DELAYED DETACHED-EDDY SIMULATION BASED PREDICTIONS OF BOUNDARY LAYER TRANSITION AND CAVITY FLOW NOISE

A THESIS SUBMITTED TO
THE GRADUATE SCHOOL OF NATURAL AND APPLIED SCIENCES
OF
MIDDLE EAST TECHNICAL UNIVERSITY

BY

ÖZGÜR YALÇIN

IN PARTIAL FULFILLMENT OF THE REQUIREMENTS
FOR
THE DEGREE OF DOCTOR OF PHILOSOPHY
IN
AEROSPACE ENGINEERING

NOVEMBER 2021

Approval of the thesis:

DELAYED DETACHED-EDDY SIMULATION BASED PREDICTIONS OF BOUNDARY LAYER TRANSITION AND CAVITY FLOW NOISE

submitted by **ÖZGÜR YALÇIN** in partial fulfillment of the requirements for the degree of **Doctor of Philosophy in Aerospace Engineering Department, Middle East Technical University** by,

Prof. Dr. Halil Kalıpçılar
Dean, Graduate School of **Natural and Applied Sciences** _____

Prof. Dr. İsmail Hakkı Tuncer
Head of Department, **Aerospace Engineering** _____

Prof. Dr. Yusuf Özyörük
Supervisor, **Aerospace Engineering, METU** _____

Examining Committee Members:

Prof. Dr. İsmail Hakkı Tuncer
Aerospace Engineering, METU _____

Prof. Dr. Yusuf Özyörük
Aerospace Engineering, METU _____

Prof. Dr. Hakan Işık Tarman
Mechanical Engineering, METU _____

Prof. Dr. Hüseyin Nafiz Alemdaroğlu
Pilotage, Atılım University _____

Assist. Prof. Dr. Onur Baş
Mechanical Engineering, TED University _____

Date: 01/11/2021

I hereby declare that all information in this document has been obtained and presented in accordance with academic rules and ethical conduct. I also declare that, as required by these rules and conduct, I have fully cited and referenced all material and results that are not original to this work.

Name, Surname: Özgür Yalçın

Signature :

ABSTRACT

DELAYED DETACHED-EDDY SIMULATION BASED PREDICTIONS OF BOUNDARY LAYER TRANSITION AND CAVITY FLOW NOISE

Yalçın, Özgür
Ph.D., Department of Aerospace Engineering
Supervisor: Prof. Dr. Yusuf Özyörük

November 2021, 157 pages

This dissertation investigates the boundary layer transition as well as the cavity flow noise prediction capabilities of a high-order in-house solver using various Delayed Detached-Eddy Simulation (DDES) frameworks. Before conducting the simulations, multiblock topology with a high-order overset grid technique is implemented into the solver, which makes mesh generation for complex geometries, such as the tunnel grids around blade sections, and cavity grids composed of two separate domains of the studied cases in this thesis. For the flow transition capability, the Baş-Çakmakçıoğlu (BCM) transition model is incorporated into DDES with a shear-layer-adapted (SLA) subgrid length scale, and applied to flowfields around a blade section and a cylinder. The results show that the BCM model captures the transition onset maintaining the laminar upstream flow while the SLA approach increases the turbulent content rapidly beyond transition. The collaboration between these two approaches enables capturing the aerodynamic coefficients of blade sections near the stall angles accurately. On the other hand, the SLA length scale is incorporated into the Improved DDES framework (IDDES-SLA) for computations of the M219 cavity flow, and its associated noise. The cavity problems are considered to have no physical lateral walls for reducing the

demand for computational resources. The results show that for these specific cases the mean and turbulent flow fields could be captured reasonably without the lateral walls, when the cavity width is taken as at least one depth. In addition, unlike the standard one, the use of the SLA length scale helps capturing the Kelvin-Helmholtz instability dominated region. IDDES-SLA yields the best acoustic results among some other tested approaches, showing good agreement with reference studies. The absence of viscous lateral walls does not seem to have an impact on overall sound levels except near the front wall.

Keywords: detached-eddy simulation, aeroacoustics, cavity flow, boundary layer transition

ÖZ

SINIR TABAKASI GEÇİŞİ VE BOŞLUK AKIŞI GÜRÜLTÜSÜNÜN GECİKTİRİLMİŞ AYRIK-ÇEVRİNTİ BENZETİMİNE DAYALI HESAPLAMALARI

Yalçın, Özgür
Doktora, Havacılık ve Uzay Mühendisliği Bölümü
Tez Yöneticisi: Prof. Dr. Yusuf Özyörük

Kasım 2021 , 157 sayfa

Bu tez, çeşitli Geciktirilmiş Ayrık-Çevrinti Simülasyonu (DDES) yöntemlerini kullanan yüksek dereceli bir çözücünün, boşluk akış gürültüsü ve sınır tabakası geçiş olayı tahmin yeteneklerini incelemektedir. Simülasyonları gerçekleştirmeden önce, çoklu-blok ağ yapısı ile birlikte yüksek mertebeli üst-üste grid özellikleri koda eklenmiştir. Böylece, kanat kesiti etrafındaki tünel ağ yapılarını ve iki ayrı bölgeden oluşan boşluk ağ yapılarını oluşturmak kolaylaşmıştır. Geçiş olayı çözümleri için, Baş-Çakmakçıoğlu (BCM) geçiş modeli, kayma-tabakasına-adapte (SLA) grid altı uzunluk ölçeğini kullanan DDES'e dahil edilmiş ve kanat kesitleri ve silindirlerin etrafındaki akış alanlarına uygulanmıştır. Sonuçlar, SLA yaklaşımının türbülanslı yapıları, geçiş olayı sonrası bölgede hızla arttırdığını ve aynı zamanda BCM modelinin gelen laminer akışı koruyarak geçiş başlangıcını doğru tahmin ettiğini göstermektedir. Bu iki yaklaşım arasındaki işbirliği, perdövites açılarındaki kanat kesitlerinin aerodinamik katsayılarının doğru bir şekilde yakalanmasını sağlamıştır. Öte yandan, SLA uzunluk ölçeği, M219 boşluk akışının ve bununla ilişkili gürültünün hesaplanması

için Geliştirilmiş DDES yöntemine (IDDES-SLA) dahil edilmiştir. Boşluk problemlerinin, hesaplama kaynaklarına olan talebi azaltmak için fiziksel yan duvarlarının olmadığı kabul edilmiştir. Sonuçlar, genişliği en az bir derinlik olarak alındığında, boşluğun ortalama ve türbülanslı akış alanlarının yan duvarlar olmadan makul bir şekilde elde edilebileceğini göstermektedir. Ayrıca, standart olandan farklı olarak, SLA uzunluk ölçeğinin kullanımı Kelvin-Helmholtz kararsızlığının hakim olduğu bölgenin tahmin edilmesine yardımcı olmuştur. IDDES-SLA, test edilen yaklaşımlar arasında en iyi akustik sonuçları vermekte ve referans çalışmalarla iyi bir uyum göstermektedir. Viskoz yan duvarların yokluğu, ön duvarın yakınları dışında genel ses seviyeleri üzerinde bir etkiye sahip görünmemektedir.

Anahtar Kelimeler: ayrık-çevrinti benzetimi, aeroakustik, boşluk akışı, sınır tabakası geçişi



Devin’e

ACKNOWLEDGMENTS

I am grateful to the following national HPC centers to provide me computational resources in order to conduct all the simulations presented in this thesis:

- Some part of the parallel computations have been made using the METUWIND (Center For Wind Energy Research) High Performance Computing Laboratory.
- The numerical calculations reported in this paper were partially performed at TUBITAK ULAKBIM, High Performance and Grid Computing Center (TRUBA resources).
- Computing resources used in this work were partially provided by the National Center for High Performance Computing of Turkey (UHeM) under grant number 4008812020.

Bu tez çalışması sırasında aldığım yardımların kuşkusuz en büyük pay sahibi, yüksek lisans eğitimimden itibaren danışmanlığımı yapmakta olan Prof. Dr. Yusuf Özyörük'tür. İhtiyacım olduğu her anda bana zaman ayırdığı, sorunlarımı sabırla dinlediği, hem teknik anlamda hem de manevi anlamda bana destek verdiği için kendisine çok teşekkür ederim. Özellikle boşluk akışı benzetimleri sırasında yaşadığım uzun süreli bir çıkmaz dönemini kendisinin tecrübeleri sayesinde aşabildim. Bunun yanı sıra, Yusuf Hoca bugüne kadar yaptığım tüm çalışmalarımda beni hep teşvik etmiş, yayınlarımın her bir satırını özenle okuyup geri bildirim sağlamıştır. Kendisinin bende emeği çok. Sağolun Hocam!

Tez İzleme Komitesi (TİK) üyeleri Prof. Dr. İsmail H. Tuncer ve Prof. Dr. Hakan Tarman hocalarıma doktora çalışmam boyunca katıldıkları tüm TİK toplantılarında verdikleri destek ve görüşleri için çok teşekkür ederim. Bu tezin karmaşık ve takip etmesi yorucu içeriğini derleyip toparlamamda ve en son halini almasında kendilerinin doğrudan katkıları olmuştur.

Tez jüri üyelerinden Prof. Dr. Nafiz Alemdaroğlu ve Dr. Öğr. Üyesi Onur Baş hocalarımın tez çalışmama gösterdikleri ilgi ve tez sunumu sırasında yaptıkları katkılardan dolayı teşekkür ederim. Nafiz Hoca'nın özellikle tezin organizasyonuyla ilgili yaptığı geri bildirimlerin, tezin daha anlaşılır olmasında önemli etkisi olmuştur. Onur Hoca'ya, tez çalışmalarımın başlarında geçiş akışı modeli ile ilgili olarak verdiği tavsiyelerden dolayı ayrıca teşekkür etmek istiyorum.

Çalışmalarımı en başından beri büyük bir ilgiyle takip eden, çok uzaklarda olsa bile hiçbir zaman desteğini esirgemeyen eski çalışma arkadaşım Dr. Kenan Cengiz'e çok teşekkür ederim. Tezimin önemli bir kısmı, ortak yürüttüğümüz çalışmalardan oluşmaktadır. Resmiyette gözükmese de kendisi gizli yardımcı danışmanımdır. Umarım ileride de bu birlikteliğimiz devam eder.

Birlikte çalışmaktan büyük kıvanç duyduğum ve yardımlarını hiç esirgemeyen arkadaşlarım Arda, Hazal, Mete, Berk, Hüseyin, Zeynep, Özcan, Özgür ve daha nicelerine teşekkür etmek isterim. Özellikle, doktora süresince aynı odayı paylaştığım, çalışmalarımı rahatlıkla yapabilmemi sağlayan ve her türlü sorunumu sabırla dinleyen Arda'nın yeri bende ayrıdır.

Son olarak, akademik çalışmalarım boyunca sürekli desteğini yanımda hissettiğim, başta annem Elmas ve eşim Hazal olmak üzere değerli aileme çok teşekkür ederim. Özellikle Hazal, tökezlediğim her anda yanımdaydı ve tekrar tekrar çalışmalarıma odaklanmamı sağladı. Umarım ben de onun doktora süresince aynı desteği sağlayabilirim. Pandemi günlerinde bana rahat bir çalışma ortamı sağlayan Altuğ ailesine (Sacit, Mine, Muratcan ve Biber) ayrıca minnettarım.

Tezimi, çalışmalarımın son yıllarında aramıza katılan ve bana büyük bir neşe ve mutluluk kaynağı olan biricik oğlum Devin'e adıyorum!

TABLE OF CONTENTS

ABSTRACT v

ÖZ vii

ACKNOWLEDGMENTS x

TABLE OF CONTENTS xii

LIST OF TABLES xvii

LIST OF FIGURES xviii

LIST OF ABBREVIATIONS xxiv

CHAPTERS

1 INTRODUCTION 1

1.1 Backgrounds 1

1.1.1 Detached-Eddy Simulation 1

1.1.2 Boundary Layer Transition 6

1.1.3 Cavity Flow 10

1.2 Motivation of the Thesis 17

1.3 Proposed Methods and Models 18

1.3.1 Cavity Flow Part 18

1.3.2 Transitional Flow Part 20

1.4 The Outline of the Thesis 21

2 METHODOLOGY 23
2.1 METUDES - Flow Solver 23
2.1.1 Favre-Averaged Navier-Stokes Equations 23
2.1.2 Spalart-Allmaras One-Equation Model 25
2.1.3 Turbulence Modeling and Resolving 27
2.1.3.1 Unsteady Reynolds-Averaged Navier-Stokes 27
2.1.3.2 Detached-Eddy Simulation 27
2.1.3.3 Delayed Detached-Eddy Simulation 28
2.1.3.4 Shear-Layer-Adapted Subgrid Length Scale 29
2.1.4 Numerics 31
2.1.5 Code Structure 33
2.2 Improvements to METUDES 33
2.2.1 DDES Frameworks 33
2.2.1.1 Transitional DDES 33
Baş-Çakmakçıoğlu Transition Model 34
Incorporation of the BCM Model into DDES 35
2.2.1.2 Improved Delayed Detached-Eddy Simulation 38
Incorporation of the Δ_{SLA} into IDDES 40
2.2.2 Numerics 40
2.2.2.1 Multiblock Topology 40
2.2.2.2 High-Order Overset Grid Technique 41
2-D $\mathbf{2^{nd}}$-Order Interpolation 44
2-D $\mathbf{3^{rd}}$-Order Interpolation 46

3-D $\mathbf{3}^{\mathbf{rd}}$-Order Interpolation 47

2.2.2.3 Optimizing the Numerical Algorithms 48

Change in the Residual Smoothing Algorithm 50

Shock Sensor in the N-S Equations using TVD Approach 51

Biased Artificial Dissipation near the Solid Walls 52

Directional Scaling Factor in the Artificial Dissipation of the Turbulence Model 53

3 SIMULATION SETUPS 57

3.1 Grid Generation 57

3.2 Boundary Conditions 59

3.3 Initial Conditions 60

3.4 Time Step Selection 62

4 VALIDATION STUDIES 63

4.1 Flatplate Test Case 63

4.2 Eppler E387 Airfoil Test Case 66

4.3 Isentropic Vortex Convection 70

4.4 Backward-Facing Step Flow 72

5 TRANSITIONAL AND CAVITY FLOW SIMULATIONS 79

5.1 Flow over an NRELS826 Blade Section 79

5.1.1 Configurations and Setups 80

5.1.1.1 Geometry 80

5.1.1.2 Grid Generation 81

5.1.1.3 Boundary Conditions 82

5.1.2 Results and Discussion 83
5.1.2.1 Grid Dependency Analysis 84
5.1.2.2 Case 1: Reynolds number of 100,000 85
5.1.2.3 Case 2: Reynolds number of 145,000 90
5.2 Flow over a Circular Cylinder 95
5.2.1 Grid Generation and Boundary Conditions 95
5.2.2 Results and Discussion 97
5.2.2.1 Grid Dependency Analysis 97
5.2.2.2 Simulations 97
5.3 Transonic Flow over an Open Cavity 104
5.3.1 Configurations and Setups 104
5.3.1.1 Geometry and Boundary Conditions 104
5.3.1.2 Grid Generation 106
5.3.2 Results and Discussion 108
5.3.2.1 Mean Flow Fields 109
5.3.2.2 Instantaneous Flow Fields 117
5.4 Supersonic Flow over an Open Cavity 125
5.4.1 Configurations and Setups 125
5.4.2 Results and Discussion 126
6 CONCLUSIONS 131
6.1 Improvements to METUDES 131
6.2 Boundary Layer Transition 132
6.2.1 Flow over an NRELS826 Blade Section 133

6.2.2 Flow over a Circular Cylinder 134

6.3 Cavity Flow 134

6.3.1 Transonic Flow over an Open Cavity 135

6.3.2 Supersonic Flow over an Open Cavity 136

6.4 Suggestions and Future Work 136

REFERENCES 139

APPENDICES

A THE ROSSITER FORMULA 153

CURRICULUM VITAE 155

LIST OF TABLES

TABLES

Table 3.1 Boundary conditions applied on each computational domain faces for all problems 61

Table 5.1 Blade and flow parameters of the benchmark studies where U_∞ is the freestream velocity, Tu_∞ is the freestream turbulence intensity, and s/c is the span-to-chord ratio 80

Table 5.2 Simulation parameters of the current and benchmark studies 82

Table 5.3 Comparison of lift and drag coefficients of the blade section 91

Table 5.4 Grid dependency study for cylinder flow 98

Table 5.5 The details of the cavity grids 107

Table 5.6 The details of the transonic open cavity flow simulations 109

Table 5.7 Comparison of frequencies and PSD levels of Rossiter modes 121

Table 5.8 The details of the cavity grids 126

LIST OF FIGURES

FIGURES

Figure 1.1 Schematic of the natural transition process showing top and side views of a boundary layer along a flatplate [124] 7

Figure 1.2 Examples of cavities in aerodynamic structures 11

Figure 1.3 Flow over a typical cavity geometry 12

Figure 1.4 Schematic of the cavity flow (solid line: open cavity, dashed line: closed cavity) [66] 13

Figure 1.5 Acoustic feedback mechanism occurring in the open cavity flow [65] 14

Figure 1.6 Broadband noise spectrum with Rossiter modes inside an open cavity [65] 14

Figure 2.1 Multiblock communication between two blocks through ghost and inner cells 41

Figure 2.2 The multiblock structured mesh domain around an open cavity geometry with $L/D = 5$. Block 1 represents the inside of the cavity while Block 2 represents the outside of it. 42

Figure 2.3 Overset interpolation between two blocks through fringe and donor cells 43

Figure 2.4 Cavity flow field deformations happening during initial cavity flow simulations. Above: eddy viscosity related contours, below: pressure contours 49

Figure 2.5 Cells used for the 4th-order artificial dissipation in j^{th}-direction at the wall cell (j=1) 53

Figure 2.6 Flow field by DDES after numerical improvements. Above: eddy viscosity related contours, below: pressure contours 55

Figure 2.7 Comparison of the convergence speeds of the residual drop in x-momentum 55

Figure 3.1 Close views of grids showing the grid nodes clustered around a) the upstream corner of a cavity, b) the leading edge of the NRELS826 airfoil profile 59

Figure 3.2 Boundary faces of a single computational block 60

Figure 4.1 2-D view of the computational domain of the flatplate test case . 64

Figure 4.2 Comparison of γ_{BCM} distributions around the flatplate obtained by METUDES and SU2 codes 64

Figure 4.3 Distributions of Term_1 (above) and Term_2 (below) around the flatplate 65

Figure 4.4 The eddy viscosity contours around the flatplate 65

Figure 4.5 The friction coefficient distributions along the flatplate viscous wall 66

Figure 4.6 2-D close view of Grid 2 for the E387 airfoil test case. Only odd-numbered points are shown. 67

Figure 4.7 The pressure coefficient distributions along the E387 airfoil surface 68

Figure 4.8 Instantaneous distributions of the triggering terms (red color: 30.0) and the intermittency function (red color: 1.0) around the E387 airfoil 69

Figure 4.9 The eddy viscosity contours and the streamlines indicating the laminar separation bubble around the E387 airfoil 69

Figure 4.10 Pressure contours of the isentropic vortex convected along single (a-c) and multiblock (d-l) domains at sequential times. Communication between two blocks is conducted by one-to-one (d-f), the 2nd-order overset interpolation (g-i), and the 3rd-order overset interpolation (j-l). . 71

Figure 4.11 Normalized pressure distribution of the isentropic vortex along $y = 0.5$ m at sequential times. The plots are obtained from Figure 4.10. 72

Figure 4.12 2-D views of the computational grid of the backward-facing step flow problem. One quarter of nodes are shown. Red lines indicate the block edges. 73

Figure 4.13 Comparison of the friction coefficient distributions along the reattachment wall 75

Figure 4.14 Isosurfaces of Q-criterion ($Q = 0$) of an instantaneous flow field around the backward-facing step geometry from different views 76

Figure 4.15 Some variables from an instantaneous flow field around the backward-facing step geometry 77

Figure 5.1 2-D views of the tunnel grid with multiblock topology around the blade section having AoA of 8° 82

Figure 5.2 3-D view of the computational domain with boundary conditions 83

Figure 5.3 Lift and drag coefficients together with the running averages of the blade profile changing with dimensionless time at AoA of 10° and Re_1 via DDES-SLA-BCM3 83

Figure 5.4 C_p distributions over the blade surface at AoA of 12° and Re_1 via DDES-SLA 84

Figure 5.5 C_l and C_d values of the wind turbine blade profile for several AoAs around stall ($\mathrm{Re} = 100,000$) 85

Figure 5.6 C_p distributions over the blade surface for various AoAs (Re $=$ $100,000$) 86

Figure 5.7 C_f distributions over the blade surface for various AoAs (Re $=$ $100,000$) 87

Figure 5.8 Laminar separation bubble observed around the leading edge at AoA of 12° via DDES-SLA and DDES-SLA-BCM3 (Re $= 100,000$) . 88

Figure 5.9 The intermittency function contours (red: $\gamma_{BCM3} = 1.0$) around the blade via DDES-SLA-BCM3 (Re $= 100,000$) 88

Figure 5.10 Isosurfaces of Q-criterion ($Q = 0$) colored by $\hat{\nu}_t/\nu$ around the blade at AoA of 12° via DDES and DDES-SLA (Re $= 100,000$) 89

Figure 5.11 Transition model terms (red color: 30.0) and the intermittency function (red color: 1.0) around the blade surface at AoA of 10° (Re $=$ $100,000$) 89

Figure 5.12 C_p distributions over the surface (left) and the streamlines around the blade (right) at AoA of 8° (Re $= 145,000$) 92

Figure 5.13 C_p distributions over the surface (left) and the streamlines around the blade (right) at AoA of 12° (Re $= 145,000$) 93

Figure 5.14 Isosurfaces of Q-criterion ($Q = 0$) colored by $\hat{\nu}_t/\nu$ around the blade at AoAs of 8° and 12° via DDES and DDES-SLA (Re $= 145,000$) 94

Figure 5.15 $\hat{\nu}_t/\nu$ contours of mean flow fields at AoA of 12° (Re $= 145,000$) 94

Figure 5.16 Close and far views of two grids having different wake resolutions over a cylinder 96

Figure 5.17 Comparison of drag coefficients of the cylinder flow for different Reynolds numbers. For clear visualization, the results are divided into two groups. 99

Figure 5.18 The onset angles of the flow separation forming wake as well as certain eddy viscosity values (dashed dot: $\hat{\nu}_t/\nu = 0.001$, solid: $\hat{\nu}_t/\nu = 5.0$) for different Reynolds numbers 99

Figure 5.19 Averaged streamlines over the cylinder obtained by different methods (Re $= 5.0 \times 10^5$) 101

Figure 5.20 Averaged streamlines over the cylinder obtained by DDES-SLA for different Reynolds numbers 102

Figure 5.21 Mean eddy viscosity ($\hat{\nu}_t/\nu$) contours obtained by different methods (Re $= 10^5$) 103

Figure 5.22 Instantaneous isosurfaces of Q-criterion colored by eddy viscosity levels ($\hat{\nu}_t/\nu$) obtained by different methods ($Q = 10^3$, Re $= 10^5$) . . 103

Figure 5.23 Instantaneous vorticity contours at wake region obtained by different methods (Re $= 10^6$) 103

Figure 5.24 Schematic of Configuration 2 with boundary conditions 105

Figure 5.25 Comparison of outer span widths between two configurations. Red lines belong to Configuration 1. 106

Figure 5.26 Close views of Grid D showing one every four cells 108

Figure 5.27 3-D close view of Grid E showing one every four cells at IJK plane surfaces 108

Figure 5.28 Comparisons of mean flow velocity and TKE profiles along the cavity at middle of the span 110

Figure 5.29 Comparisons of mean flow velocity and TKE profiles along the cavity at middle of the span 111

Figure 5.30 Comparisons of mean flow velocity and TKE profiles along the cavity at middle of the span 112

Figure 5.31 Streamlines of the mean flow fields at middle of the span 113

Figure 5.32 Variations of the momentum thickness, the vorticity thickness, and the ratio of them along the shear layer 115

Figure 5.33 Spanwise two-point auto-correlation of mean streamwise velocity profiles at different locations along the shear layer 117

Figure 5.34 Isosurfaces of Q-criterion ($Q = 0$) colored by $\hat{\nu}_t/\nu$ values 118

Figure 5.35 Pressure fluctuations by IDDES-SLA at equally spaced instants over a convection period of shear layer 119

Figure 5.36 Comparison of overall sound pressure levels emitted from the cavity ceiling at midspan 120

Figure 5.37 Comparison of PSD spectra at three cavity ceiling locations at midspan 122

Figure 5.38 Sound level spectral surfaces along the span at three cavity ceiling locations 124

Figure 5.39 PSD spectra at $x/D = 0.25$, and $z/D = 0$ on the cavity ceiling with a spanwise acoustic mode representation 125

Figure 5.40 Comparison of boundary layer velocity profiles at $x/L = -0.83$ 127

Figure 5.41 Comparisons of mean flow velocity and TKE profiles along the cavity at middle of the span 127

Figure 5.42 Streamlines of the mean flow fields at middle of the span obtained by IDDES-SLA 128

Figure 5.43 Variations of the momentum thickness, the vorticity thickness, and the ratio of them along the shear layer 129

Figure 5.44 Isosurfaces of Q-criterion ($Q = 0$) colored by $\hat{\nu}_t/\nu$ values of instantaneous flow fields 130

LIST OF ABBREVIATIONS

2-D	Two-Dimensional
3-D	Three-Dimensional
AoA	Angle of Attack
AR	aspect ratio
BC	boundary condition
BCM	the modified version of Baş-Çakmakçıoğlu
BCM3	BCM with the proposed modifications
Cd	drag coefficient
Cf	friction coefficient
CFD	Computational Fluid Dynamics
Cl	lift coefficient
Cp	pressure coefficient
DDES	Delayed Detached-Eddy Simulation
DES	Detached-Eddy Simulation
DNS	Direct Numerical Simulation
DRP	dispersion-relation-preserving
FANS	Favre-averaged Navier-Stokes
GIS	Grid-Induced Separation
IDDES	Improved Delayed Detached-Eddy Simulation
ILES	Improved Large Eddy Simulation
K-H	Kelvin-Helmholtz
LDV	Laser Doppler Velocimetry
LES	Large Eddy Simulation

LLM	Log Layer Mismatch
MSD	Modeled-Stress Depletion
N-S	Navier-Stokes
OASPL	Overall Sound Pressure Level
PIV	Particle Image Velocimetry
PSD	Power Spectral Density
RANS	Reynolds-averaged Navier-Stokes
Re	Reynolds number
S-A	Spalart-Allmaras
SLA	shear-layer-adapted
SR	stretching ratio
SST	shear stress transport
T-S	Tollmien-Schlichting
TKE	turbulent kinetic energy
TVD	Total Variation Diminishing
URANS	Unsteady Reynolds-averaged Navier-Stokes
VTM	Vortex Tilting Measure
WMLES	Wall-Modeled Large Eddy Simulation
ZDES	Zonal Detached-Eddy Simulation

CHAPTER 1

INTRODUCTION

1.1 Backgrounds

1.1.1 Detached-Eddy Simulation

Turbulence is one of the most complex phenomena in mathematics and the physical world. Among the many definitions in literature, Çıray describes it as "Turbulence consists of essentially unsteady and three-dimensional (3-D) flow motions where any quantities are random in time and space while mean quantities are deterministic" [18]. Such disordered flow fields result in eddies, a group of highly correlated fluid particles, and also known as coherent structures. They are inherently vortical, diffusive, and dissipative. There is an energy cascading between eddies: At first, large eddies, which are very energetic and unstable, are created under large gradients (due to either a geometry and/or a freestream itself) in the flow field. Then, they break up and turn into smaller eddies as they loose their energies because of viscosity. This decaying energy transfer keeps going until the smallest eddy which then disappears or takes a part in another flow. As a whole, this phenomena is observed in the energy spectrum corresponding to different wavenumbers.

Turbulent flow simulations vary based on their setting the resolution level of eddies within this energy spectrum. The best way to simulate the flow field is to resolve all involved eddy structures. This is called Direct Numerical Simulation (DNS). In the DNS approach the Navier-Stokes (N-S) equations, a mathematical model of the fluid flow dynamics, are numerically solved resolving all eddies. However, as Reynolds number (Re), representing relative magnitude of inertial to viscous forces, increases

the length scale of the smallest eddy structure (Kolmogorov scale) decreases accordingly. In a 3-D computational domain, roughly Re^3 grid cells are required, which makes DNS costly to perform for the real-world applications. This is why DNS studies in literature solve mostly simple two-dimensional (2-D) flow problems. Large Eddy Simulation (LES), on the other hand, only resolves large eddies filtered out from the N-S equations. Small eddies, which are on the subgrid scales by the filtering process, are modeled, instead. Here, the large eddies represent the non-isotropic and the geometry dependent components of the flow dynamics while the small eddies are isotropic and under universal equilibrium. Resolving only the large eddies still provides the desired momentum transfer and turbulent mixing in the field without adequate dissipation mechanism. The modeling of subgrid scales makes up for this mechanism and reduces the computational cost in comparison to DNS, making LES a plausible approach, particularly in free shear flows. Nevertheless, in the case of a wall-bounded flow problem with high Re, a very fine grid resolution requires inside the boundary layer since the energetic eddies emanate mostly from the wall itself. The total grid cell numbers could increase with $Re^{2.4}$. Time step requirement reduces in the same manner. The recent LES strategies prefer to model near wall region by using wall-functions, solving different equations, or averaging the variables [87]. Besides these, the Reynolds-averaged N-S (RANS) approach models all scales of eddies in the entire flow domain by relating the Reynolds stresses with mean velocity field and the "eddy viscosity". This is a commonly used method for the Computational Fluid Dynamics (CFD) applications because it cuts the computational cost down to feasible levels for all types of flow problems including the industrial ones. However, the averaging procedure brings out new unknowns namely the Reynolds stresses, causing a closure problem. Thus, an additional model equation(s) must be solved. These model equations are mostly good at estimating attached boundary layers. However, they miss the instantaneous information necessary for acoustical and vibrational problems. Although Unsteady RANS (URANS) may reveal an unsteady solution, it fails at largely separated zones as well as free shear flows. The reason is that modeling all eddies causes redundant Reynolds stresses which damp the instabilities, and thereby delaying the formation of 3-D structures in flow fields.

Detached-Eddy Simulation (DES) [108] was initially proposed to simulate massively

separated flow fields observed around aircraft and automobiles while overcoming the drawbacks of both URANS and LES. It is a kind of hybrid RANS/LES method, aiming to model the attached boundary layers and then to resolve the highly separated field. DES is based on the RANS equations. It models eddy viscosity in the boundary layer as RANS does, and switches to an LES-like mode at the outer boundary layer regions. The switching is done through the length scale of the model equation. It is kept the same when the RANS mode is active. On the other hand, the maximum dimension of a grid cell (Δ_{max}) is used as a subgrid length scale in the LES mode. DES takes the minimum of them and solves the model equation(s) accordingly. Studies in the last two decades have shown that DES can supply high accuracy with low computational costs in wall-bounded, highly separated aerodynamic flow problems. Since large eddies dominate these separated regions, the RANS resolution suffices to obtain accurate aerodynamic results [109]. However, its success is limited to only highly detached flows due to the unnatural switching mechanism, revealing two major defects. One of them is known as the grey-area problem, the most accentuated one in literature, and the other is regarding a delay of possible instabilities inside the shear layers.

DES makes the RANS/LES switching sharply, which is not natural. There is no energy transfer mechanism between the resolved and the modeled scales. In fact, there is no such discontinuity in eddy viscosity levels. It means there is a region around the boundary layer edge where the DES mode should not be LES or RANS alone. This region is called the grey-area [108, 109], which restricts DES implementations. Several modifications to DES have been proposed to cure the grey-area problem. For example, DES may switch to the LES mode earlier due to "ambiguous grid" cases (i.e. grids designed improperly). In this type of grids there are some cells, inside the boundary layer, having smaller subgrid length than the model one. They lead to an early switch to LES in the RANS region where the resolution is not sufficient to resolve eddies. As a consequence, DES develops less eddy viscosity, known as the Modeled-Stress Depletion (MSD) problem. In addition, low viscosity might induce earlier separation than expected (the Grid-Induced Separation (GIS) problem). This pitfall was overcome by Spalart *et al.* in their approach called Delayed DES (DDES) [110]. It keeps the RANS mode inside the attached boundary layer through a bound-

ary layer shielding function used in the length scale switching. This effort works well in many aerodynamic flow problems and is the most commonly used method among all the DES types. Another approach to avoid the grey-area problem is to divide the grid domain into zones such that the user defines the RANS zone and the LES zone on the grid. This method is called Zonal DES (ZDES) [25]. Despite its accuracy [25, 26], a zonal approach is difficult to implement in complex flow problems. Besides, another group of researchers brings a different approach that adapted the Wall-Modeled LES (WMLES) treatment [88] into DES [83, 105, 26]. In theory, the modeling mode is activated in only a much thinner region of a boundary layer, and the rest of the domain is resolved. The switching basically occurs very close to the wall ($y^+ \approx 15 - 20$). DES type WMLES methods seem to solve the grey-area problem; however, it brings up another issue: the Log Layer Mismatch (LLM) problem. WMLES reveals two log layer solutions in the boundary layer; a RANS solution (from the inner layer) and an LES one (from the outer layer). The channel flow studies showed that the intercept constants of the two log layer solutions do not match, which causes an underprediction of the skin friction coefficient. A recent modification to solve the LLM issue is Improved DDES (IDDES) [105]. This method combines DDES and WMLES by an empirical blending function so that while in the cases without inflow turbulent content it treats as DDES, in others the length scale reduces to the WMLES one, resulting in much more turbulence resolution. In the WMLES mode, it uses an elevating function to prevent less modeled viscosity due to the log layer mismatching. In this respect, IDDES cures some certain weaknesses of DES regarding the uncertain switching and shows successful results in different flow problems where DDES and WMLES activations differ [105]. Nevertheless, increase in the computational cost due to partly-resolved eddies inside the boundary layer should be taken into consideration.

Apart from the enhancements to the DES switching, the selection of the subgrid length scale has been discussed in literature. Most of the DES applications take the standard subgrid length scale ($\Delta_{max} = max(\Delta_x, \Delta_y, \Delta_z)$) in the LES mode whereas some approaches prefer to use the cube root of the cell volume ($\Delta_{vol} = \sqrt[3]{\Delta_x \Delta_y \Delta_z}$) [7, 25]. Since the grid cells outside the boundary layer are intended to be nearly cubical, both definitions do not make any difference there. However, computational

domains may have anisotropic grid cells just outside the boundary layers. In addition, some DES applications (when properly adjusted) may resemble WMLES, as already mentioned, which means LES mode is activated inside the boundary layer where isotropy of the cells may not be preserved. In these anisotropic grids, the above-mentioned subgrid length scale selections (Δ_{max} and Δ_{vol}) become distinct, and this may pose a problem. Δ_{vol} approach may be too harsh for eddies of smaller dimensions to survive [109]. Moreover, it may cause numerical instabilities because of too small eddy viscosities. On the other hand, Δ_{max} is absolutely a more conservative and a safer choice. This is preferred in classical DES and DDES applications and it provides a good RANS functioning. But this time, it may suppress the flow instabilities that are expected to generate eddies. This is the second issue of DES drawbacks, as mentioned previously. In brief, both subgrid length scale selections are not ideal. There have been some progress towards resolving this issue. In IDDES, a modified subgrid length scale is used to avoid these problems in case of anisotropic grid cells. It roughly combines the wall distance and the grid cell dimensions in both DDES and WMLES modes. But, it does not get any information from the turbulent flow solution as well as not address the delay of instability problem. Another important improvement, made by Chauvet *et al.*, is taking the subgrid length scale as Δ_{ω}, which depends on the vorticity orientation of the flow [16]. This flow-dependent length scale attempt tries to defeat slow turbulent development. However, Δ_{ω} is mostly used in the zonal approaches [16, 26]. A more recent modification, a shear-layer-adapted length scale (Δ_{SLA}), was introduced by Shur *et al.* [106]. This new definition makes use of a vorticity-aligned grid dimension definition and a curbing mechanism for eddy viscosity in 2-D shear layers so that it accelerates the transition to the LES mode in shear layers. The resulting length scale serves as a reduction to the vorticity-oriented length scale up to one order in regions where the K-H instability waves are expected to occur, thus leaving ground to transition to resolved (LES) contents. Additionally, for wall-bounded flows, this reduction is inactivated to keep the boundary layer shielded as done in the standard DDES with Δ_{max}. This version has proven to be successful not only in free shear layers, but also in wall-bounded flows, jet flow, decaying turbulence, and backward-facing step flow [106].

1.1.2 Boundary Layer Transition

Boundary layer transition phenomena refers to a process of transition from laminar flow to fully turbulent flow. The transition process is complicated because many possible disturbances in flow setting may trigger the transition; in fact, flow instabilities occurred later on may also differ. Freestream turbulence levels, surface roughness, pressure gradients, compressibility (Mach number) effects, heat transfer, and suction/blowing air are some of the common examples to these disturbances. Boundary layer transition problems are categorized regarding their instability mechanisms. One of them is called natural transition (see Figure 1.1). Here, the completely attached boundary layer is triggered under very low turbulence intensity and the process takes place slowly. First, the disturbances start to grow inside the boundary layer as a receptivity stage. Then, the Tollmien-Schlichting (T-S) waves emanate. These 2-D waves are known as the primary instability. From the receptivity stage to the end of the primary instability, the disturbances interact to each other linearly; thus, the corresponding region is called the linear region. After the disturbances reach a certain amplitude (if they are not damped out), the secondary instability is observed. The waves are not 2-D anymore as spanwise vortices form in addition to the streamwise ones. This yields nonlinear interactions between the waves, and therefore, a nonlinear region starts. Nonlinearities and high disturbance growth rates make the process go into the final stage, called breakdown stage, where the instability waves break into the smaller ones. As a result, the flow becomes fully turbulent. In the case of higher disturbances, commonly seen in the real-world applications, the primary instability stage of the natural transition is bypassed. These situations are called bypass transition. In addition, there is a separation-induced transition, where laminar flow is separated first under an adverse pressure gradient or any geometrical induction, then the transition process occurs in the separated shear layer, and finally the flow becomes fully turbulent, which may reattach to the surface. Since transition is initiated in free shear layers, 2-D Kelvin-Helmholtz (K-H) waves are seen as a primary instability. This mechanism is inviscid as it happens above the surface. Although the T-S waves still exist, the K-H instability, which has a higher amplification rate, is the dominant one. These 2-D waves quickly roll along the spanwise direction so that a three-dimensionality takes place as a secondary instability. After that, they

breakdown to the smaller scales and the separated flow reattaches as turbulent flow, resulting in a separation bubble. For high turbulence intensities ($> 1.5\%$) the separation bubble length is reduced and the receptivity stage is bypassed. This means that a bypass situation can be also seen in the separation-induced transition; however, in this case the primary (K-H) instability is not bypassed [128]. As the turbulence intensity continues to increase ($> 5.5\%$) flow goes into turbulent regime without separation so that the K-H instability does not appear [1].

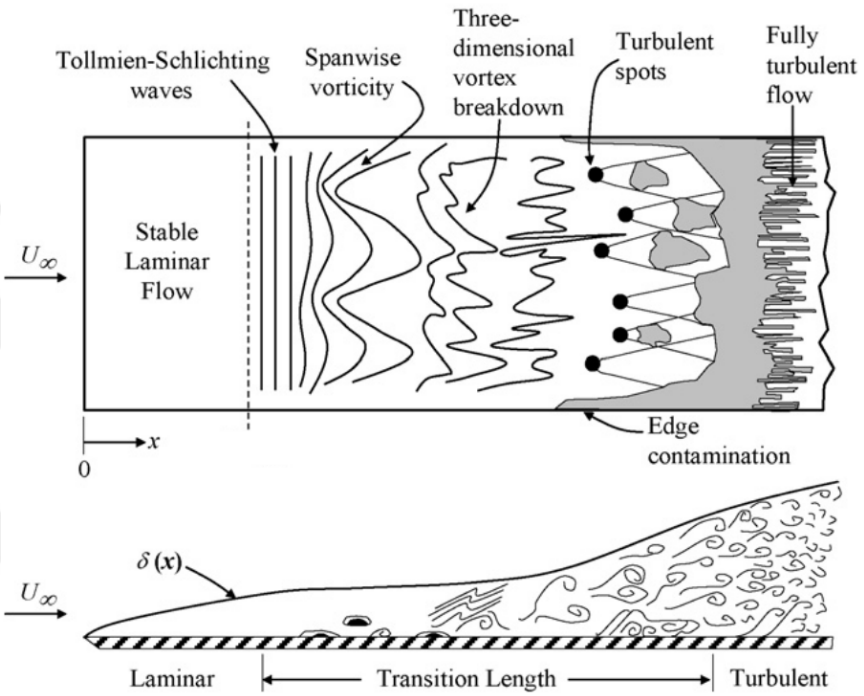


Figure 1.1: Schematic of the natural transition process showing top and side views of a boundary layer along a flatplate [124]

Laminar-to-turbulent transition influences the boundary layer quantities, which directly results in an alteration of aerodynamic performances (especially the maximum lift coefficient prediction). Flow problems with low Re that are observed particularly in low-speed wings, rotor blades, high-lift devices, and wind turbine blades are exposed to transition effects excessively that is why both industry and academic communities have been working on this topic over many years. Earlier studies were mostly based on a linearized theory and measurements which investigated the linear

[1] It should be noted that in the case of a geometrically induced separation, the K-H instability is bypassed under a high turbulence intensity as in the attached boundary layer transition.

region of the transition. After the nonlinear mechanism with 3-D breakdown was first discovered by Klebanoff et al. [52], the natural transition process could be understood as a whole. For a long time, the linear stability theory [71] had been extended and widely used for transition estimations. However, this theory had ability to handle only the natural transition. This is why the bypass mechanism had been discovered much later (through measurements of Morkovin [78]). For the reason that the limitations of measurement techniques made the investigation of the near-surface flow field difficult, detailed analysis of transition (including bypass and separation-induced cases) was conducted by DNS [53, 68, 47, 94] and LES studies [89, 129, 64]. For practical applications, on the other hand, transition models incorporated into RANS simulations have been proposed because CFD based RANS approaches mostly assume the whole flow field as fully turbulent. The e^N method, which relates the amplification rate to the transition onset based on the stability theory, is one of them [11, 114]. The input variables required for the method are provided by a different boundary layer solver that is coupled with a RANS code. Then, the output is used for the RANS model. This incorporation procedure is complicated, and the e^N method is limited to certain type of problems [28]. Use of low Re transition models [125, 60] is another approach. It basically damps the turbulence in viscous sublayer through a damping function; however, the transition capability is controversial as the physical backgrounds of viscous sublayer and the transition mechanism are completely different. Reformulating the function as the flow conditions change is not simple either.

The most common transition modeling approaches are based upon experimental correlations. Here, the freestream turbulence intensity and the momentum thickness Reynolds number required for transition ($Re_{\theta t}$) are related (as in [1]). The main idea is that when the calculated momentum thickness Reynolds number (Re_θ) is exceeded $Re_{\theta t}$, turbulence (either any term of the turbulence model equation or the eddy viscosity itself) is included in the flow equations; otherwise, it is suppressed. Suzen and Huang [115] developed an intermittency transport equation in order to activate turbulence through an intermittency function (γ) that is zero in the laminar flow and one when the transition criteria ($Re_\theta > Re_{\theta t}$) is satisfied. Despite its accuracy, the computation of Re_θ is hard to implement in modern CFD codes (especially the parallel ones). The reason is that this is an integration operation, which requires not only

a search algorithm to find the boundary layer edge but also a nonlocal cell information at each step. An efficient nonlocal correlation-based transition model has been improved by Kozulovic et al. for unstructured parallel codes and they showed that only 7% computation load is added in steady state simulations [56]. On the other hand, Menter et al. came with a novel idea that checks the transition criteria at each cell by using the vorticity Reynolds number (Re_ν) which is proportional to Re_θ and obtained using only the local values [76]. Hereby, an implementation of the model into any solver becomes easier. This widely used model is called $\gamma - Re_\theta$ because it solves an additional transport equation for Re_θ. By doing this, nonlocal information coming from the turbulent intensity is eliminated. Then, one-equation local transition model to be solved for only γ function has been proposed and it was shown that use of nonlocal Re_θ values can provide results in similar accuracy to the previous one [77]. These correlation-based models were mainly developed for $k - \omega$ turbulence equations where the production and destruction terms of the transport equation for turbulent kinetic energy are multiplied with the intermittency function. Medida and Baeder [75] modified the two-equation transition model to be coupled with the Spalart-Allmaras (S-A) turbulence equation in which an eddy viscosity related term is solved ($\tilde{\nu}$). They also demonstrated that starting the simulation with $\tilde{\nu}/\nu_\infty \leqslant 10^{-8}$ makes the upstream flow totally laminar before the transition onset which is essential for transitional problems. Lately, Baş and Çakmakçıoğlu have introduced a zero-equation correlation-based model that obtains the intermittency function algebraically (without any transport equation) [9]. This model (called B-C) has been introduced for the S-A one-equation model. The B-C model directly multiplies the production term of the S-A equation with γ that is computed via two terms: one is used to trigger transition as critical Re_θ is exceeded (through Re_ν as in the $\gamma - Re_\theta$ model) whereas the other term allows γ, generated by the first term, into the boundary layer. The idea is to benefit from the convection and diffusion features of the already solved turbulence model instead of solving extra equations. This makes the model very cheap. They showed that in steady-state simulations the B-C model can reveal quite comparable results to those obtained by other transition models with transport equations.

In the last decade, researchers have taken interest in transitional DES approaches. Initial attempts have blended classical DES based on the $k-\omega$ turbulence equation with

the $\gamma - Re_\theta$ transition model [107]. Over the last few years, enhanced DES versions (such as DDES, IDDES, and DDES with WALE subgrid scale) using the S-A or $k-\omega$ turbulence closure have been coupled with different correlation-based models (B-C model, γ model, or a two transport equation model based on an envelope amplification factor) [19, 122, 24]. Most of them implemented the intermittency function in the production and destruction terms of the turbulence equation as usual. On the other hand, Coder et al. [19] used the function in the trip term of the S-A equation (f_{t2}) in order not to corrupt the numerical stability of the fully turbulent version as well as in the length scale definition of DDES to ensure the RANS mode in the attached laminar boundary layers.

It should be emphasized that the correlation-based models do not intend to represent the process of transition mechanisms. The physics behind the process are ensured by the empirical correlations. Hence, as long as the correct correlations are provided, the models can be used for all transition types. The use of intermittency function taking a value between 0 and 1 is capable of capturing the bypass transition. However, studies involving laminar separation bubbles showed that this concept estimates the reattachment point at too far downstream [77]. To compensate this, a separation intermittency function, which can be greater than 1 when the laminar flow separates, is combined with γ. This provides a large production of turbulence so that an early reattachment is acquired.

1.1.3 Cavity Flow

Cavity flow is observed around the cavities in aerodynamic structures, which are exposed to intense turbulent and acoustic fields at relatively high speeds. It causes noise, vibration, fatigue, and drag force, which should be avoided for aerodynamic and structural efficiency. Two important examples to such cavities include those found in landing gear housings in commercial airplanes and weapon bays on military aircraft [30, 31] (see Figure 1.2). During landing, extension of the landing gear forms a resonant cavity creating noise almost at the same level as the propulsion unit [5, 39, 65]. On the other hand, the effect of cavity flow occurred in military aircraft is more harmful. Rockets, bombs and similar stores are carried inside the fuselage both

for low observability and preventing performance degradation. The problem appears when these stores are dropped, such that airflow immediately rushes in and over the arising cavity. This in turn causes highly turbulent flow which causes noise and vibrational loads [65, 74, 95]. Level of these loads on the store might even exhibit an entirely unsafe operation due to a possible crash of it to the fuselage [98, 112]. In addition, vortices created by all these cavities could increase the induced drag upto 250% [95]. Apart from the aviation industry, cavity flow can be observed in automobiles. For instance, open sunroof and side windows create noise and decrease the aerodynamic performance [23, 35].



(a) Landing gear housings during landing [100]

(b) Weapon bay in a F-22 fighter during store separation [33]

Figure 1.2: Examples of cavities in aerodynamic structures

Cavity flows contain a wide range of complex flow phenomena, particularly at transonic and supersonic flow velocities. These are separation, flow instability, 3-D effects, unsteadiness, secondary flows (corner flows), and reattachment [65, 95, 104]. It is not straightforward to analyze these flow fields by analytical and numerical approaches. Hence, at first, experiments were conducted to find out the fundamental behaviors of cavity flows [57, 96, 97]. Rossiter is one of the pioneers who observed that a depth and a length of a cavity (see Figure 1.3) directly influence its flow characteristics. His experiments showed that as the cavity becomes deeper, waves having narrow-band frequencies occur, and vice versa. Then, he developed a semi-empirical formula that calculates the frequency of highly-intense and narrow-band tones. These tones are called Rossiter modes. This formula (valid for Mach numbers between 0.4 and 1.4) and its enhancements (valid for all Mach regimes) [44] are still being used

to estimate the Rossiter modes (see Appendix A for the original equation).

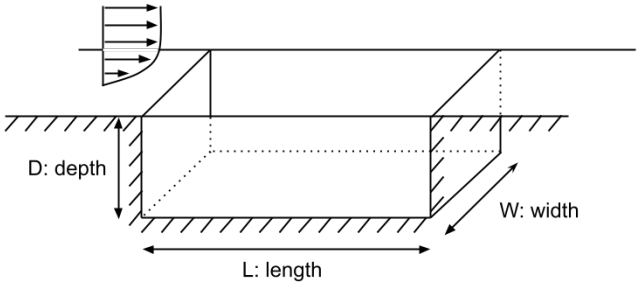


Figure 1.3: Flow over a typical cavity geometry

Today, it is well-known that the ratio of the cavity length to depth directly influences the unsteady flow character, from length scales to frequency scales of the turbulent structures. According to this ratio, cavity flow types are classified as:

- Open (deep) cavity flow: $L/D \leq 10$
- Closed (shallow) cavity flow: $L/D > 13$
- Transitional cavity flow: $10 < L/D \leq 13$

where L represents the cavity length (streamwise length) and D represents the cavity depth (normalwise length). On the other hand, the cavity width (W, spanwise length) affects the boundaries of L/D at subsonic and transonic velocities mostly [90]. The above boundaries are valid for $W/D = 1$. As W/D increases, the transition region expands to $9 - 14$. Dimensions of a typical cavity geometry is shown in Figure 1.3.

Presented in Figure 1.4 is a schematic of the cavity flow where solid lines represent the open cavity flow, and dashed lines represent the closed cavity flow. In closed and transitional cavities, flow separating from the upstream edge strikes the ceiling of the cavity, and then gets separated and diverted to the downstream edge. This causes a significant variation in pressure along the mouth of the cavity. Low pressure around the upstream edge and high pressure around the opposing edge yield an unwanted pitching moment on the deployed missile or bomb, putting the store separation in danger. This is why the use of closed and transitional cavity geometries are mostly avoided in military aircraft. Instead, open cavities, where the separated flow strikes

the downstream edge of the aft wall directly, are preferred thanks to an occurrence of nearly uniform pressure distribution. In this case, however, impingement of the shear layer leads to noise as well as vibration. Moreover, the upstream propagating acoustic waves increase the instability of the shear layer forming a feedback mechanism, as shown in Figure 1.5, and thereby complicating the problem. Therefore, modifications to the aft wall are more effective to suppress this mechanism [95]. Supersonic flow regime increases the instability as well. In this case, oblique shock happens at the downstream edge. Then, boundary layer thickens and shear layer instability starts earlier. As a consequence, sound levels of high frequency waves become higher than those in case of subsonic flows [69]. A typical open cavity noise spectrum is shown in Figure 1.6. In this spectrum, broadband noise is composed by the shear layer separation from the incoming turbulent boundary layer whereas intense and narrow-band discrete tones, which are the Rossiter modes, are generated by the feedback mechanism [97, 95, 65].

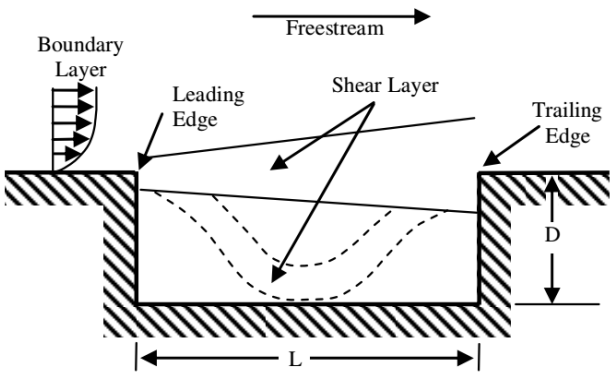


Figure 1.4: Schematic of the cavity flow (solid line: open cavity, dashed line: closed cavity) [66]

There are still unclear flow behaviors in cavity problems. Although the traditional signal processing methods have shown that the Rossiter (pressure) modes have constant magnitudes in time, some experiments revealed a change of dominant modes in time in case of open cavity flows [50]. This is called as mode-switching. According to the studies, energies of modes exchange between each other and this results in a shifting of the dominant ones. However, mode-switching phenomena is still a question whether it occurs in all cavity problems.

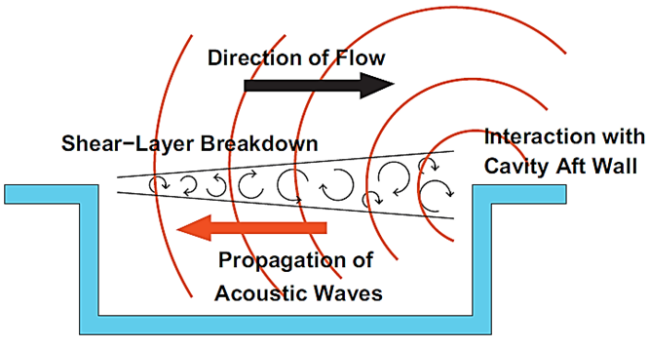


Figure 1.5: Acoustic feedback mechanism occurring in the open cavity flow [65]

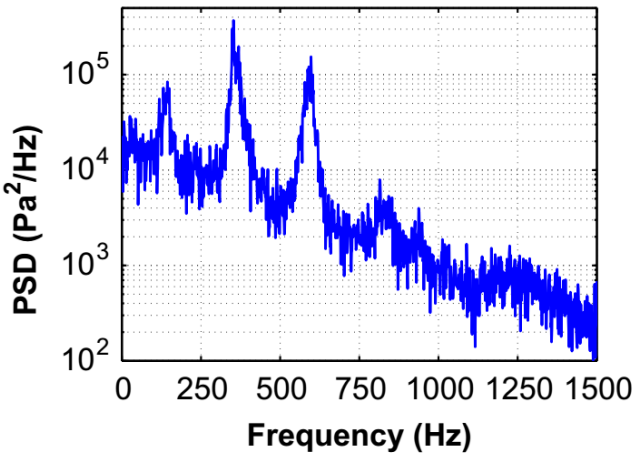


Figure 1.6: Broadband noise spectrum with Rossiter modes inside an open cavity [65]

In early experiments, use of equipments such as pitot-tubes or pressure transducers, that were in contact with unsteady turbulent flow field, had influenced the flow characteristics. Accordingly, early cavity experiments were conducted by Shadowgraph or Schlieren Photography techniques, which do not interfere with the flow [15, 57, 97]. In these results, dominant acoustic tones with narrow-band frequency were observed, and they were called Rossiter modes. However, since it was difficult to increase the spatial resolution in these techniques, broadband frequency spectrum could not be obtained. Later on, modern experimental equipments such as Particle Image Velocimetry (PIV) and Laser Doppler Velocimetry (LDV) were developed and high resolution observations in cavity flows could be made [42, 41]. Nevertheless, these equipments are expensive, and they have low resolution in time. Increasing spatial and temporal resolutions at the same time is challenging; limited to flow problems with Re of

order 10^5 while most cavity flows at relatively high speeds have at least Re of order 10^6. Therefore, experimental approaches are not adequate and effective to analyze this kind of problem with its all aspects.

Numerical studies, in recent years, have shown that CFD has rhe capability to increase the flow field resolution in both space and time. The numerical algorithms developed have lowered both the grid cell and iteration number requirements; thereby, steady problems with high Re could be resolved accurately. However, resolving unsteady turbulent flows is still quite a challenge as Re increases. Cavity problems, at first, was treated as 2-D flow. Even though the fundamental behavior of cavity flow, shear layer development, is 2-D, the vortices created at downstream and upstream edges make the flow field 3-D [92]. This is why 3-D solvers obtain results closer to the measurements than 2-D ones [65].

Considering the requirements of small time steps and fine grid domains, use of DNS is not realistic for cavity flows even with modern computing resources. In literature, there are some DNS studies that analyze flows with low Re and/or 2-D problems [20, 37, 43, 99]. These studies generally indicate the noise generation mechanism of cavity flows. URANS applications showed that it is not capable of resolving broadband spectrum of cavity problems [2, 81, 43, 38, 113]. It could only capture the main acoustic tones with low frequencies because of its modeling approach in the whole domain. Although high frequency waves have low energies, they cause noise as well as fatigue in cavity structures [2]. This is why prediction of the whole spectrum is essential. One of the reasons of failure is that modeling of all scales leads to an overproduction of eddy viscosities, especially near the wall corners. Another reason is that URANS could not diffuse the energies of fluctuations in the lateral direction accurately. Nevertheless, URANS gives reasonable results in those problems in which the cavity doors are 90° open since the doors restrict the three-dimensionality of the flow [81]. On the other side, LES studies provide better prediction of broadband spectrum than URANS because of their resolving most of the waves [6, 37, 59, 63, 81, 62, 93]. However, LES applications are excessively expensive due to high Re and presence of 5 walls inside the cavity domain. In addition, LES based on a scale invariance approach (Smagorinsky subgrid model) encounters a difficulty to model subgrid (filtered) scales near the aft corner regions where high vortical structures with

relatively low Re exist [37, 59, 63]. This causes redundant contribution of subgrid eddies to resolved (large) ones, resulting in increase of the narrow-band acoustic tones [6, 59, 63]. Instead, Improved LES (ILES) and Monotone Integrated LES (MILES) techniques, which add a filtered scales effect through special numerical algorithms, provide more plausible results [62].

Studies using DES have shown quite good agreement with experimental results, particularly in obtaining the shape of the sound level spectrum [43, 2, 81, 82, 86, 85, 51, 69]. These problems include subsonic and supersonic flows over cavities with and without weapons. The corresponding results can reach accuracy levels similar to those yielded by LES, but on much coarser grids due to RANS resolutions near the walls. It is also found that DES is superior to RANS for all tonal modes as well as the broadband noise, as expected. Furthermore, some recent flow control techniques aiming to reduce the noise and vibration levels have been examined via DES approaches [81, 51]. Apart from the weapon bays, cavity flows caused by landing gears have successfully being studied using DES [61]. However, an overprediction in the Overall Sound Pressure Levels (OASPL) along the cavity ceiling is reported in the studies with standard DES approaches although the spectrum trend is perfectly captured. In the Sound Pressure Levels (SPL), the frequencies of the Rossiter modes and the broadband noise are estimated well, but the magnitudes of the modes are overpredicted while the high-frequency content is underpredicted [43, 2]. These mispredictions are in the range of $5 - 10$ dB. The mismatches increases in the Power Spectral Density (PSD) analysis. Those are mainly related to the uncertain transition between the RANS and the LES regions. There are some enhancements to DES, over the last years, in an aim to improve and extend its capabilities (see Section 1.1.1 for details); however, its implementations in cavity flows are seldom. Luo et al. have performed IDDES over an open cavity for transonic and supersonic flows and improved the velocity and turbulent kinetic energy profiles around the rear wall compared to DES [69, 70]. Around the front wall where the shear layer instabilities dominate, the fluctuations could not be predicted as such. They commented that the slow transition from the RANS mode to the LES mode might be the reason. Along the cavity ceiling, the OASPL results as well as the magnitudes of the Rossiter modes perfectly matches with the measurements. The magnitudes in higher frequencies are

overpredicted though. Additionally, the narrow-band frequencies reveal upto 30 Hz deviations. As a final remark, DES simulations based on different turbulence closure models obtain very similar acoustic results for cavity flows [2] as the flow field is dominated by the large eddies inherently.

1.2 Motivation of the Thesis

Past knowledge on complex flow problems such as cavity noise and boundary layer transition was mostly based on experimental studies. However, probes used to measure flow quantities were in direct contact and hence in interaction with the flow itself. Instead of such conventional probes, modern techniques such as PIV and LDV are often used to measure quantities of unsteady flow phenomena, making more accurate measurements possible. These techniques are quite expensive though, and they limit Re of interest. On the other hand, CFD methods are favored more today due to tremendous improvements achieved in computer power and numerical algorithms. They also enable resolution increments both in time and space as long as sufficient computational resources are provided. Commercial CFD softwares are commonly used in industrial establishments due to the availability of wide range of physical and algorithmic models. However, the algorithmic models are usually limited to conventional low-order methods, which are not necessarily the best for resolving unsteady flow field and acoustic environment. On the other hand, on a given computational mesh high-order methods provide better resolution of the scales, and this fact directs many research institutions and universities to develop their own high-order flow solvers. One other important point is that commercial software updates are not as fast as the progress made in turbulence modeling. In-house research codes are better platforms to incorporate such fast developments. There is a high-order aeroacoustic in-house solver recently developed in Aerospace Engineering Department at Middle East Technical University, and named as METUDES [14, 12, 126]. This is a parallel code written in Fortran 95 and based on the finite volume approach. It solves the N-S equations using the algorithms which preserve the dispersion and dissipation characteristics of acoustic waves. The turbulence closure is obtained by solving the S-A one-equation model. The eddy modeling and resolving issues are managed by

the DES approach since DES reduces the necessity of a very fine grid in high Re wall-bounded flows while keeping the accuracy of the results high. This thesis aims to enhance the METUDES flow solver towards accurately capturing turbulent and acoustic flow fields around the cavities in aerodynamic structures as well as transitional flow over the wing/blade profiles. The enhancement is intended to be realized mostly using a hybrid scheme of DES because the switching between the RANS and the LES modes restricts the application of DES. As already discussed, the problems mentioned are out of the scope of DES. Despite its improvements over the last years, their implementations in the cavity as well as the transitional flow cases are very limited and recent. Besides, an efficient DES method that captures these kinds of flow physics with minimum additional computational effort (compared to the original version) has not become available yet. These points form the motivation of the thesis.

1.3 Proposed Methods and Models

1.3.1 Cavity Flow Part

In this thesis, open cavity flow is studied since open cavities are important in the design processes of weapon bays in military aircraft in order to ensure a safe store separation. The M219 cavity model has tremendous experimental and numerical validation data in literature; therefore, this model is selected to simulate. The geometric dimensions are an L/D of 5 and a W/D of 1. As mentioned, it causes a tonal noise with broadband spectrum. Open cavity noise is dominated by two main mechanisms: shear layer instability starting from the front corner and the impingement of this shear layer on the aft wall. DES requires an immediate activation of the LES region after separation of the incoming flow because 2-D K-H instability waves are highly unstable such that 3-D breakdown happens quickly. In addition, the eddy resolution level should be increased very near the reattachment surface, which represents the region around the aft wall in open cavities. In this respect, following methods are proposed:

- The SLA subgrid length scale is used to provide rapid transition from the RANS mode to the LES one when the K-H instability is detected.

- The IDDES method is selected for simulations so that an LES content could be increased by the WMLES approach, stepping in the impingement zone while the rest is performed by DDES, ensuring the RANS modeling inside the attached boundary layers.
- METUDES has already an SLA option, which can be used with DES and DDES. During this study, IDDES is implemented, and the SLA length scale is incorporated into IDDES.

On the other hand, METUDES is a single-block solver on structured mesh domains. Although cavity structures are generally simple rectangular prisms, multiblock domains are required to generate a mesh including both the outer and the inner flow fields. Hence,

- a multiblock structured grid topology with one-to-one interface communication is implemented in the solver.

In addition, METUDES has been used for flow over a blade profile problems thus far involving only 1 viscous wall boundary. In the cavity problem, there are 5 walls just inside the cavity where wall boundary conditions are applied in all three directions. Those increase the complexity of the flow field which is prone to worsen the convergence and stability behavior as it changes the stiffness characteristic of the flow equations. As a result, the convergence acceleration techniques already implemented in the dual-time stepping algorithm of the solver are improved as follows:

- The residual smoothing algorithm used for the N-S equations is modified and a residual smoothing for the turbulent model equation is added.
- Dissipation for shock capturing while solving the turbulent equation is enhanced with the TVD (Total Variation Diminishing) shock sensor.
- A biased artificial dissipation is added to be activated in grid cells near the solid walls.
- A scaling factor is added to the artificial dissipation of the turbulent equation for high aspect-ratio cells which exist along the shear layer at the cavity mouth.

1.3.2 Transitional Flow Part

METUDES was developed for wind turbine blade simulations, but it treats the entire flow field as fully turbulent. It solves a modified version of the S-A equation by Crivellini et al. [21] which gives an opportunity to start the simulations with almost zero eddy viscosity. As discussed in Section 1.1.2, laminar-to-turbulent transition is taking essential part of the aerodynamic predictions, particularly the maximum lift coefficient for the blades. Thus, performing transitional DES is the other target of the thesis. Wind turbine blades are thick in which a laminar separation and the bypass transition might be observed at the same flow condition. Hence, it is intended to capture both the bypass and the separation-induced transitions. On the other hand, the solver already solves 6 partial differential equations together with the S-A model equation. Moreover, computation of the high-order low-dissipation low-dispersion schemes brings an additional cost. This leads to an idea that the fully turbulent RANS equations should be incorporated with a zero-equation transition model. Lastly, the wake resolution is another important issue in this kind of problems for estimating the aerodynamic coefficients. In the light of all the above information, following methods are proposed:

- For all types of transition, in order to predict the exact transition onset location, the modified version of the B-C (BCM) algebraic correlation-based model [10] is implemented in the solver.
- For the separation-induced transition, the SLA length scale is used to detect the K-H instability observed in laminar separation bubbles, and then to switch to the resolution mode rapidly so that the 3-D content can be resolved.
- A new triggering term together with some modifications are proposed to combine the SLA length scale and the BCM model through DDES approach.
- The initial eddy viscosity value is set almost to zero, thanks to the modified S-A equation.
- A Chimera type overset grid technique compatible with the multiblock topology is implemented. This provides a creation of a sufficiently fine wake domain while keeping the grid cell number in reasonable levels. As the solver is based

on high-order schemes, a high-order interpolation proposed by Lee et al. [67] is used in the overset method.

1.4 The Outline of the Thesis

The rest of the thesis proceeds with a methodology chapter that includes the introduction of the flow solver as well as the implementations of the new methods. Next, a chapter of simulation setups describing the grid generation strategy, boundary conditions, initial conditions, and time step selection is presented. The thesis continues with some simulations in order to validate the code implementations. After that, the results of transitional and cavity flow simulations are shown in comparison to available experimental and numerical data from literature. This thesis presentation is finalized by conclusions and future suggestions.

CHAPTER 2

METHODOLOGY

All numerical simulations conducted in this thesis are performed by the METUDES flow solver. In this regard, this chapter starts with a brief introduction to the solver including the flow equations, numerical approaches, and the structure of the code. Then, it continues with a detailed description and formulation of the methods which were not available in METUDES but required for the corresponding simulations, thereby being implemented in the solver.

2.1 METUDES - Flow Solver

METUDES is an in-house flow solver which has been developed in the Department of Aerospace Engineering at the Middle East Technical University. The development of the solver was initiated from scratch [12] originally for wind turbine blade noise predictions under a TÜBİTAK 1001 project grant no. 112M106 [14]. This project resulted in one MSc thesis [126], one PhD thesis [12], and thereby a few early versions of METUDES. The development of this solver was continued after the completion of the project with some added capabilities. The features of the version leading to this thesis are briefly described first in the following sections:

2.1.1 Favre-Averaged Navier-Stokes Equations

METUDES solves 3-D, time-dependent, compressible, Favre-averaged Navier-Stokes equations, together with a modified version of Spalart-Allmaras turbulence equation simultaneously. The Favre averaging process [32] is a mathematical simplification of

the RANS equations for compressible flows. The Favre averaging of any instantaneous quantity (let say ϕ) is obtained as

$$\tilde{\phi} = \frac{\overline{\rho\phi}}{\bar{\rho}} = \frac{\frac{1}{T}\int_t^{t+T} \rho(x_i,\tau)\phi(x_i,\tau)d\tau}{\frac{1}{T}\int_t^{t+T} \rho(x_i,\tau)d\tau} \tag{2.1}$$

where ρ is density, x_i denotes the space vector, t denotes time, and τ denotes a dummy integration variable. Here, tilde and overbar represent the Favre averaging and Reynolds averaging, respectively. The Favre averaging simply computes the density-weighted averaged of ϕ using the Reynolds averaging process that is realized over a time interval, T. In this way, the additional correlation terms due to the density fluctuation are eliminated.

The Favre-averaged Navier-Stokes (FANS) equations are composed of continuity, momentum, and energy equations, which can be written using the Einstein index notation as follows,

$$\begin{aligned}
\frac{\partial\bar{\rho}}{\partial t} + \frac{\partial}{\partial x_i}(\bar{\rho}\tilde{u}_i) &= 0, \\
\frac{\partial\bar{\rho}\tilde{u}_i}{\partial t} + \frac{\partial}{\partial x_j}(\bar{\rho}\tilde{u}_j\tilde{u}_i) &= -\frac{\partial\bar{p}}{\partial x_i} + \frac{\partial\bar{\tau}_{ji}}{\partial x_j}, \\
\frac{\partial\bar{\rho}\tilde{E}}{\partial t} + \frac{\partial}{\partial x_i}\left[(\bar{\rho}\tilde{E}+\bar{p})\tilde{u}_i\right] &= \frac{\partial}{\partial x_i}(\bar{\tau}_{ij}\tilde{u}_j - \bar{q}_i)
\end{aligned} \tag{2.2}$$

where u_i is the velocity vector, and p is pressure. E represents the total energy and obtained as $\tilde{E} = \bar{p}/\left[\bar{\rho}(\gamma-1)\right] + \tilde{u}_i^2/2$ where γ is the heat capacity ratio. After the Boussinesq hypothesis is applied, the Reynolds stress, emanating from the averaging process, is governed by an eddy viscosity concept; therefore, the shear stress (τ_{ij}) and the heat flux (q_i) terms are defined as

$$\begin{aligned}
\bar{\tau}_{ij} &= (\mu+\mu_t)\left[\left(\frac{\partial\tilde{u}_i}{\partial x_j} + \frac{\partial\tilde{u}_j}{\partial x_i}\right) - \frac{2}{3}\delta_{ij}\frac{\partial\tilde{u}_j}{\partial x_j}\right] \\
\bar{q}_i &= -\left(\frac{\mu}{Pr(\gamma-1)} + \frac{\mu_t}{Pr_t(\gamma-1)}\right)\frac{\partial\tilde{T}}{\partial x_i}
\end{aligned} \tag{2.3}$$

where μ and μ_t are the molecular dynamic viscosity and the eddy viscosity, whereas Pr and Pr_t are Prandtl and turbulent Prandtl numbers, respectively. δ_{ij} represents the Kronecker delta, and T denotes temperature. One may notice that density and pressure terms in the equations are not Favre-averaged; they are just Reynolds-averaged.

In the FANS equations, there are 7 unknowns: ρ, u_i (3 components), p, T, and μ_t. In order to solve them, at least 7 equations are required: 5 of them are the FANS equations, and 1 of them comes from the ideal gas law, which is

$$\bar{p} = \bar{\rho} R \tilde{T} \tag{2.4}$$

where R is the gas constant. The remaining equation for closure is the S-A turbulence model equation, which solves μ_t.

2.1.2 Spalart-Allmaras One-Equation Model

A modified version of the S-A turbulence model equation proposed by Crivellini et al. [22] is used in METUDES. This is a transport equation solving a turbulence-related variable, $\hat{\nu_t}$, and the equation may be written as

$$\frac{\partial \hat{\nu_t}}{\partial t} + \tilde{u}_i \frac{\partial \hat{\nu_t}}{\partial x_i} = \Psi + \Pi - \Phi \tag{2.5}$$

where Ψ, Π, and Φ are the source terms and denote diffusion, production, and destruction, respectively. The turbulence-related variable is used to compute the kinematic eddy viscosity, ν_t, and then μ_t as follows,

$$\begin{aligned} \nu_t &= f_{v1} \max(\hat{\nu_t}, 0), \\ \mu_t &= \rho \nu_t \end{aligned} \tag{2.6}$$

where $f_{v1} = \chi^3/(\chi^3 + c_{v1}^3)$, and $\chi = \hat{\nu_t}/\nu$. ν is the kinematic molecular viscosity, whereas c_{v1} is a constant. Since the solver does not enforce a laminar suppression

with a tripping mechanism, the trip term, f_{t2}, in the original equation is taken as zero. Thus, the right hand side terms without f_{t2} are calculated as

$$\Psi = \frac{\partial}{\partial x_i}\left(\frac{\nu + \max(\hat{\nu}_t, 0)}{\sigma}\frac{\partial \hat{\nu}_t}{\partial x_i}\right), \tag{2.7a}$$

$$\Pi - \Phi = \begin{cases} 0, & \hat{\nu}_t < 0 \\ \left(\dfrac{c_{b1}}{\kappa^2 r} - c_{w1} f_w\right)\left(\dfrac{\hat{\nu}_t}{d_w}\right)^2 + \dfrac{c_{b2}}{\sigma}\left|\dfrac{\partial \hat{\nu}_t}{\partial x_i}\right|^2, & \hat{\nu}_t \geq 0 \end{cases} \tag{2.7b}$$

where

$$r = \begin{cases} r_{max}, & r^* < 0 \\ \min\left(r^*, r_{max}\right), & r^* \geq 0 \end{cases}, \tag{2.8a}$$

$$r^* = \left(\frac{S\kappa^2 d_w^2}{\hat{\nu}_t} + f_{v2}\right)^{-1}. \tag{2.8b}$$

S denotes the vorticity magnitude which is computed as $S = \left|\epsilon_{ijk}\dfrac{\partial \tilde{u}_k}{\partial x_j}\right|$. In addition, d_w is the nearest wall distance. The remaining variables are obtained as follows,

$$f_{v2} = 1 - \frac{\chi}{1 + \chi f_{v1}}, \quad f_w = g\left[\frac{1 + c_{w3}^6}{g^6 + c_{w3}^6}\right]^{1/6}, \quad g = r + c_{w2}(r^6 - r). \tag{2.9}$$

Finally, all constants appearing in the equations so far are given as

$$\begin{aligned} \sigma = 2/3,\ c_{b1} = 0.1355,\ c_{b2} = 0.622,\ \kappa = 0.41,\ c_{w1} = \frac{c_{b1}}{\kappa^2} + \frac{1 + c_{b2}}{\sigma}, \\ c_{w2} = 0.3,\ c_{w3} = 2,\ c_{v1} = 7.1,\ r_{max} = 10. \end{aligned} \tag{2.10}$$

This modified version differs from the original S-A model equation [3] mostly in the source term calculations, curing the problem of negative $\hat{\nu}_t$ values and related numerical instabilities. On the other hand, these modifications give an opportunity to set the initial eddy viscosity values as zero throughout the computational domain.

This provides an apparent laminar-to-turbulent transition behavior, especially when a transition is induced by laminar separation bubbles [21, 13]. Consequently, the most of the simulations in this thesis started by setting an initial value of $\hat{\nu}_{t\infty}/\nu$ as 10^{-8} where the subscription of ∞ represents the freestream.

2.1.3 Turbulence Modeling and Resolving

Resolving all eddies throughout the computational domain with 3-D, unsteady, high Re flow fields is unlikely when considering the computational resources by year 2030 [72]. Instead, METUDES models eddies partly or completely using URANS and DES strategies, which are described mathematically in the following sections.

2.1.3.1 Unsteady Reynolds-Averaged Navier-Stokes

The URANS simulation approach models all scales of eddies. The modeling is carried out through the turbulence model length scale which is the wall distance term, d_w, appearing in the source terms of the S-A model equation (see Equation 2.7b). That is, the RANS (model) length scale is obtained as

$$l_{\text{RANS}} = d_w. \tag{2.11}$$

As fluid particles flow near a solid wall, the length scale becomes very small, and thereby increasing the destruction term extremely. This suppresses the eddy formation in the viscous sublayer as expected. On the other hand, as the particles move away from the wall, the eddy viscosity starts to generate. After a certain distance, the destruction effect due to the model length totally dissipates and the eddy viscosity continues increasing and diffusing as long as the numerical dissipation allows.

2.1.3.2 Detached-Eddy Simulation

DES [108] is a hybrid RANS/LES approach based on the RANS equations. It essentially models eddies in the boundary layer by its RANS mode, and resolves them

away from the boundary layer and/or in separated regions by its LES mode. DES makes a switching between these modes through the turbulence model length scale as

$$l_{\text{DES}} = \min(l_{\text{RANS}}, l_{\text{LES}}). \tag{2.12}$$

Here, $l_{\text{LES}} = C_{\text{DES}}\Delta$ where C_{DES} is 0.65, and Δ is the subgrid length scale, which is taken as the local maximum cell dimension, Δ_{max}. In the desired DES grid, $\Delta_{max} >> \delta$ in attached flow regions where δ represents the boundary layer thickness. This ensures that the RANS modeling is kept inside the boundary layer since DES chooses d_w as the length scale. After a separation, since the rapidly growing δ becomes higher than Δ_{max}, the LES mode takes place. Henceforth, the length scale serves as a subgrid scale. Because this is a massive separation, large eddies dominate the field such that the grid resolution by Δ_{max} suffices for eddy resolution. In this field, the destruction term of the S-A equation still exists, unlike URANS, and provides a reduction of eddy viscosity.

2.1.3.3 Delayed Detached-Eddy Simulation

The switching mechanism of DES is totally mesh dependent. If a grid is designed improperly, that is Δ_{max} of some cells becomes smaller than δ inside an attached boundary layer, DES switches to the LES mode earlier. In other words, the grey-area between RANS and LES regions shifts inside the boundary layer. At this point, the subgrid scales (eddies smaller than Δ_{max}), which should be modeled by the RANS mode, could not be resolved. This causes MSD and/or GIS problems, as discussed in Section 1.1.1. The DDES approach [109] ensures to keep the modeling mode inside the boundary layer by modifying the DES length scale as follows,

$$l_{\text{DDES}} = l_{\text{RANS}} - f_d \max(0, l_{\text{RANS}} - \Psi C_{\text{DES}}\Delta_{max}). \tag{2.13}$$

Here, f_d is a delaying function which delays the LES activation in the boundary layer

and it is computed as

$$f_d = 1 - \tanh\left([8r_d]^3\right) \tag{2.14a}$$

$$r_d = \frac{\nu_t + \nu}{\left(\frac{\partial \tilde{u}_i}{\partial x_j}\frac{\partial \tilde{u}_i}{\partial x_j}\right)^{0.5} \kappa^2 d_w^2} \tag{2.14b}$$

where κ is Karman constant and equals to 0.41. By this formulation, in attached boundary layers f_d goes to 0 and makes $l_{\text{DDES}} = l_{\text{RANS}}$, whereas in other regions it returns to the original DES formulation (Equation 2.12). On the other hand, Ψ is a low Re correction term which prevents an excessive reduction of eddy viscosity values in the low Re regions and/or in case of an overmuch grid refinement. It is calculated as (without the trip term)

$$\Psi = \sqrt{\min\left(10^2, \frac{1 - \frac{c_{b1} f_{v2}}{c_{w1}\kappa^2 0.424}}{f_{v1}}\right)}. \tag{2.15}$$

2.1.3.4 Shear-Layer-Adapted Subgrid Length Scale

The choice of Δ_{max} as a subgrid length scale is safe to keep the RANS functioning in the boundary layer. However, if prediction of a thin boundary layer separation, separated shear layers, and/or free shear layers is intended, Δ_{max} would be a bad choice as it damps and delays the K-H instability waves. The eddy viscosity should be lowered to release the K-H instability. For this purpose, the SLA subgrid length scale was proposed recently [106]. This approach, which depends not only on the grid but also on the flow, and its three-dimensionality, reduces the subgrid length scale by two levels. Firstly, a vorticity dependent subgrid length scale is defined as

$$\tilde{\Delta}_\omega = \frac{1}{\sqrt{3}} \max_{n,m=1,8} |I_{n,i} - I_{m,i}| \tag{2.16}$$

where $I_{n,i} = \epsilon_{ijk} n_{\omega,k} r_{n,j}$, and $n_{\omega,i}$ is the unit vorticity vector, whereas $r_{n,i}$ is the position vector for the vertices of the cell ($n = 1, ..8$ for hexahedral cells). This

formulation removes the dependence of subgrid viscosity on a cell length (mostly $\Delta_{max} = \Delta z$ for a shear layer in $x - y$ plane) in the vorticity direction, which had been a problem in shear layers where the planar shear is expected to initiate transition to the LES mode. Instead, the subgrid viscosity is based on the maximum dimension on the shear plane in a quasi-2D region. Still, the resulting reduction of the subgrid viscosity is not sufficient to initiate the transition in quasi-2D regions.

As a second level, an ILES-like behavior is used in such regions to allow the K-H instabilities to take over. The so-called "Vortex Tilting Measure" (VTM) function is defined to detect such regions:

$$VTM = \frac{\sqrt{6}|\epsilon_{ijk}(\hat{S}_{ij}\omega_j)\omega_j|}{|\omega_i|^2\sqrt{3tr(\hat{S}_{ij}\hat{S}_{jk}) - \left[tr(\hat{S}_{ij})\right]^2}} \tag{2.17}$$

where $\hat{S}_{ij}$ is the strain rate tensor, ω_i is the vorticity vector, and tr refers to trace. It yields zero when the vorticity is aligned with any eigenvectors of the strain; nonzero when the deformation tensor tilts the vorticity vector. VTM is facilitated in the function,

$$F_{KH}(\langle VTM\rangle) = \max\left[F_{KH}^{min}, \min\left\{F_{KH}^{max}, F_{KH}^{min} + \frac{F_{KH}^{max} - F_{KH}^{min}}{a_2 - a_1}(\langle VTM\rangle - a_1)\right\}\right] \tag{2.18}$$

where the angle bracket, $\langle\cdot\rangle$, means the value is averaged among neighboring cells. Averaging is necessary for smoothing the distribution since it is reported that VTM may have downward excursions locally. F_{KH} is a simple function depending on VTM with the sole purpose of reducing the subgrid viscosity properly. $F_{KH}^{max} = 1$ that recovers the original length scale, while $F_{KH}^{min} = 0.1$. a_1 and a_2 are constants that are adjusted through numerical experiments and equal to 0.15 and 0.3, respectively. Accordingly, F_{KH} varies linearly between $\langle VTM\rangle$ of 0.15 and $\langle VTM\rangle$ of 0.3 yielding values ranging from 0.1 to 1. Finally, the ultimate subgrid length scale is

calculated by

$$\Delta_{\text{SLA}} = \tilde{\Delta}_{\omega} F_{KH}(\langle VTM \rangle). \tag{2.19}$$

The resulting length scale serves as a reduction to $\tilde{\Delta}_{\omega}$ up to one order in regions where the K-H instabilities are expected to occur, thus leaving ground to transition to the resolved 3-D turbulent mode. However, for wall-bounded flows, this reduction should be inactivated to keep the boundary layer shielded as done in DDES with Δ_{max}. The following limitation to F_{KH} was proposed for that purpose:

$$F_{KH}^{lim} = \begin{cases} 1, & f_d < 0.99 \\ F_{KH}, & f_d \geq 0.99 \end{cases}. \tag{2.20}$$

Moreover, in order to avoid numerical oscillations in inviscid regions, $\langle VTM \rangle$ should be multiplied with $\max\left(1, \dfrac{0.2\nu}{\max(\nu_t - \nu_{t,\infty}, 10^{-6}\nu_{t,\infty})}\right)$. This makes F_{KH} 1 so that it is deactivated in inviscid regions.

The SLA subgrid length scale is implemented into DDES by simply replacing $\Delta_{\max}$ with Δ_{SLA}. Thus, this new length scale, called as DDES-SLA, becomes

$$l_{\text{DDES-SLA}} = l_{\text{RANS}} - f_d \max(0, l_{\text{RANS}} - \Psi C_{\text{DES}} \Delta_{\text{SLA}}). \tag{2.21}$$

Note that METUDES has another option as a DES strategy: Zonal DES (ZDES). However, ZDES is not described here as it is not used in the simulations.

2.1.4 Numerics

The numerical features of the solver are summarised in the following list:

- The governing equations are transformed from the physical domain to the computational domain by one-to-one mapping using metric terms. The flux computations of flow equations are realized on curvilinear structured single grids.

- The fluxes are discretized in space by the central finite volume scheme. For the FANS equations, a 4th-order accurate algorithm with the dispersion-relation-preserving (DRP) as well as the skew-symmetry schemes (suggested by Kok [54]) is performed. The 4th-order accurate central discretization provides low-dissipation, whereas the DRP scheme [118], requiring additional nodes in stencils, provides low-dispersion. In addition, the skew-symmetry algorithm preserves the kinetic energy. A prediction of acoustic waves in aeroacoustic simulations benefits greatly from this low-dissipation low-dispersion scheme. On the other hand, the fluxes of the S-A model equation is discretized by a 2nd-order accurate finite volume.

- Time integration is conducted in dual time stepping based on a 2nd-order backward difference, but solved in explicit iterative manner by adding a pseudo time derivative term [49]. The resulting explicit integration is computed using a 5-stage Runge-Kutta algorithm. The dual time stepping integration provides an opportunity to increase the CFL number, and thereby avoiding the restriction of time step in viscous wall-bounded flows.

- Preconditioning squared approach, based on a cooperation of low speed preconditioning and Jacobi preconditioning [119], is used for acceleration of a steady state flow convergence in subiterations of dual time steps. Low speed preconditioning removes the stiff behavior of flow equations at low Mach numbers. This stiffness is caused by a large discrepancy between the acoustic speed and the convective speed when the flow has low speed. Low speed preconditioning, in principle, makes the Courant number 1. On the other hand, Jacobi preconditioning enhances high frequency error damping by introducing a matrix-based artificial viscosity and using a matrix time stepping. Hence, the preconditioning squared provides a fast convergence to low Mach number steady state flows.

- A blended matrix artificial dissipation [91] is used to damp spurious high-frequency waves. This algorithm blends the preconditioners for both steady and unsteady flows to properly scale the artificial dissipation.

- Implicit residual smoothing [48] is also added to increase the convergence rate during the subiterations. In brief, a residual obtained after spatial discretiza-

tions is smoothed out by the Laplace operator using residuals of neighboring cells. The resulting tridiagonal system of equations in each direction is solved by the Thomas algorithm implicitly. Implicit residual smoothing results in an increment of the maximum CFL number by a factor of almost 2.

The detailed mathematical expressions of these numerical algorithms mentioned above can be found in [12].

2.1.5 Code Structure

METUDES is written in Fortran90/95 language. It is parallelized using OpenMPI libraries [34] for distributed memory machines. A master processor decomposes the computational mesh and distributes it to the others, and then, they all start to solve the equations simultaneously within their borders. After each subiteration, they communicate the required (shared) information with their neighboring processors in all directions by the send/receive routines of the MPI library. The paralellization of the solver with 3-D decomposition provides almost a linear speedup.

2.2 Improvements to METUDES

This section describes and discusses the improvements made to METUDES by the present thesis work. The incorporated features are geared especially towards both cavity and boundary layer transition simulations. The contributions are divided mainly into two categories: improvements to DDES frameworks, and improvements to numerics.

2.2.1 DDES Frameworks

2.2.1.1 Transitional DDES

Prediction of laminar-to-turbulent transition in flows over wing/turbine blade profiles has a key role in capturing the aerodynamic coefficients. Assuming fully turbulent

throughout the computational domain fails at this point. Despite starting DDES with almost laminar flow everywhere by the modification to the S-A equation, there is no information regarding the transition onset in the solver. In order to make DDES transitional, the Baş-Çakmakçıoğlu (B-C) transition model has been implemented in METUDES. Since transition begins in the RANS region, but may end in the LES region, the incorporation of the model into DDES frameworks requires special attention. This section presents the B-C model and its incorporation.

Baş-Çakmakçıoğlu Transition Model A modified version of the B-C model (BCM), which has been coded into the present solver, is a zero-equation correlation-based transition model [10]. It uses an intermittency function to trigger the transition. This function depending on local flow information is simply multiplied with the production term of the S-A equation:

$$\frac{\partial \hat{\nu}_t}{\partial t} + \tilde{u}_i \frac{\partial \hat{\nu}_t}{\partial x_i} = \Psi + \boldsymbol{\gamma}_{\text{BCM}} \Pi - \Phi. \tag{2.22}$$

The intermittency value, γ_{BCM}, is calculated algebraically through two terms: Term_1 is used to trigger transition in the outer boundary layer using the vorticity Reynolds number (Re_ν), and Term_2 transports the intermittency value, produced by Term_1, into the boundary layer. γ_{BCM} takes a value of 0 in laminar flow such that the production of eddy viscosity is prevented. As the transition criterion is met, γ_{BCM} abruptly goes to 1, thereby recovering the turbulence equation fully. The calculation is straightforward:

$$\gamma_{\text{BCM}} = 1 - \exp\left(-\sqrt{\text{Term}_1} - \sqrt{\text{Term}_2}\right) \tag{2.23}$$

$$\begin{aligned} \text{Term}_1 &= \frac{\max(Re_\theta - Re_{\theta c}, 0)}{\chi_1 Re_{\theta c}}, \\ \text{Term}_2 &= \frac{\max(\nu_t, 0)}{\chi_2 \nu} \end{aligned} \tag{2.24}$$

where

$$Re_\theta = \frac{Re_v}{2.193}, \quad Re_v = \frac{\rho d_w^2 \Omega}{\mu}. \tag{2.25}$$

Ω is the vorticity vector magnitude. $\chi_1 = 0.002$ and $\chi_2 = 0.02$ are the calibration constants. The critical momentum thickness Reynolds number, $\mathrm{Re}_{\theta c}$, is found from empirical correlations as

$$Re_{\theta c} = 803.73(\mathrm{Tu}_\infty + 0.6067)^{-1.027} \tag{2.26}$$

where Tu_∞ denotes the freestream turbulence intensity.

Incorporation of the BCM Model into DDES The BCM model was proposed for the RANS framework. The studies showed that the transition onset in steady transitional flows and corresponding aerodynamic results are well-estimated by the model [9, 10, 79]. It is remarkable to achieve these results without solving extra transport equations. The model benefits from the convection and diffusion terms of the already-solved turbulence equation. In principle, it makes the flow laminar upstream of the trigger point, and fully turbulent the entire downstream. However, the suitability of this model for time-dependent problems was studied in this thesis, and three deficiencies have been observed:

1. In unsteady flow problems, Term_1 becomes unstable in the vicinity of transition onset. This makes, at some instants, the intermittency function less than 1, which in turn affects the production term of the S-A equation instantly. This strong coupling between the transition and turbulence models as well as the absence of history effect of the intermittency function can hamper the eddy production. Under weak unsteadiness conditions such as large adverse pressure gradients, the time and length scales are big enough to reduce the unsteadiness effect on Term_1, resulting in a persistent intermittency value (see Section 5.2 presenting a flow problem over a circular cylinder). Contrarily, in strong

unsteadiness the persistence is lost (see Section 5.1 presenting a flow problem over a blade section).

2. In the LES mode of DDES, the balance between the production and the destruction terms is essential for the performance of the subgrid scale model. Although the LES region in DDES is supposed to be fully turbulent such that the balance is already ensured, the LES mode might be activated in early transition region in case of DDES-SLA. In this context, the multiplication of the intermittency function only with the production term becomes a problem.

3. The SLA subgrid length scale reduces the eddy viscosity in quasi-2D regions of K-H instabilities in accordance with its purpose. In separation-induced transition cases, Term_1 is expected to trigger transition around the K-H instability waves. When the BCM model is directly used in the DDES-SLA simulations, even though the intermittency function is triggered successfully, it may not be penetrated into the boundary layer as desired (see Section 5.1.2.2). The reason is that Term_2 is calibrated according to the RANS eddy viscosity, which is much higher than the DDES-SLA one.

All of three deficiencies could be overcome by decoupling the transition and the turbulence model, and solving another transport equation for the intermittency function, as discussed in Section 1.1.2. Instead, three improvements to the BCM transition model are proposed to stick with the algebraic model approach [1]:

1. For the 1st deficiency mentioned above, an additional term, called Term_3, to be inserted in γ_{BCM} calculation is proposed. This term is designed to trigger transition due to slight separations in unsteady flows such as laminar separation bubbles where both time and length scales are small. In this regard, Term_3 is formulated by benefiting from the VTM sensor used in the SLA calculations (see Section 2.1.3.4). This sensor works as a detector of quasi-2D K-H instability waves which are expected to initiate transition in separated shear layers.

[1] The mentioned improvements have been developed by a collaborative work with Dr. Kenan Cengiz. For details about calibrations and initial attempts, see [127]

The new γ_{BCM} and Term_3 are computed as follows,

$$\gamma_{\text{BCM}} = 1 - \exp\left(-\sqrt{\text{Term}_1} - \sqrt{\text{Term}_2} - \text{Term}_3\right), \tag{2.27}$$

$$\text{Term}_3 = f_d(\chi_3\langle VTM\rangle)^p \tag{2.28}$$

where f_d, the delaying function of DDES (Equation 2.14a), provides to make Term_3 active only outer attached boundary layer. $\langle VTM\rangle$ is the "Vortex Tilting Measure" function of DDES-SLA (Equation 2.17). The constants of χ_3 and p are calibrated to make γ_{BCM} as 1 quickly when $\langle VTM\rangle$ is close to 0.15. Note that $\langle VTM\rangle$ is 0 in quasi-2D regions, and larger than 0.3 in fully developed turbulence regions. In DDES-SLA simulations, when $\langle VTM\rangle$ is between 0 and 0.15, F_{KH} is kept constant as 0.1, which increases the destruction term of the S-A model equation 100 times. This ensures an ILES behavior (i.e. "no model"). After $\langle VTM\rangle = 0.15$, F_{KH} starts to increase and the destruction term reduces accordingly; therefore, eddy production is allowed. This is why $\langle VTM\rangle = 0.15$ is targeted while calibration. As a result, χ_3 and p are set as 12 and 6, respectively.

2. Regarding the 2nd deficiency, a balance between the source terms of the turbulence equation can be easily preserved by replacing Equation 2.22 with

$$\frac{\partial\hat{\nu_t}}{\partial t} + \tilde{u}_i\frac{\partial\hat{\nu_t}}{\partial x_i} = \Psi + \boldsymbol{\gamma}_{\text{BCM}}\Pi - \boldsymbol{\gamma}_{\text{BCM}}\Phi. \tag{2.29}$$

Here, the intermittency function is multiplied with not only the production term but also the destruction term.

3. The last proposal, related to the 3rd deficiency, is to rearrange Term_2 as

$$\text{Term}_2 = \frac{\max\left(\frac{\nu_t}{F_{KH}^2}, 0\right)}{\chi_2\nu} \tag{2.30}$$

where F_{KH} is already used in DDES-SLA to reduce the SLA subgrid length scale (Equations 2.18 and 2.19). In case of the SLA reduction, this proposed approach scales the eddy viscosity appearing in Term_2 up to the level used in

calibration. This means the reduced eddy viscosity is increased by the same amount as the destruction term. Thus, Term_2 can transport the generated intermittency function into the boundary layer as desired. Note that when there is no SLA reduction, F_{KH} takes the value of 1 such that the term returns to its original version.

The first and the third methods are proposed only for the DDES-SLA framework. As the new functions are already computed for Δ_{SLA}, they do not cause an additional computational load to the BCM model. For the pure DDES, on the other hand, the first method is suggested to include in case of a strong unsteadiness in flow field even there is an additional VTM calculation. In the rest of the study, DDES with the BCM model called DDES-BCM which includes only the second proposed method. Likewise, DDES-SLA with the BCM model includes all of the proposed methods, and called DDES-SLA-BCM3 ("3" comes from Term_3 which covers the largest part of the modifications).

2.2.1.2 Improved Delayed Detached-Eddy Simulation

The IDDES method [105] is a combination of DDES and WMLES approaches. It behaves like WMLES if there is an unsteady inflow turbulent content as well as the grid resolution is sufficient. In other conditions, it acts as DDES exactly. In the WMLES branch, IDDES shifts the RANS/LES border from the boundary layer edge (or above it) to approximately the end of the inner layer. This results in a turbulence resolution increment as desired. The turbulent length scale of IDDES is computed as

$$l_{\text{IDDES}} = \tilde{f}_d(1 + f_e)d_w + (1 - \tilde{f}_d)C_{\text{DES}}\Delta_{\text{IDDES}}. \tag{2.31}$$

Here, $\tilde{f}_d$ is a blending function that makes the switching automatically. It is calculated as

$$\tilde{f}_d = \max(1 - f_{dt}, f_B) \tag{2.32}$$

where $f_{dt} = 1 - \tanh[(8r_{dt})^3]$. r_{dt} is the turbulent part of r_d used in the DDES formulation (see Equation (2.14b)). The empirical blending function, f_B, is obtained as

$$f_B = \min(2\exp\left(-9\alpha^2\right), 1), \quad \alpha = 0.25 - d_w/\Delta_{max}. \tag{2.33}$$

The empirical elevating function, f_e, prevents an excessive reduction of the modeled Reynolds stresses in the grey-area, and thereby solving the LLM problem. f_e is calculated as

$$f_e = \max((f_{e1} - 1), 0)\Psi f_{e2} \tag{2.34}$$

$$f_{e1} = \begin{cases} 2\exp(-11.09\alpha^2), & \alpha \geq 0 \\ 2\exp(-9\alpha^2), & \alpha < 0 \end{cases} \tag{2.35}$$

$$f_{e2} = 1 - \max(f_t, f_l), \quad f_t = \tanh[(c_t^2 r_{dt})^3], \quad f_l = \tanh[(c_l^2 r_{dl})^{10}] \tag{2.36}$$

where r_{dl} is the laminar part of r_d (see Equation (2.14b)). The constants, c_t and c_l, are 1.63 and 3.55, respectively. Ψ is the low-Reynols number correction term, the same as in Equation 2.15.

Lastly, the subgrid length scale of IDDES was determined to provide a variation along the wall-normal direction as in the eddy viscosity levels. Besides, it gives a reduction of the original subgrid length, thereby destabilizing the flow under potential instabilities. Δ_{IDDES} is calculated as follows,

$$\Delta_{\text{IDDES}} = \min\left(\max(C_w d_w, C_w \Delta_{max}, h_{wn}), \Delta_{max}\right) \tag{2.37}$$

where C_w is 0.15, and h_{wn} is a grid step in the wall-normal direction. It is suggested in the original paper [105] that in WMLES regions, one may use a stretching ratio of 1.14 with $y_1^+ < 1$ while generating a boundary layer mesh.

Incorporation of the Δ_{SLA} into IDDES One of the objective of this thesis is to simulate the cavity flow problems by the combination of the IDDES and the SLA approaches. For the implementation of the IDDES-SLA framework in METUDES, the steps in the paper of Guseva et al. [40] has been followed. Since $\tilde{f}_d$ is used in IDDES instead of f_d, the delaying function of DDES, the limitation to F_{KH} (see Equation 2.20) is changed as

$$F_{KH}^{lim} = \begin{cases} 1.0, & \tilde{f}_d > 0.01 \\ F_{KH}, & \tilde{f}_d \leq 0.01 \end{cases} \tag{2.38}$$

in a similar manner. The remaining computations to obtain Δ_{SLA} are the same. The subgrid length scale is, then, obtained as

$$\Delta_{\text{IDDES-SLA}} = \min\left(\max(C_w d_w, C_w \Delta_{max}, h_{wn}), \Delta_{\text{SLA}}\right) \tag{2.39}$$

which is used to find the ultimate length scale of IDDES-SLA by replacing Equation 2.31 with

$$l_{\text{IDDES-SLA}} = \tilde{f}_d(1 + f_e)d_w + (1 - \tilde{f}_d)C_{\text{DES}}\Delta_{\text{IDDES-SLA}}. \tag{2.40}$$

2.2.2 Numerics

2.2.2.1 Multiblock Topology

Computational domain of cavities is composed of two main regions: inside and outside of the cavity. It is difficult and inefficient to create a single block structured grid for the whole domain. Instead, two separate single grids can be generated, and connected to each other through an interface (see Figure 2.2a). Besides, some of the boundary layer transition simulations require a tunnel grid, where maintaining the grid orthogonality by a single grid from the airfoil surface to the wind tunnel walls is inconvenient. However, the previous version of METUDES works on a single block.

Hence, a multiblock topology option has been implemented. During the implementation into the code, data structure of the CFL3D solver, developed in NASA Langley Research Center [58], has been beneficial. A one-to-one blocking strategy is an easy as well as an efficient way for block interfaces. In this situation, the interface shared by multiple single blocks are identical such that all grid points located at the interface are coincided. The crucial point is the communication between the blocks, which are performed through ghost cells. These cells should be identical to the inner cells of the neighbor block. Figure 2.1 describes this communication. Here, the ghost cells of block 2 receive the flow variables directly from the inner cells of block 1. In METUDES, this send and receive routine is realized for three ghost cells to complete the central spatial discretization of the 4th-order DRP scheme. Note that METUDES conducts this multiblock communication after the physical boundary conditions are enforced.

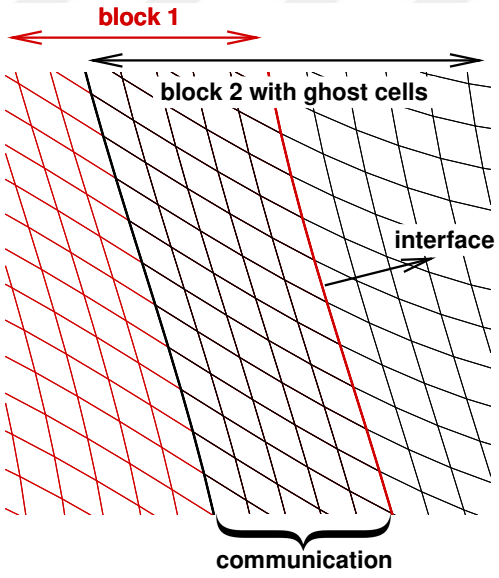
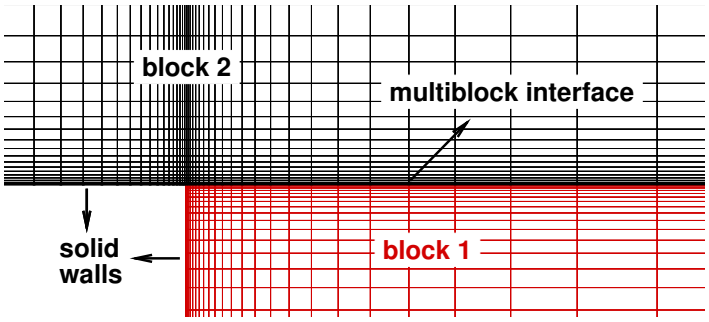


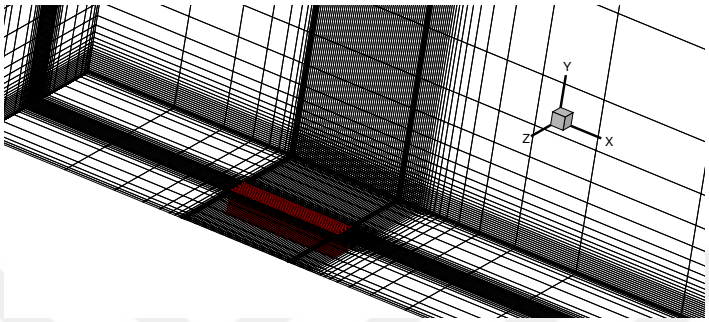
Figure 2.1: Multiblock communication between two blocks through ghost and inner cells

2.2.2.2 High-Order Overset Grid Technique

The one-to-one multiblock approach needs an identical communication region. This limits the mesh generation capability around complex geometries. One example is



(a) 2-D view



(b) 3-D view at IJK plane surfaces (showing one every three cells)

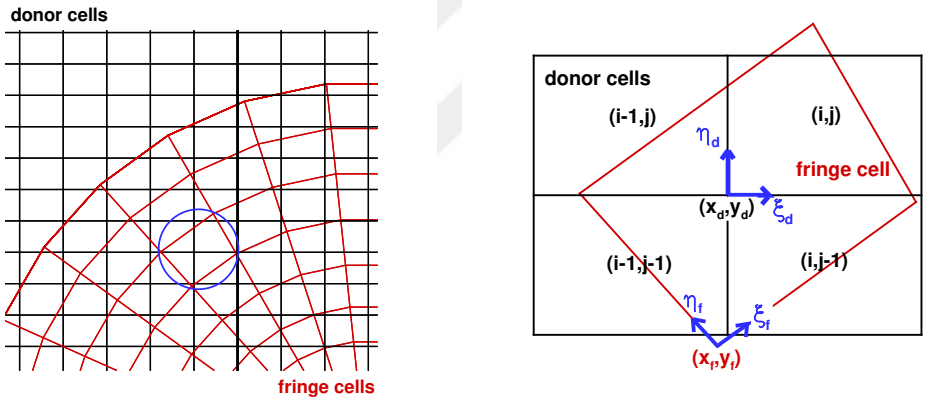
Figure 2.2: The multiblock structured mesh domain around an open cavity geometry with $L/D = 5$. Block 1 represents the inside of the cavity while Block 2 represents the outside of it.

the store separation simulations from cavities[2]. Even though a structured meshing around a store is achieved, merging of that with the cavity mesh is quite challenging. Moreover, one may aim to refine a certain region such as a wake zone following a blade section, which is crucial for transitional flows, while keeping the rest of the domain the same. On the contrary, one may want to coarsen a grid locally. For instance, in cavity domains very fine grid steps in boundary layers near the existing walls are extended to the far field boundaries of the outer block. This causes a redundant grid refinement, considering the walls locating along all directions (see Figure 2.2b). Such a local refinement or coarsening spoils the coincidence of cells at the multiblock interface. Therefore, the Chimera type overset grid technique, developed for complex and moving geometries [4], has been implemented into the code. This method handles the

[2] The store separation is out of the scope of this thesis; however, in the long term it might be simulated via METUDES.

communication between overlapped structured blocks by interpolation. Overlapping gives a freedom to connect two blocks having different grid topologies.

The key point, here, is the interpolation algorithm. A conventional linear interpolation is adequate for low-order solvers; however, it has shown that a high-order interpolation is required to preserve the high-order accuracy of solvers [17]. Lee *et al.* [67] introduced a high-order interpolation method for overset grid based on a finite volume scheme. This method basically finds the interpolation polynomial for overlapped grid cells in one grid (called donor grid), then transforms the coordinates, and finally obtains the desired cell value of the other grid (called fringe grid). The study also suggests to use a multidimensional limiting process to remove the oscillations appearing because of high-order interpolations. In the mentioned study, the results from Euler equations demonstrated that the 4th-order interpolation preserves the 6th-order accuracy of a solver without changing the flow solutions.



(a) overlapped region (b) fringe and donor cells

Figure 2.3: Overset interpolation between two blocks through fringe and donor cells

Three different interpolation methods based on finite volume schemes have been developed to be implemented in METUDES: 2-D 2nd-order, 2-D 3rd-order, and 3-D 3rd-order interpolations. Since METUDES is 4th-order accurate in space, the 3rd-order interpolations are intended to use for the overlapped regions including highly turbulent structures, thereby preserving the accuracy. In the Euler regions, the 2nd-order interpolation should be adequate. During the development, the same steps shown for

the 2-D 4th-order interpolation in [67] have been followed.

2-D 2nd-Order Interpolation In METUDES, the overlapped region involves ghost cells so that the interpolation is used to obtain flow variables attached to them. Suppose a uniform mesh block and an O-mesh block are connected as in Figure 2.3a. If the ghost cell values of the O-mesh are tried to obtain, the cells in red are called fringe cells. On the other hand, the Cartesian grid which interpolates its inner cell values and transfers the resulting value to the O-mesh is called donor grid; and consequently, the cells in black are the donor cells. As an example, the value of the fringe cell indicated by a blue circle (see Figure 2.3a) is calculated through the 2-D 2nd-order interpolation method. Firstly, the interpolation function is written in the donor grid coordinates (see Figure 2.3b) as follows,

$$\phi_d(\xi_d, \eta_d) = A\xi_d + B\eta_d + C\xi_d\eta_d + D. \tag{2.41}$$

Here, ϕ represents any flow variable whereas A, B, C, and D are the unknown coefficients. 4 cell values are required to solve for the unknowns; therefore, 4 donor cells closest to the fringe cell are selected as in Figure 2.3b. Each donor cell value is equal to the integrated value of the interpolation function. The integration boundaries are determined according to the coordinate origin. For instance, the value of ϕ at the cell with the indices $(i-1, j)$ is equal to

$$\overline{\phi}_{i-1,j} = \int_0^1 \left(\int_{-1}^0 \phi_d(\xi_d, \eta_d) d\xi_d \right) d\eta_d. \tag{2.42}$$

Remember that $\overline{\phi}_{i-1,j}$ is known from the donor cell. Using the other donor cells, the coefficients of the interpolation function are obtained as

$$\begin{bmatrix} A \\ B \\ C \\ D \end{bmatrix} = \begin{bmatrix} -1/2 & 1/2 & -1/2 & 1/2 \\ -1/2 & -1/2 & 1/2 & 1/2 \\ 1 & -1 & -1 & 1 \\ 1/4 & 1/4 & 1/4 & 1/4 \end{bmatrix} \begin{bmatrix} \overline{\phi}_{i-1,j-1} \\ \overline{\phi}_{i,j-1} \\ \overline{\phi}_{i-1,j} \\ \overline{\phi}_{i,j} \end{bmatrix}.$$

Next, the coordinates should be transformed; thus, the interpolation function for the fringe cell, ϕ_f, could be obtained. Here, ϕ_f is written in the fringe cell coordinates as

$$\phi_f(\xi_f, \eta_f) = A'\xi_f + B'\eta_f + C'\xi_f\eta_f + D' \tag{2.43}$$

where A', B', C', and D' are the new unknowns and can be computed by relating the coordinates. Using the chain rule,

$$\begin{aligned} x_f &= \frac{\partial x_f}{\partial \xi_f}\xi_f + \frac{\partial x_f}{\partial \eta_f}\eta_f, \quad y_f = \frac{\partial y_f}{\partial \xi_f}\xi_f + \frac{\partial y_f}{\partial \eta_f}\eta_f, \\ \xi_d &= \frac{\partial \xi_d}{\partial x_d}x_d + \frac{\partial \xi_d}{\partial y_d}y_d, \quad \eta_d = \frac{\partial \eta_d}{\partial x_d}x_d + \frac{\partial \eta_d}{\partial y_d}y_d, \end{aligned} \tag{2.44}$$

and the distance between the coordinate origins,

$$x_d = x_f + \Delta x, \quad y_d = y_f + \Delta y, \tag{2.45}$$

the relations between (ξ_d, η_d) and (ξ_f, η_f) can be found as

$$\xi_d = \alpha_1\xi_f + \beta_1\eta_f + \gamma_1, \quad \eta_d = \alpha_2\xi_f + \beta_2\eta_f + \gamma_2 \tag{2.46}$$

where

$$\begin{aligned} \alpha_1 &= \frac{\partial \xi_d}{\partial x_d}\frac{\partial x_f}{\partial \xi_f} + \frac{\partial \xi_d}{\partial y_d}\frac{\partial y_f}{\partial \xi_f}, \quad \beta_1 = \frac{\partial \xi_d}{\partial x_d}\frac{\partial x_f}{\partial \eta_f} + \frac{\partial \xi_d}{\partial y_d}\frac{\partial y_f}{\partial \eta_f}, \quad \gamma_1 = \frac{\partial \xi_d}{\partial x_d}\Delta x + \frac{\partial \xi_d}{\partial y_d}\Delta y, \\ \alpha_2 &= \frac{\partial \eta_d}{\partial x_d}\frac{\partial x_f}{\partial \xi_f} + \frac{\partial \eta_d}{\partial y_d}\frac{\partial y_f}{\partial \xi_f}, \quad \beta_2 = \frac{\partial \eta_d}{\partial x_d}\frac{\partial x_f}{\partial \eta_f} + \frac{\partial \eta_d}{\partial y_d}\frac{\partial y_f}{\partial \eta_f}, \quad \gamma_2 = \frac{\partial \eta_d}{\partial x_d}\Delta x + \frac{\partial \eta_d}{\partial y_d}\Delta y. \end{aligned} \tag{2.47}$$

The fractional terms are obtained from the metric tensor. Then, substituting Equation 2.46 into Equation 2.41 and equating the result to Equation 2.43, the coefficients of ϕ_f are obtained as

$$\begin{bmatrix} A' \\ B' \\ C' \\ D' \end{bmatrix} = \begin{bmatrix} \alpha_1 & \alpha_2 & \alpha_1\gamma_2 + \alpha_2\gamma_1 & 0 \\ \beta_1 & \beta_2 & \beta_1\gamma_2 + \beta_2\gamma_1 & 0 \\ 0 & 0 & \alpha_1\beta_2 + \beta_1\alpha_2 & 0 \\ \gamma_1 & \gamma_2 & \gamma_1\gamma_2 & 1 \end{bmatrix} \begin{bmatrix} A \\ B \\ C \\ D \end{bmatrix}.$$

Finally, the flow variable at the fringe cell is calculated by integrating $\phi_f(\xi_f, \eta_f)$ function. This is repeated for each fringe cell at each numerical iteration. Since fixed meshes are used in this thesis, searching for the donor cells, and computing the most of the parameters including metrics and constants are conducted once at the beginning of the simulations. This reduces the computational cost of the overset grid, substantially. As a final remark, the donor cells are found simply by searching for the cell centers in the donor grid closest to the fringe cell center.

2-D 3rd-Order Interpolation For the 2-D 3rd-order method, the interpolation function of the fringe grid is

$$\phi_f(\xi_f, \eta_f) = A'\xi_f^2 + B'\eta_f^2 + C'\xi_f\eta_f + D'\xi_f + E'\eta_f + F'. \tag{2.48}$$

Now, 6 donor cells are needed. Let the closest donor cell to the fringe cell have indices (i, j). After the previous procedure is followed, the ultimate relation between the donor flow variables and the coefficients are found as

$$K = L * M * N \tag{2.49}$$

where

$$K = \begin{bmatrix} A' \\ B' \\ C' \\ D' \\ E' \\ F' \end{bmatrix}, L = \begin{bmatrix} \alpha_1^2 & \alpha_2^2 & \alpha_1\alpha_2 & 0 & 0 & 0 \\ \beta_1^2 & \beta_2^2 & \beta_1\beta_2 & 0 & 0 & 0 \\ 2\alpha_1\beta_1 & 2\alpha_2\beta_2 & \alpha_1\beta_2 + \alpha_2\beta_1 & 0 & 0 & 0 \\ 2\alpha_1\gamma_1 & 2\alpha_2\gamma_2 & \alpha_1\gamma_2 + \alpha_2\gamma_1 & \alpha_1 & \alpha_2 & 0 \\ 2\beta_1\gamma_1 & 2\beta_2\gamma_2 & \beta_1\gamma_2 + \beta_2\gamma_1 & \beta_1 & \beta_2 & 0 \\ \gamma_1^2 & \gamma_2^2 & \gamma_1\gamma_2 & \gamma_1 & \gamma_2 & 1 \end{bmatrix},$$

$$M = \begin{bmatrix} 0 & 0 & 1/2 & -1 & 1/2 & 0 \\ 0 & 1/2 & 0 & -1 & 0 & 1/2 \\ 1 & -1 & -1 & 1 & 0 & 0 \\ -1/2 & 1/2 & -1/2 & 1/2 & 0 & 0 \\ -1/2 & -1/2 & 1/2 & 1/2 & 0 & 0 \\ 1/4 & 1/12 & 1/12 & 11/12 & -1/6 & -1/6 \end{bmatrix}, N = \begin{bmatrix} \overline{\phi}_{i-1,j-1} \\ \overline{\phi}_{i,j-1} \\ \overline{\phi}_{i-1,j} \\ \overline{\phi}_{i,j} \\ \overline{\phi}_{i+1,j} \\ \overline{\phi}_{i,j+1} \end{bmatrix}$$

α, β, and γ variables are the same as in Equation 2.47.

3-D 3$^{\mathbf{rd}}$-Order Interpolation The 3-D 3rd-order interpolation function requires 10 coefficients, and written as

$$\phi_f(\xi_f, \eta_f, \zeta_f) = A'\xi_f^2 + B'\eta_f^2 + C'\zeta_f^2 + D'\xi_f\eta_f + E'\xi_f\zeta_f + F'\eta_f\zeta_f + G'\xi_f + H'\eta_f + I'\zeta_f + J' \tag{2.50}$$

Again, if the closest donor cell have indices (i, j, k), following the same steps yields the coefficients as

$$K = L * M * N \tag{2.51}$$

where

$$K = \begin{bmatrix} A' \\ B' \\ C' \\ D' \\ E' \\ F' \\ G' \\ H' \\ I' \\ J' \end{bmatrix}, L = \begin{bmatrix} \alpha_1^2 & \alpha_2^2 & \alpha_3^2 & \alpha_1\alpha_2 & \alpha_1\alpha_3 & \alpha_2\alpha_3 & 0 & 0 & 0 & 0 \\ \beta_1^2 & \beta_2^2 & \beta_3^2 & \beta_1\beta_2 & \beta_1\beta_3 & \beta_2\beta_3 & 0 & 0 & 0 & 0 \\ \theta_1^2 & \theta_2^2 & \theta_3^2 & \theta_1\theta_2 & \theta_1\theta_3 & \theta_2\theta_3 & 0 & 0 & 0 & 0 \\ 2\alpha_1\beta_1 & 2\alpha_2\beta_2 & 2\alpha_3\beta_3 & \alpha_1\beta_2 + \alpha_2\beta_1 & \alpha_1\beta_3 + \alpha_3\beta_1 & \alpha_2\beta_3 + \alpha_3\beta_2 & 0 & 0 & 0 & 0 \\ 2\alpha_1\theta_1 & 2\alpha_2\theta_2 & 2\alpha_3\theta_3 & \alpha_1\theta_2 + \alpha_2\theta_1 & \alpha_1\theta_3 + \alpha_3\theta_1 & \alpha_2\theta_3 + \alpha_3\theta_2 & 0 & 0 & 0 & 0 \\ 2\beta_1\theta_1 & 2\beta_2\theta_2 & 2\beta_3\theta_3 & \beta_1\theta_2 + \beta_2\theta_1 & \beta_1\theta_3 + \beta_3\theta_1 & \beta_2\theta_3 + \beta_3\theta_2 & 0 & 0 & 0 & 0 \\ 2\alpha_1\gamma_1 & 2\alpha_2\gamma_2 & 2\alpha_3\gamma_3 & \alpha_1\gamma_2 + \alpha_2\gamma_1 & \alpha_1\gamma_3 + \alpha_3\gamma_1 & \alpha_2\gamma_3 + \alpha_3\gamma_2 & \alpha_1 & \alpha_2 & \alpha_3 & 0 \\ 2\beta_1\gamma_1 & 2\beta_2\gamma_2 & 2\beta_3\gamma_3 & \beta_1\gamma_2 + \beta_2\gamma_1 & \beta_1\gamma_3 + \beta_3\gamma_1 & \beta_2\gamma_3 + \beta_3\gamma_2 & \beta_1 & \beta_2 & \beta_3 & 0 \\ 2\gamma_1\theta_1 & 2\gamma_2\theta_2 & 2\gamma_3\theta_3 & \gamma_1\theta_2 + \gamma_2\theta_1 & \gamma_1\theta_3 + \gamma_3\theta_1 & \gamma_2\theta_3 + \gamma_3\theta_2 & \theta_1 & \theta_2 & \theta_3 & 0 \\ \gamma_1^2 & \gamma_2^2 & \gamma_3^2 & \gamma_1\gamma_2 & \gamma_1\gamma_3 & \gamma_2\gamma_3 & \gamma_1 & \gamma_2 & \gamma_3 & 1 \end{bmatrix},$$

$$M = \begin{bmatrix} -1 & 1/2 & 0 & 1/2 & 0 & 0 & 0 & 0 & 0 & 0 \\ -1 & 0 & 1/2 & 0 & 1/2 & 0 & 0 & 0 & 0 & 0 \\ -1 & 0 & 0 & 0 & 0 & 1/2 & 1/2 & 0 & 0 & 0 \\ 1 & -1 & -1 & 0 & 0 & 0 & 0 & 1 & 0 & 0 \\ 1 & -1 & 0 & 0 & 0 & -1 & 0 & 0 & 0 & 1 \\ 1 & 0 & -1 & 0 & 0 & -1 & 0 & 0 & 1 & 0 \\ 0 & 0 & 1/2 & 0 & 0 & 1/2 & 0 & -1/2 & 0 & -1/2 \\ 0 & 1/2 & 0 & 0 & 0 & 1/2 & 0 & -1/2 & -1/2 & 0 \\ 0 & 1/2 & 1/2 & 0 & 0 & 0 & 0 & 0 & -1/2 & -1/2 \\ 5/4 & -1/6 & -1/6 & -1/6 & -1/6 & -1/6 & -1/6 & 1/4 & 1/4 & 1/4 \end{bmatrix}, N = \begin{bmatrix} \overline{\phi}_{i,j,k} \\ \overline{\phi}_{i-1,j,k} \\ \overline{\phi}_{i,j-1,k} \\ \overline{\phi}_{i+1,j,k} \\ \overline{\phi}_{i,j+1,k} \\ \overline{\phi}_{i,j,k-1} \\ \overline{\phi}_{i,j,k+1} \\ \overline{\phi}_{i-1,j-1,k} \\ \overline{\phi}_{i,j-1,k-1} \\ \overline{\phi}_{i-1,j,k-1} \end{bmatrix}.$$

This time α, β, γ, and the new θ variables include the third dimension metrics, additionally. The ones with the subscript 1 are as follows,

$$\begin{aligned} \alpha_1 &= \frac{\partial \xi_d}{\partial x_d}\frac{\partial x_f}{\partial \xi_f} + \frac{\partial \xi_d}{\partial y_d}\frac{\partial y_f}{\partial \xi_f} + \frac{\partial \xi_d}{\partial z_d}\frac{\partial z_f}{\partial \xi_f}, \\ \beta_1 &= \frac{\partial \xi_d}{\partial x_d}\frac{\partial x_f}{\partial \eta_f} + \frac{\partial \xi_d}{\partial y_d}\frac{\partial y_f}{\partial \eta_f} + \frac{\partial \xi_d}{\partial z_d}\frac{\partial z_f}{\partial \eta_f}, \\ \theta_1 &= \frac{\partial \xi_d}{\partial x_d}\frac{\partial x_f}{\partial \zeta_f} + \frac{\partial \xi_d}{\partial y_d}\frac{\partial y_f}{\partial \zeta_f} + \frac{\partial \xi_d}{\partial z_d}\frac{\partial z_f}{\partial \zeta_f}, \\ \gamma_1 &= \frac{\partial \xi_d}{\partial x_d}\Delta x + \frac{\partial \xi_d}{\partial y_d}\Delta y + \frac{\partial \xi_d}{\partial z_d}\Delta z. \end{aligned} \tag{2.52}$$

2.2.2.3 Optimizing the Numerical Algorithms

The METUDES solver had been tested mostly for flow simulations over airfoil profiles and flat plates until this thesis study. When cavity flow problems were simulated, three numerical difficulties were encountered:

1. The subiteration number in dual time stepping substantially increased. In other words, late convergence of residual values was observed, which slowed down the running performance of the code.

2. The code could be suddenly aborted even after the transition period had passed. This abortion was caused by negative $\hat{\nu_t}$ values emerged in the outer domain along the intersection of two orthogonal cavity walls.

3. A deformity was observed along the shear layer revealed at the cavity mouth. As time step of an unsteady simulation was advanced, turbulent viscosity contours started to deform around the grid cells having very high aspect ratios ($AR \sim \mathcal{O}(4)$) and located along the cavity mouth. This deformation is shown in Figure 2.4. Here, a discontinuity exists in the normal direction, which is also seen in the pressure contours at later time steps, as indicated in the same figure. This nonphysical situation inevitably caused a misprediction in the results. Interestingly, no discontinuity was observed when the flow was simulated as laminar everywhere. However, slow convergence problem was still the issue.

In summary, the mentioned problems were preventing to obtain successful cavity flow simulations quite a while in the early stages of this study. The following improvements implemented in the solver algorithms resolved all the problems.

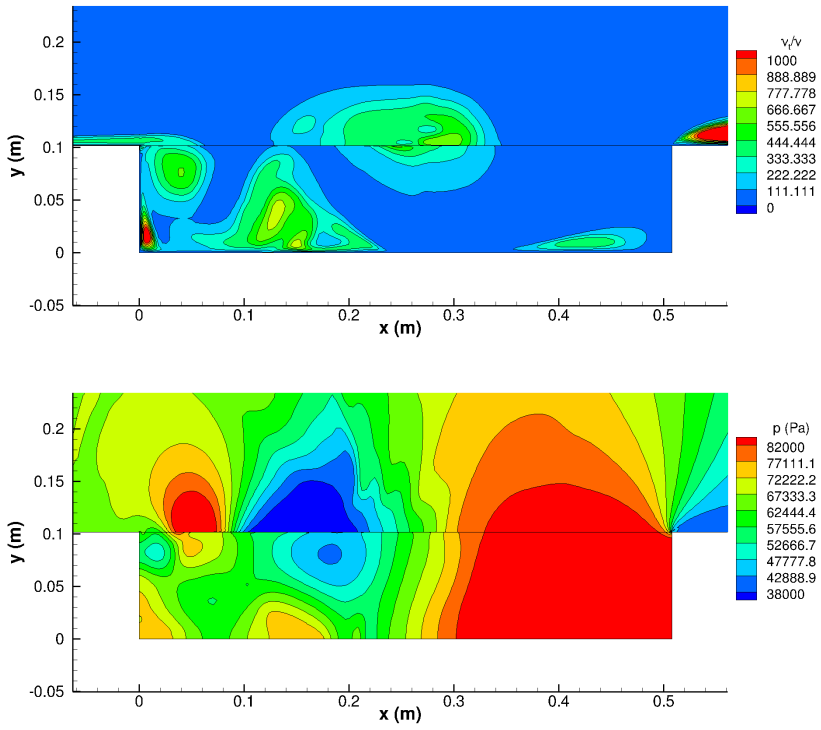


Figure 2.4: Cavity flow field deformations happening during initial cavity flow simulations. Above: eddy viscosity related contours, below: pressure contours

Change in the Residual Smoothing Algorithm In METUDES, residual obtained after spatial discretization is smoothed out to increase the CFL number within the subiterations, as discussed in Section 2.1.4. This smoothing operations (by the Laplace operator) are only performed for the N-S equations. In order to reduce the computational cost, the Laplace operator is applied in each direction separately. For instance, in i^{th}-direction the following equation is to be solved:

$$-\epsilon_i \bar{R}_{i-1,j,k} + (1+2\epsilon_i)\bar{R}_{i,j,k} - \epsilon_i \bar{R}_{i+1,j,k} = R_{i,j,k} \tag{2.53}$$

where $\bar{R}$ is the smoothed residual (R), and ϵ is the coefficient containing spectral radius and some constants. Including the neighboring cells results in a tridiagonal system, which is solved implicitly by the Thomas algorithm. If one writes Equation 2.53 for a boundary cell index (say $i = 1$),

$$-\epsilon_1 \bar{R}_{0,j,k} + (1+2\epsilon_1)\bar{R}_{1,j,k} - \epsilon_1 \bar{R}_{2,j,k} = R_{1,j,k} \tag{2.54}$$

is obtained. Here, $\bar{R}_{0,j,k}$ needs to take the values of a boundary condition (BC). Previously, it was assumed as $\bar{R}_{0,j,k} = 0$ (Dirichlet type BC). By applying the same BC for the other ghost cell ($\bar{R}_{imax+1,j,k} = 0$), the following matrix system is obtained:

$$\begin{bmatrix} 1+2\epsilon_i & -\epsilon_i & 0 & 0 & \cdots & 0 \\ -\epsilon_i & 1+2\epsilon_i & -\epsilon_i & 0 & \cdots & 0 \\ 0 & \ddots & \ddots & \ddots & & \\ \vdots & & \ddots & \ddots & \ddots & \\ \vdots & & & -\epsilon_i & 1+2\epsilon_i & -\epsilon_i \\ 0 & \cdots & \cdots & \cdots & -\epsilon_i & 1+2\epsilon_i \end{bmatrix} \cdot \begin{bmatrix} \bar{R}_{1,j,k} \\ \bar{R}_{2,j,k} \\ \vdots \\ \vdots \\ \bar{R}_{imax-1,j,k} \\ \bar{R}_{imax,j,k} \end{bmatrix} = \begin{bmatrix} R_{1,j,k} \\ R_{2,j,k} \\ \vdots \\ \vdots \\ R_{imax-1,j,k} \\ R_{imax,j,k} \end{bmatrix}. \tag{2.55}$$

Suppose that all smoothed residual values are equal to each other. In this situation, $\bar{R}_{i,j,k}$ becomes the same as $R_{i,j,k}$ except those of the boundary cells where, as an example, $(1+\epsilon_1)\bar{R}_{1,j,k} = \bar{R}_{1,j,k}$. This suggests that the mentioned Dirichlet BC may cause some numerical instabilities. Instead, a Neumann type BC is used in this study,

that is, the gradient is taken as zero: $\bar{R}_{0,j,k} = \bar{R}_{1,j,k}$ and $\bar{R}_{imax-1,j,k} = \bar{R}_{imax,j,k}$. Consequently, the new system of equations becomes as

$$\begin{bmatrix} 1+\epsilon_i & -\epsilon_i & 0 & 0 & \cdots & 0 \\ -\epsilon_i & 1+2\epsilon_i & -\epsilon_i & 0 & \cdots & 0 \\ 0 & \ddots & \ddots & \ddots & & \\ \vdots & & \ddots & \ddots & \ddots & \\ \vdots & & & -\epsilon_i & 1+2\epsilon_i & -\epsilon_i \\ 0 & \cdots & \cdots & \cdots & -\epsilon_i & 1+\epsilon_i \end{bmatrix} \cdot \begin{bmatrix} \bar{R}_{1,j,k} \\ \bar{R}_{2,j,k} \\ \vdots \\ \vdots \\ \bar{R}_{imax-1,j,k} \\ \bar{R}_{imax,j,k} \end{bmatrix} = \begin{bmatrix} R_{1,j,k} \\ R_{2,j,k} \\ \vdots \\ \vdots \\ R_{imax-1,j,k} \\ R_{imax,j,k} \end{bmatrix}. \tag{2.56}$$

When this new form was used in cavity simulations, the breakdown issue of the code was resolved. As a matter of fact, it increased the convergence speed as well. In addition, it was decided that a residual smoothing operator should be applied to not only the N-S equations but also the S-A equation. This provided a quick drop of the corresponding eddy viscosity residual. Note that for the turbulence equation, the same system of equations is used. However, ϵ is taken as constant, which is 0.75 to double the CFL number.

Shock Sensor in the N-S Equations using TVD Approach Sharp gradients of flow quantities occurring mostly in shear layers and/or at high Mach number conditions (such as shock waves) may cause numerical oscillations which result in poor results during the computations. METUDES involves a pressure-based shock sensor in the blended matrix dissipation calculations to prevent this problem. The sensor, ν, is obtained in the ith-direction as

$$\nu_i = \left| \frac{p_{i+1,j,k} - 2p_{i,j,k} + p_{i-1,j,k}}{p_{i+1,j,k} + 2p_{i,j,k} + p_{i-1,j,k}} \right| \tag{2.57}$$

where p is the pressure variable. ν behaves as a switch which enforces 2nd-order dissipation terms in case of sharp gradients. In cavity flow, these oscillations become stronger than the ones in the airfoil problems. One explanation is the possible shock waves on the shear layer instabilities. In [116], it was suggested the use of a TVD

(Total Variation Diminishing) switch instead of Equation 2.57 to overcome strong oscillations. A mix of a TVD switch and the current formulation is coded by following [116] as

$$\begin{aligned} \nu_i &= \frac{|p_{i+1,j,k} - 2p_{i,j,k} + p_{i-1,j,k}|}{\omega P + (1-\omega) P_{TVD}}, \\ P &= p_{i+1,j,k} + 2p_{i,j,k} + p_{i-1,j,k}, \\ P_{TVD} &= |p_{i+1,j,k} - p_{i,j,k}| + |p_{i,j,k} - p_{i-1,j,k}|. \end{aligned} \tag{2.58}$$

The ω parameter determines the weight of the TVD switch. When $\omega = 1$, Equation 2.57 is recovered. After making several cavity flow simulations, ω is calibrated as 0.6. When only the TVD approach improvement was applied, the breakdown issue was resolved but the convergence got worse. Conversely, the convergence was accelerated more when TVD and new residual smoothing algorithm were used together. Moreover, the discontinuity appearing in the flow contours was reduced by the TVD switch.

Biased Artificial Dissipation near the Solid Walls METUDES conducts central discretization in space for accurate resolution of flow with minimum dissipation. Artificial dissipation is used to eliminate the spurious waves induced by the central scheme throughout the computational domain. However, an excessive addition of artificial dissipation may change the effective Reynolds number near walls [117]. Since the cavity domain has solid walls in all directions, this issue should be considered carefully. In order to increase stability and convergence, artificial dissipation is decided to be computed with biased grid cells at wall boundaries as proposed in [117]. Suppose that a 4th-order artificial dissipation is added to a 2nd-order spatial differencing of a variable, W, at the wall grid cell (cell index = 1) in j^{th}-direction (normalwise). The artificial dissipation is calculated as follows,

$$D_j^4 W_1 = (\lambda\epsilon)_2(W_3 - 2W_2 + W_1) - 2(\lambda\epsilon)_1(W_2 - 2W_1 + W_0) + (\lambda\epsilon)_0(W_1 - 2W_0 + W_{-1}) \tag{2.59}$$

where D represents the artificial dissipation, λ is the spectral radii, and ϵ is the coefficient containing the pressure sensor. Figure 2.5 describes the cells used in this discretization. Here, grid cells with indices 0 and -1 indicate the ghost cells, located outside the domain.

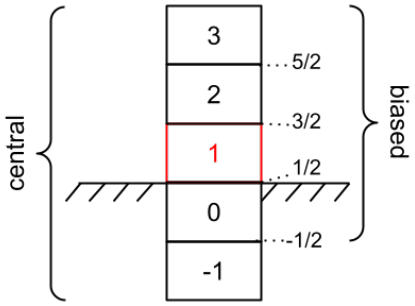


Figure 2.5: Cells used for the 4th-order artificial dissipation in j^{th}-direction at the wall cell (j=1)

If a forward differencing of the variable between ghost cells ($\Delta W_{-1/2} = W_0 - W_{-1}$) is equated as

$$\Delta W_{-1/2} = 2\Delta W_{1/2} - \Delta W_{3/2}, \tag{2.60}$$

then, W_{-1} is replaced by $3W_0 - 3W_1 + W_2$ such that Equation 2.59 takes a noncentral (biased) form as follows,

$$D_j^4 W_1 = (\lambda\epsilon)_2(W_3 - 2W_2 + W_1) - 2(\lambda\epsilon)_1(W_2 - 2W_1 + W_0) + (\lambda\epsilon)_0(W_2 - 2W_1 + W_0). \tag{2.61}$$

This form of dissipation near walls ensures that the viscous sublayer formed in turbulent flows is conserved while the numerical stability and convergence are enhanced [117]. In the test studies, convergence acceleration was observed.

Directional Scaling Factor in the Artificial Dissipation of the Turbulence Model

The high AR grids cause over dissipation, and thereby affecting the numerical convergence and accuracy [116]. On high AR grids, especially when $AR > 50$, use

of an isotropic scaling factor in the artificial dissipation leads to excessive numerical dissipation [84]. In METUDES, this numerical difficulty is suppressed by use of a directional scaling factor, instead. This is applied only for the N-S equations, which is commonly preferred in literature. In the previous airfoil problems, the high AR grids were present near the solid walls; therefore, the S-A equation was not the problem as the eddy viscosity was already hampered by the viscous sublayer. In cavity flow problems, however, the high AR grids are present away from the wall, and as mentioned before, this causes discontinuities along the shear layer. Consequently, it was decided to scale the artificial dissipation of the S-A equation as well. Literature has a little information about this issue. In [55], it is suggested to add the directional scaling only to the fourth-order diffusion. In the light of this information, two scaling factors are computed:

$$\begin{aligned} \lambda_i &= \max\left(|\vec{u}\cdot\vec{A}_i|, 0.01(|\vec{u}\cdot\vec{A}_i| + c||\vec{A}_i||)\right), \\ \lambda_{i,AR} &= \lambda_i\left(1 + r_1^{\zeta} + r_2^{\zeta}\right). \end{aligned} \tag{2.62}$$

Here, λ_i is the spectral radius used for the second-order dissipation term as an isotropic scaling factor whereas $\lambda_{i,AR}$ is the directional one and added to the fourth-order dissipation. In λ_i computation, $\vec{u}$ is the local velocity, $\vec{A}_i$ is the cell-face area vector in i^{th}-direction, and c is the speed of sound. On the other hand, $r_1 = \lambda_j/\lambda_i$, $r_2 = \lambda_k/\lambda_i$, and $\zeta = 0.66$. Here, use of $\lambda_{i,AR}$ is expected to remove the effect of grid spacing discrepancies of high AR cells. This algorithm has resolved the discontinuity problem upto cell AR of $\mathcal{O}(4)$. Thus, the cavity meshing along the shear layer for the rest of the study is generated, accordingly.

After implementing the above improvements in the solver, the same simulation is repeated. The new flow contours are shown in Figure 2.6. This instantaneous flow field represents much further time step than the previous one in Figure 2.4. It shows that the deformation problem is disappeared completely. Additionally, the new and old convergence speeds are compared in Figure 2.7 where the residual drop in x-momentum values is drawn. The interval between two sequential peaks represents the subiteration number required for one physical time step. The results show that the running performance of the solver is clearly accelerated.

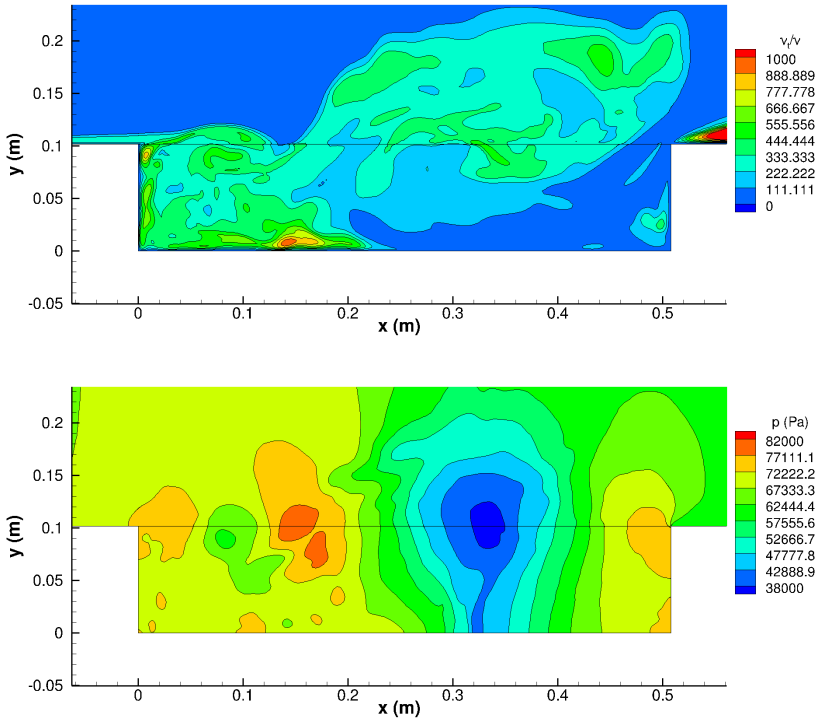


Figure 2.6: Flow field by DDES after numerical improvements. Above: eddy viscosity related contours, below: pressure contours

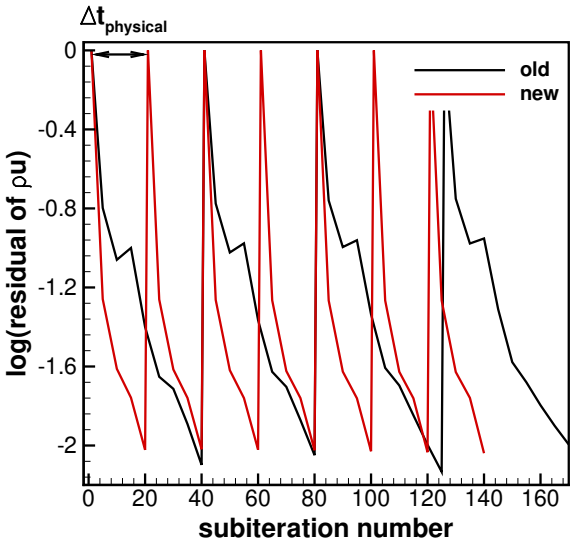


Figure 2.7: Comparison of the convergence speeds of the residual drop in x-momentum

CHAPTER 3

SIMULATION SETUPS

This chapter discusses how simulation configurations are set up. Specifically, grid generation strategy, setting of boundary & initial conditions, and selection of time step are presented. Unless otherwise stated, the simulations carried out in the next chapters are configured as described below:

3.1 Grid Generation

DES meshing strategies of [111] are partially followed during grid creation. A typical DES grid is composed of RANS, LES, and Euler zones. The RANS zone is a region where all eddy structures are modeled. It starts from a solid wall, and usually ends around the corresponding boundary layer edge. Subsequently, the LES zone, where the most of the eddies are resolved, extends from the end of the RANS zone to the beginning of the Euler one. The rest is covered by the Euler zone in which the eddy and vortical structures no longer exist.

DDES shields an attached boundary layer as a RANS zone. By DDES, the grey-area is located away from the boundary layer edge. However, when the DDES-SLA framework is used (as in almost all flow problems in this thesis), it is possible that the grey-area penetrates inside the outer layer of the boundary layer. This means the RANS zone may end at the beginning of the outer layer. Therefore, all the computational grids are created according to this scenario, which differs from the suggestions in [111].

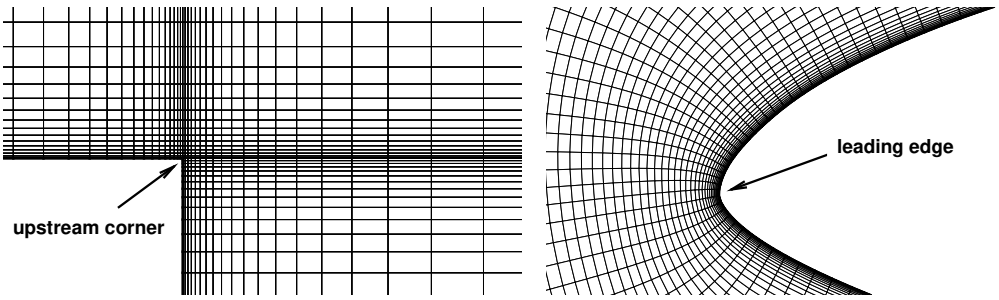
In the wall normal direction, the first cell height is determined by taking the nondi-

mensional wall normal distance, y^+, as approximately 1. Then, the subsequent grid nodes are created with a stretching ratio (SR) of 1.2, which is typical in RANS grids. SR is reduced to 1.05 when the outer layer (and possible LES zone) starts, which is expected at a distance of $\delta/3$ (δ: boundary layer thickness). This SR value is maintained up to the maximum cell dimension, Δ_{max}, corresponding to the minimum resolved eddy size. After that, no further stretching is applied until the LES zone ends. In the Euler zone, SR is gradually increased to 1.2, thereby extruding the grid rapidly. This provides some mesh damping eventually for non-reflective boundary conditions.

A grid spacing in the spanwise direction, Δ_z, is directly dependent on Δ_{max}. In most cases the domain in the spanwise (lateral) direction is terminated by the periodic boundary condition such that Δ_z becomes uniform. Because cubic (isotropic) cells are preferred in the LES zone, which includes the eddies that are less dependent on the geometric boundary, Δ_z is to be the same as Δ_{max}. In addition, the span length should be sufficiently long to cover the largest vortical structure in the domain.

In the problems including straight solid walls such as flatplate, backward-facing step, and cavity flow, the streamwise grid spacing, Δ_x, grows with an SR of 1.2. If there exists a corner due to the intersection with another perpendicular solid wall, the grid is clustered towards the corner by following the boundary layer grid strategy, as shown in Figure 3.1a. In blade section problems, grid nodes along the surface are distributed according to the slope of the surface. As the slope increases, the mesh spacing gets finer (see Figure 3.1b). Again, the cubic cells are provided by setting the maximum of Δ_x as Δ_{max} in the LES zone.

As a result, the selection of both Δ_{max} and the span length is vital while creating a DES mesh. In turbulence aspect, since Δ_{max} exists inside the LES zone, mesh spacing criterion of LES studies can be used as a guide. In [36], it was suggested that Δ_z^+ (Δ_z in wall units) should be less than 40. This is given for low-order (mostly 2nd-order) spatial algorithms. Because METUDES is of high-order, the above limit can be relaxed. In aeroacoustic aspect, which is the most determining factor, Δ_{max} should be set such that high frequency sound waves are resolved. Suppose that the highest frequency wave to be resolved has a frequency of f_{max}. Then, Δ_{max} is determined



(a) Cavity mesh (b) Airfoil mesh

Figure 3.1: Close views of grids showing the grid nodes clustered around a) the upstream corner of a cavity, b) the leading edge of the NRELS826 airfoil profile

approximately as

$$\Delta_{max} \leq \frac{c}{A f_{max}} \tag{3.1}$$

where A is the minimum required number of mesh spacings to resolve a wave, and c is the sound speed. A depends on the spatial accuracy of a solver. For instance, the standard 2nd-order, 4th-order, and 6th-order algorithms require 15.7, 9.0, and 6.3 mesh spacings, respectively (when convective effects are ignored) whereas the 4th-order DRP scheme requires only 4.5 mesh spacings to resolve the same wave [126]. To be more conservative, A is taken as 5 in the present simulations. On the other hand, there is no certain formula for the span length. As Reynolds number and the thickness of the geometry increase, the span length should be increased as well. In brief, the selection of mentioned grid criteria is not straightforward. The best way is to perform a grid dependency study by changing Δ_{max} and the span length, separately. Most of the flow problems in this dissertation starts with this kind of grid dependency study.

3.2 Boundary Conditions

The computational domains are composed of single/multiple structured blocks. The boundary conditions (BCs) are set for all faces of each block. At solid boundaries, no-slip conditions are applied. The freestream values at inlet and/or far field bound-

aries are specified by the Riemann invariants. For infinite spans, the faces at the spanwise direction are connected to each other by periodic conditions. In case of a tunnel grid, tunnel walls are treated as inviscid (slip) wall with symmetry conditions. In simulations having an initial flatplate wall, a fraction of the wall following the flow entrance from the inlet boundary employs the slip wall BC. At subsonic outlet boundaries, pressure is specified as a freestream value whereas the rest of the variables are computed by linear extrapolations (i.e. back pressure BC). At supersonic outlet boundaries, all variables including pressure are extrapolated from the inner cells. The multiblock interfaces are communicated by either a one-to-one blocking strategy or a high-order overset interpolation. When an O-mesh is created around an airfoil, the interface between two end-to-end faces are seamed (i.e. seam BC).

Boundary conditions applied on all boundary faces (see Figure 3.2) of each computational domain demonstrated in Chapters 4 and 5 are listed in Table 3.1. The grid configurations are shown in the corresponding sections.

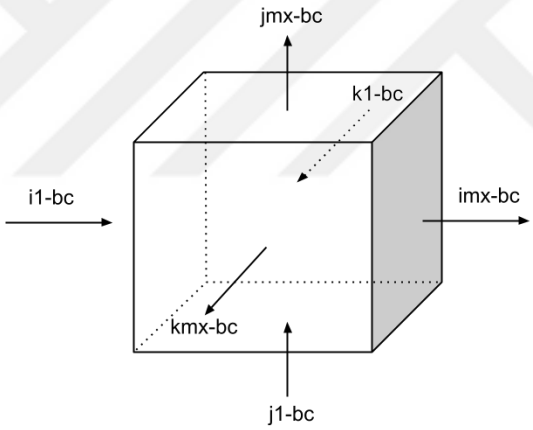


Figure 3.2: Boundary faces of a single computational block

3.3 Initial Conditions

All calculations are started by URANS by assigning freestream values everywhere. The initial value of the turbulence-related variable is set as $\hat{\nu}_{t\infty}/\nu = 10^{-8}$ thanks to the modified version of S-A equation [22]. If the BCM transition model is activated, the initial value is changed as $\hat{\nu}_{t\infty}/\nu = 0.015$ (Otherwise, the transition could not be

Table 3.1: Boundary conditions applied on each computational domain faces for all problems

Problems	i1-bc	imx-bc	j1-bc	jmx-bc	k1-bc	kmx-bc
Flatplate	Riemann	back pressure	slip/no-slip	back pressure	periodic	periodic
Eppler E387	seam	seam	no-slip	Riemann	periodic	periodic
Backward-facing step (1st block)	Riemann	one-to-one	slip/no-slip	slip/no-slip	periodic	periodic
Backward-facing step (2nd block)	no-slip/one-to-one	back pressure	no-slip	no-slip	periodic	periodic
Isentropic vortex	periodic	periodic	periodic	periodic	periodic	periodic
NRELS826 [a]	Riemann	back pressure	slip	slip	periodic	periodic
Circular cylinder	seam	seam	no-slip	Riemann	periodic	periodic
Cavity flow (1st block)	no-slip	no-slip	no-slip	one-to-one	periodic or slip or no-slip	periodic or slip or no-slip
Cavity flow (2nd block)	Riemann	back pressure	no-slip/slip/one-to-one	back pressure	periodic	periodic

[a] Tunnel grid. Indeed, there are 5 blocks inside, communicated by one-to-one strategy.

triggered). After initial transients leave the computational domain, and the mean flow fields reach statistical stationary state, simulations are continued with the selected DDES approach.

3.4 Time Step Selection

METUDES conducts a 2nd-order accurate time integration despite its high-order spatial scheme. This indicates that time step, Δt, should be chosen very carefully; otherwise, the truncation error due to a large time step might annihilate the gains from the spatial scheme. On the other hand, a very small time step increases the computational cost of unsteady simulations.

In wall-resolved LES studies, nondimensional time scale, Δt^+, was suggested to be in the order of 1 where $\Delta t^+ = u_\tau^2 \Delta t/\nu$, and u_τ is the friction velocity [36]. Since near the wall region is modeled, this criterion is too conservative for DES. In DES studies, time step can be computed as $\Delta t = \Delta_{max}/U_{max}$ where U_{max} represents the maximum flow velocity in the LES zone, and can be assumed roughly as $U_{max} = 1.5U_\infty$ [111]. This time step corresponds to the CFL number of 1. The dual time stepping approach of METUDES allows to take the CFL number as 100 approximately. Therefore, time step can be estimated according to this criterion.

In aeroacoustic simulations, there is an additional criterion that depends on both the grid resolution (or the maximum frequency of resolvable sound waves) and the temporal scheme. For 2nd-order accurate schemes, at least 5 time steps are required for one period [111]. Hence, in order to obtain the highest frequency content the acoustic data should be collected at every time step of $T_{min}/5$ where $T_{min} = 1/f_{max}$. This enforces that

$$\Delta t \leq \frac{1}{5 f_{max}}. \tag{3.2}$$

Nevertheless, the appropriate time step requires some experimentation in consideration of the grid resolution.

CHAPTER 4

VALIDATION STUDIES

This chapter presents the simulations that validate the code implementations of the methods. For the BCM transition model, incompressible flow simulations over a flatplate as well as an Eppler E387 airfoil are performed. In addition, an isentropic vortex convection case is tested for both the multiblock and the overset grid topologies. Lastly, the IDDES implementation is validated through a backward-facing step flow problem. All flow problems are performed as unsteady simulations.

4.1 Flatplate Test Case

Incompressible flow over a flatplate with zero pressure gradient is simulated via transitional DDES approaches. The freestream velocity is set to 5.4 m/s, and Reynolds number to 3.6×10^5 /m. Upstream turbulence intensity (Tu_∞) is taken 3.0%, yielding a bypass transition. This is a well-known validation problem in literature, called as the T3A case [103]. One of the verification flatplate grids from NASA Langley Reserch Center [80] is used. The grid is shown in Figure 4.1. It has $137 \times 97 \times 7$ grid nodes. Flow enters the domain in $+x$-direction, and goes over an inviscid wall before the viscous wall that starts at $x = 0$ m. The boundary conditions are given in Table 3.1. The nondimensional time step with respect to speed of sound[1] ($\Delta t^* = \Delta t c_\infty / L_{ref}$ where $L_{ref} = 2$ m) is 5×10^{-2}.

DDES-BCM and DDES-SLA-BCM3 are conducted for computations. Since there is no flow separation in this case, both methods yield exactly the same results. Hence, only DDES-BCM results are presented, here. For comparison, the same problem

[1] All nondimensional time steps are given with respect to speed of sound in this dissertation.

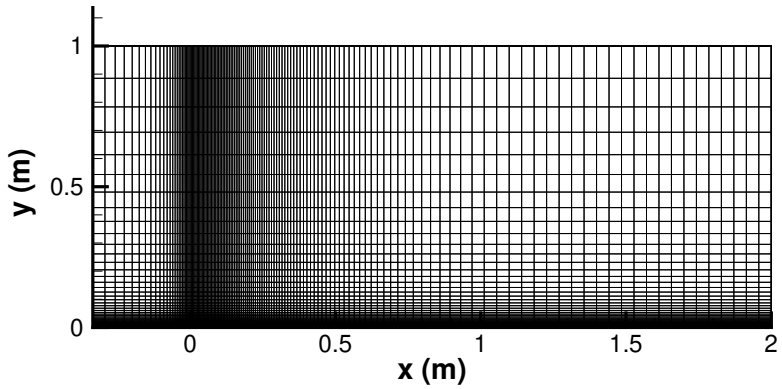


Figure 4.1: 2-D view of the computational domain of the flatplate test case

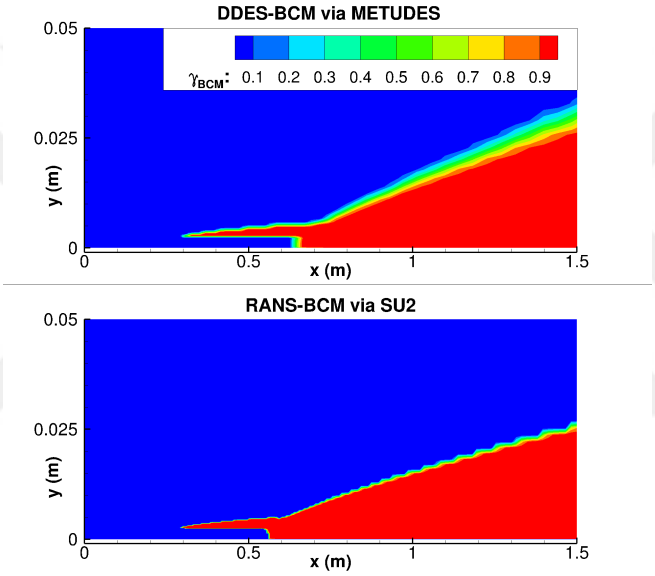


Figure 4.2: Comparison of γ_{BCM} distributions around the flatplate obtained by METUDES and SU2 codes

is performed by a steady RANS-BCM simulation using SU2 (Stanford University Unstructured) open-source software [29] in which the BCM model based on the S-A turbulence equation is present. Figure 4.2 shows the intermittency function, γ_{BCM}, distribution over the viscous wall. The turbulence equation is fully activated when $\gamma_{BCM} = 1.0$. DDES-BCM via METUDES reveals non-zero γ_{BCM} contours in the regions very similar to the ones obtained by SU2. However, METUDES estimates the onset of non-zero γ_{BCM} on the wall a little further than SU2 does. In Figure 4.3, triggering terms of the BCM model by METUDES are drawn, separately. It is

observed that Term_1 triggers the intermittency function at $x = 0.3$ m away from the wall, and then Term_2 takes the function inside the boundary layer approximately at $x = 0.6$ m. Hereby, it is understood that the slight difference is caused by Term_2. This is possibly due to the numerical algorithm discrepancies between the two codes because Term_2 constants were calibrated using SU2 in the original study [9].

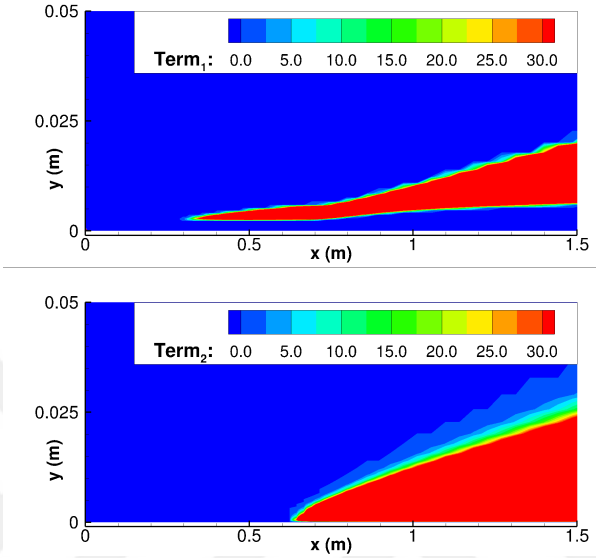


Figure 4.3: Distributions of Term_1 (above) and Term_2 (below) around the flatplate

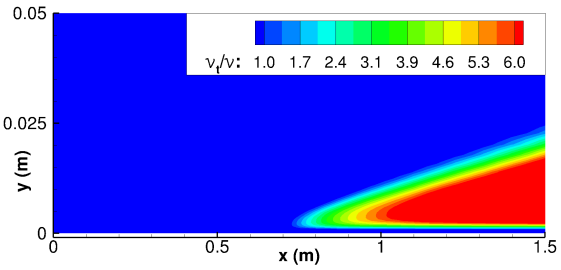


Figure 4.4: The eddy viscosity contours around the flatplate

The eddy viscosity contours are shown in Figure 4.4. Flow remains laminar up to $x \approx 0.7$ m, which is compatible with the previous figures. Then, the transition is triggered such that flow becomes fully turbulent in a short distance. This behavior can be observed clearly in Figure 4.5 where the friction coefficient, C_f, distribution along the wall are compared with an experimental study [103], the original study [9] that presents the BCM model via RANS, and another RANS study with the $\gamma - Re_\theta$

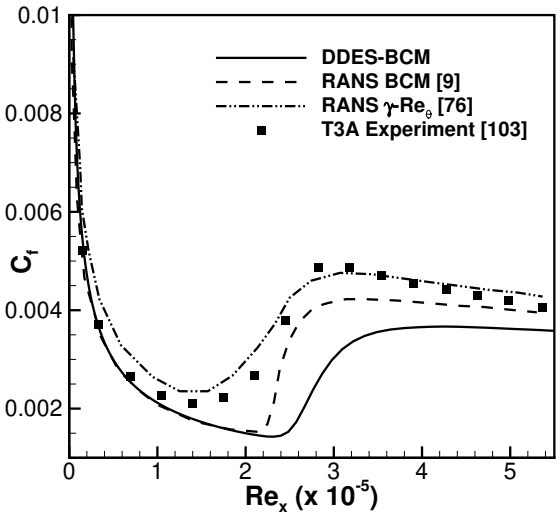


Figure 4.5: The friction coefficient distributions along the flatplate viscous wall

transition model [76]. The BCM models reveal similar C_f profiles. In both results, the laminar behavior is preserved till almost the same location where the production term of the turbulence equation is activated. However, although the flow suddenly goes into the fully turbulent regime in the original study, the current study exhibits a longer transition period. This also explains the discrepancy observed in Figure 4.2.

4.2 Eppler E387 Airfoil Test Case

Flow with freestream velocity of 3 m/s and Reynolds number of 2.0×10^5 /m over the airfoil is simulated via DDES, DDES-BCM, and DDES-SLA-BCM3. Upstream Tu_∞ is set to 0.1%, and the angle of attack (AoA) to 0°. Under these conditions, transition is expected to be initiated under an adverse pressure gradient on the suction side, after which a laminar separation bubble takes place. Hence, this case is tested for a separation-induced transition, as is commonly done in literature. Besides, there is a lot of available data regarding flow over the E387 airfoil in literature. An O-type DES grid is generated around the airfoil. Since the transition is expected to be triggered by the adverse pressure gradient, the streamwise grid number on the surface is important[2]. In this regard, two grids with different streamwise node number are

[2] Indeed, Term_1 requires a sufficient mesh resolution since it is the term that triggers transition.

created: Grid 1 has $257 \times 73 \times 7$ nodes whereas Grid 2 has $501 \times 73 \times 7$ nodes. The close view of Grid 2 is shown in Figure 4.6. Meshing details, boundary conditions, and initial conditions are provided in Chapter 3. $\Delta_{x,max}$ values on the surface of Grid 1 and Grid 2 are 8×10^{-3} /m and 19×10^{-3} /m, respectively. Accordingly, the spanwise mesh spacings, Δ_z, of each grid are determined to provide cubic cells. Moreover, the nondimensional physical time step is 1×10^{-2}.

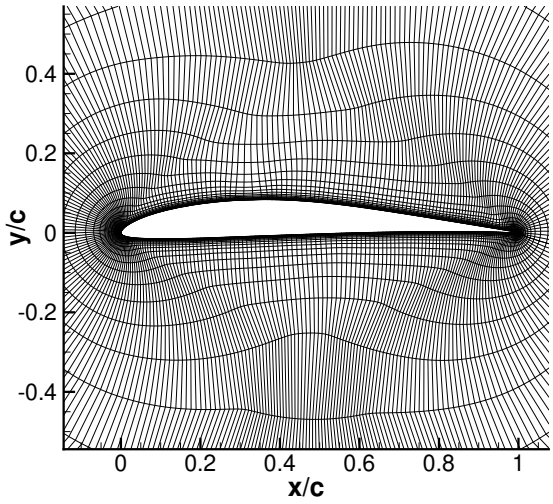


Figure 4.6: 2-D close view of Grid 2 for the E387 airfoil test case. Only odd-numbered points are shown.

The pressure coefficient distributions from all the current simulations on both grids are plotted in Figure 4.7. The results are compared with an experiment [73] and the original BCM study [9] where the corresponding 2-D grid had 699×179 grid nodes. The present results with the BCM model are in good agreement with the reference studies when Grid 2 is used. In contrast, use of Grid 1 fails to capture the ripple appearing around $x/c = 0.7$ on the suction side. A similar failure is seen from DDES with fully turbulent equations. Therefore, not only the transition model but also the streamwise grid points are important to predict the transition. Even though a slight difference is observed around the ripple, the proposed BCM model (BCM3) to be compatible with DDES-SLA achieves almost the same distribution as in DDES-BCM.

Instantaneous distributions of the triggering terms of BCM are presented in Figure

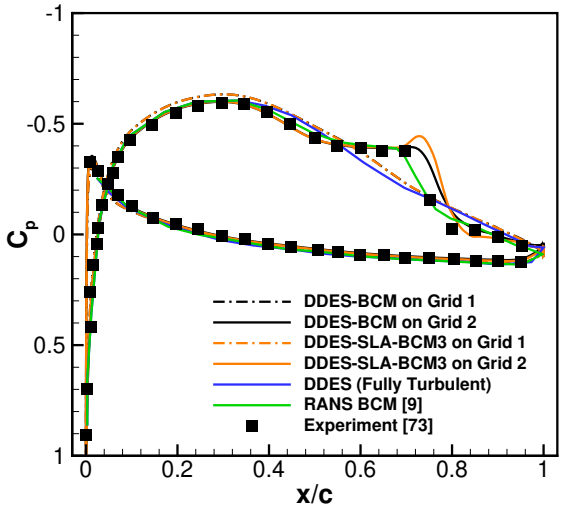
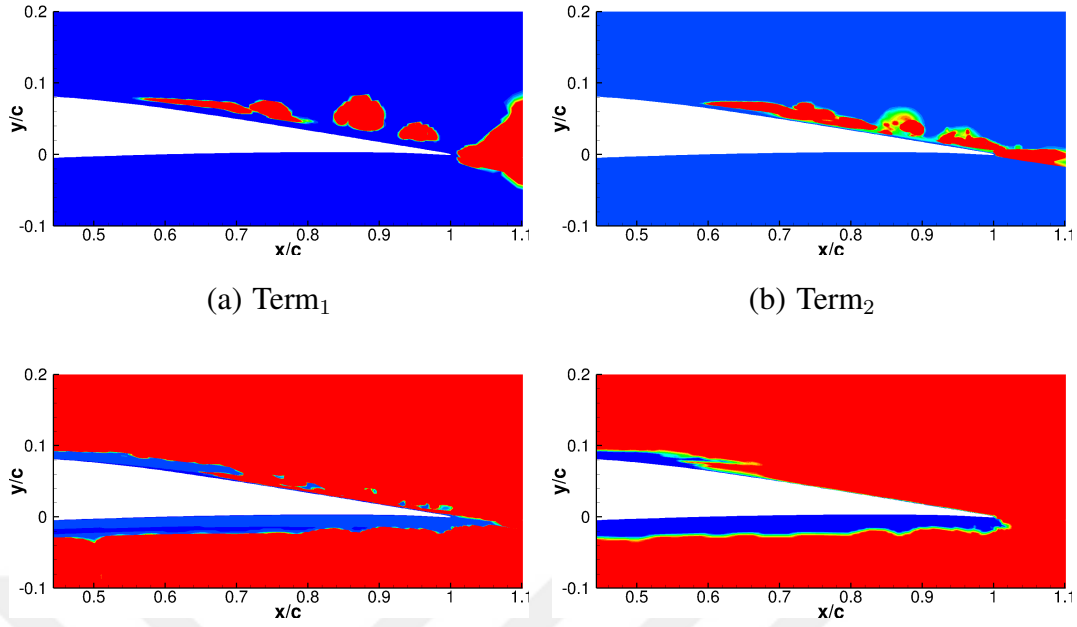


Figure 4.7: The pressure coefficient distributions along the E387 airfoil surface

4.8. These are obtained by DDES-SLA-BCM3; therefore, Term_3 is also included in the figures. The intermittency function becomes 1.0 between x/c of 0.6 and 0.7 near the wall, and in the whole upstream (except very close to the wall, inherently), the turbulence production is fully activated (see Figure 4.8d). Unlike the previous case, γ_{BCM} is also 1.0 outside the boundary layer where the flow is already laminar. This is caused by the mathematical expression of Term_3 in which VTM sensor has nonzero values in inviscid regions (see Section 2.1.3.4). Again, the intermittency function is triggered by Term_1 (at $x/c = 0.6$), and Term_2 takes the generated function inside the boundary layer (at $x/c = 0.7$). As discussed in Section 2.2.1.1, in unsteady simulations the continuity of Term_1 appearance along upstream is difficult to ensure, which is observed in Figure 4.8a. Since the unsteadiness is weak in this problem (the flow is steady, but, time-marching is unsteady), Term_2 provides for the generation of γ_{BCM} in most of the upstream (see Figure 4.8b). Term_3 compensates the remaining gaps as desired (see Figure 4.8c).

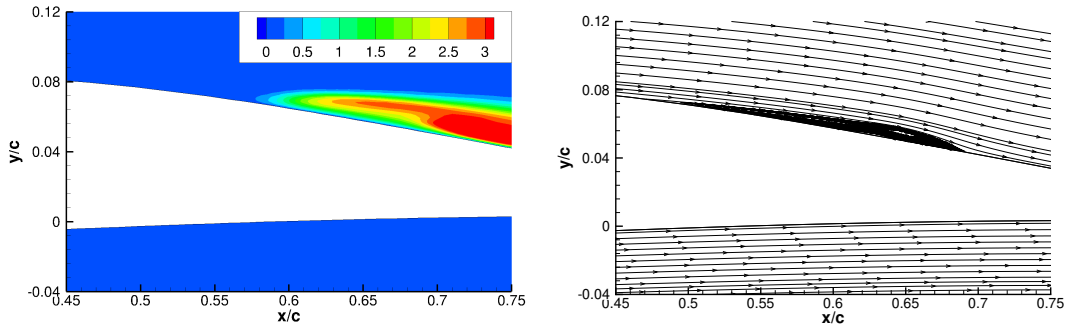
The averaged flow field with eddy viscosity contours and streamlines are shown in Figures 4.9a and 4.9b, respectively. The eddy viscosity, on the suction side, is generated starting from $x/c \approx 0.6$. After that, the flow becomes fully turbulent at $x/c = 0.7$. Meanwhile, a separated region is observed between $x/c = 0.5$ and $x/c = 0.7$. Both figures show that the incoming laminar flow separates at $x/c = 0.5$,



(a) Term_1 (b) Term_2

(c) Term_3 (d) γ_{BCM}

Figure 4.8: Instantaneous distributions of the triggering terms (red color: 30.0) and the intermittency function (red color: 1.0) around the E387 airfoil



(a) $\hat{\nu}_t/\nu$ (b) Streamlines

Figure 4.9: The eddy viscosity contours and the streamlines indicating the laminar separation bubble around the E387 airfoil

and then, it reattaches at $x/c = 0.7$ as fully turbulent, forming a laminar separation bubble. This is the transition mechanism which is quite compatible with the observations in Figures 4.7 and 4.8 as well as the original BCM study [9]. The pressure side, on the other hand, is kept completely laminar as expected.

To conclude, the flatplate and the E387 airfoil results validate the BCM model implementations into METUDES. In addition, it is demonstrated the incorporated model works with the DDES frameworks properly in steady flows even though they are solved by unsteady time integration.

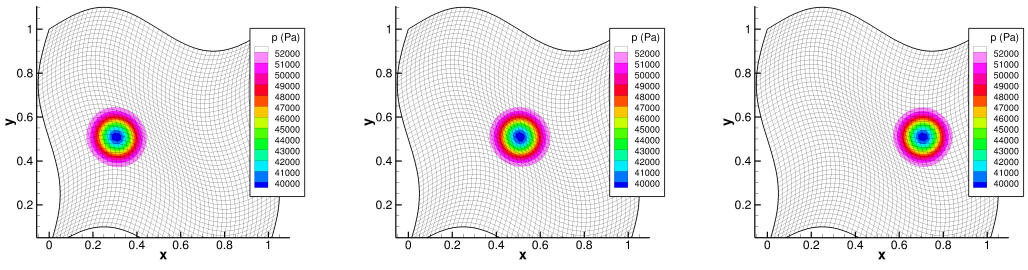
4.3 Isentropic Vortex Convection

The implementations of the multiblock and overset grid topologies are validated through an isentropic vortex convection problem. An isentropic vortex is generated by Gaussian distribution on a single sinusoidal structured grid having $50 \times 50 \times 7$ grid cells (see Figure 4.10a). The vortex is convected in the $+x$-direction. The shape of the vortex must be preserved during the convection process due to absence of diffusion. The time step of the 2nd-order accurate time integration is selected sufficiently small not to spoil the 4th-order accuracy from the spatial scheme. In Figures 4.10a-c, the pressure distribution is shown at sequential times (from t_0 to t_2). The shape is preserved as expected.

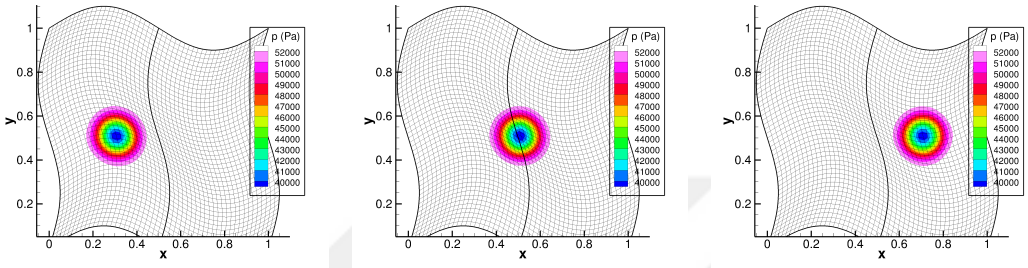
The same problem is tested on the same grid which is divided into two separate single blocks where the interface cells overlap perfectly. At the interface, the one-to-one multiblock communication is set as a boundary condition. The results shown in Figures 4.10d-e point out that the multiblock implementation works as desired.

In the next test, the second block is replaced with a Cartesian mesh block (see Figure 4.10g). There is no interface, this time. Instead, the overlapping region includes two different grid topologies. The solution is repeated by the 2nd- and the 3rd-order overset interpolation techniques, and their results are shown in Figures 4.10g-i and Figures 4.10j-l, respectively. It is observed that use of the 2nd-order interpolation causes some distortions on the vortex shape. On the other side, the 3rd-order interpolation preserves the shape during the convection.

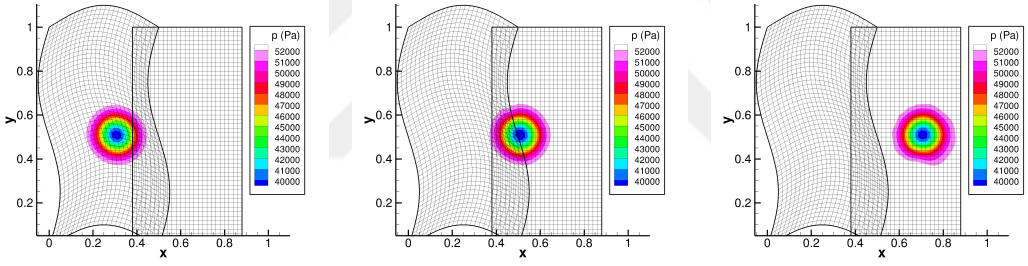
For each plot in Figure 4.10, a cut through the isentropic vortex at $y = 0.5$ m (along the vortex center) is taken, and normalized. The resulting pressure distributions are shown in Figure 4.11. It is observed that although the vortex is perfectly convected through the identical overlap region by one-to-one communication, some distortions



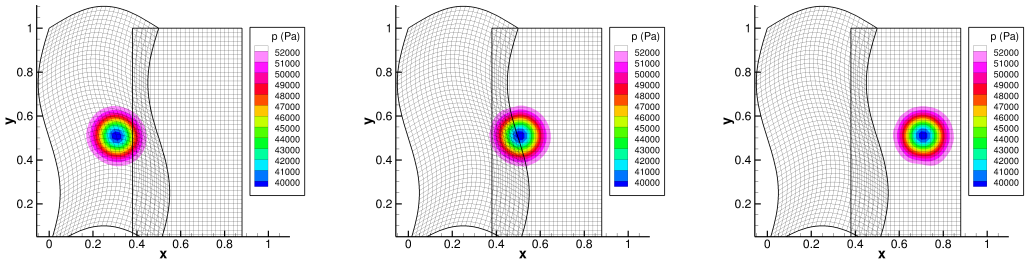
(a) $t = t_0$, single (b) $t = t_1$, single (c) $t = t_2$, single



(d) $t = t_0$, one-to-one (e) $t = t_1$, one-to-one (f) $t = t_2$, one-to-one



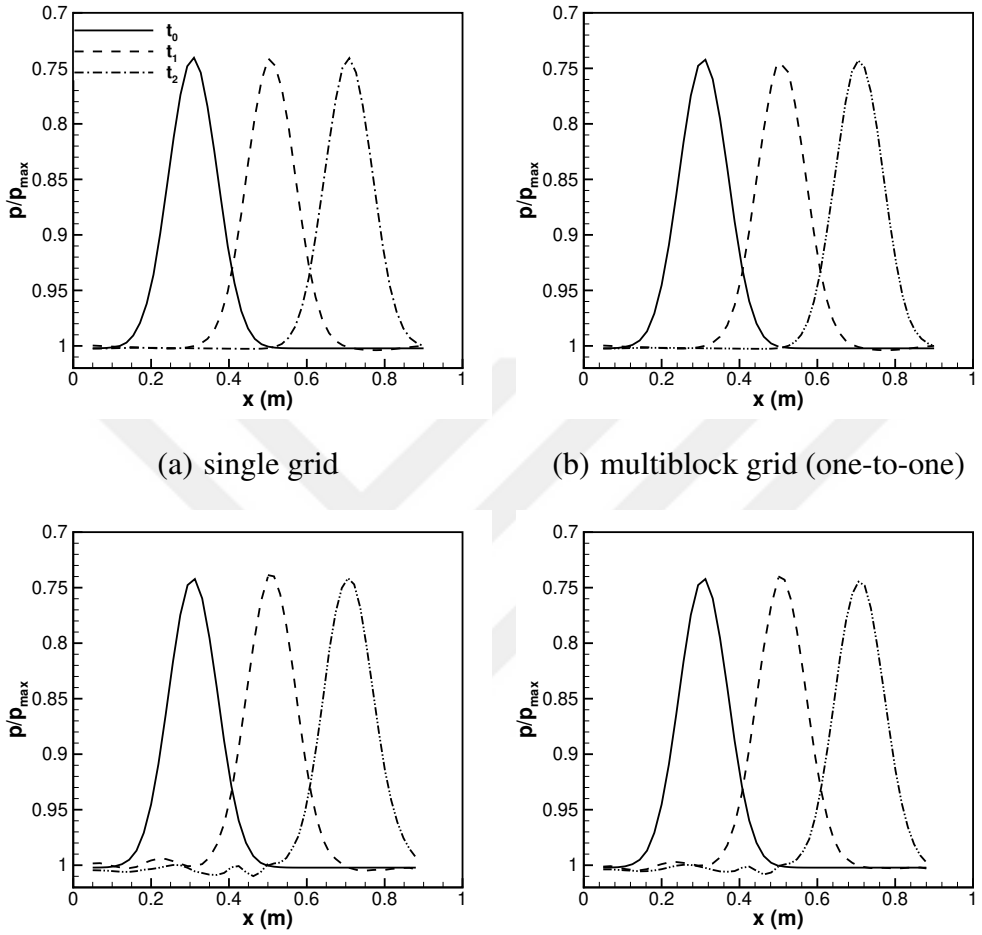
(g) $t = t_0$, 2nd-order (h) $t = t_1$, 2nd-order (i) $t = t_2$, 2nd-order



(j) $t = t_0$, 3rd-order (k) $t = t_1$, 3rd-order (l) $t = t_2$, 3rd-order

Figure 4.10: Pressure contours of the isentropic vortex convected along single (a-c) and multiblock (d-l) domains at sequential times. Communication between two blocks is conducted by one-to-one (d-f), the 2nd-order overset interpolation (g-i), and the 3rd-order overset interpolation (j-l).

appear on the overset grids. This is partly due to the different grid topologies. Nevertheless, using the 3rd-order overset interpolation reveals less distortions than using the 2nd-order one. As a result, it is decided to use the 3rd-order interpolation for the overset boundary conditions.



(a) single grid (b) multiblock grid (one-to-one)

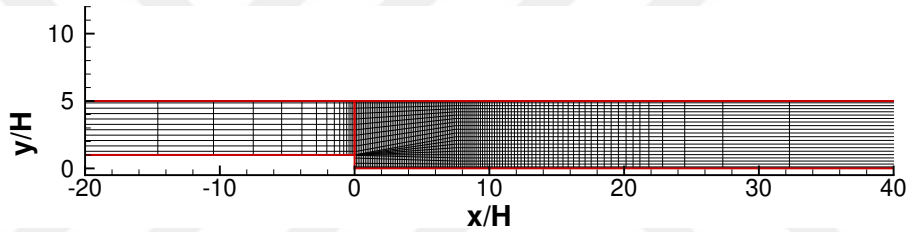
(c) overset grid (2nd-order) (d) overset grid (3rd-order)

Figure 4.11: Normalized pressure distribution of the isentropic vortex along $y = 0.5$ m at sequential times. The plots are obtained from Figure 4.10.

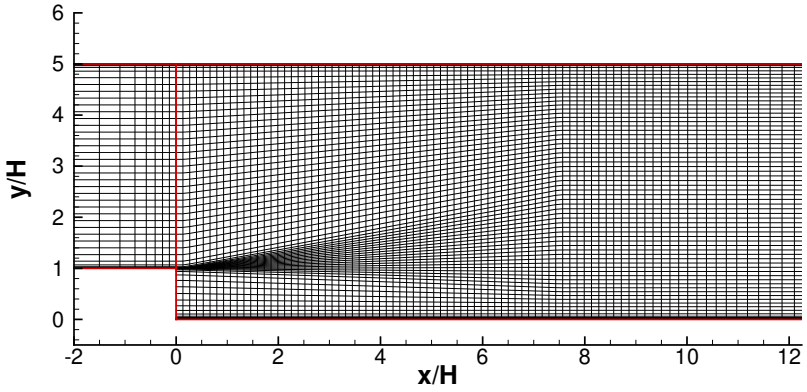
4.4 Backward-Facing Step Flow

As discussed in Section 2.2.1.2, in DDES the RANS/LES interface (the grey-area) shows up around the boundary layer edge whereas the interface shifts to the border between the inner and outer layers in case of WMLES. The IDDES length scale is

simply a blend of these two approaches. In this context, the backward-facing step flow is a good test case for validating the IDDES implementation as the case includes the RANS/LES interfaces of both the DDES and WMLES frameworks, in separate regions. This problem is a kind of a channel flow where an abrupt sectional change exists beyond which the lower wall is shifted downward (see Figure 4.12). Here, it is expected that the upcoming attached boundary layer is treated as RANS, and the separated flow turns out to be a LES region, forming a typical DDES case. Additionally, the separated flow reattaches to the wall one step below; therefore, the WMLES mode gets activated because the inflow already has turbulent contents. This kind of flow is similar to one that appears in open cavity flow problems except the aft wall. In open cavities, on the other hand, there is only an impingement on the aft wall which can be treated as a reattachment zone. Consequently, the backward-facing step flow is also a good test problem before conducting cavity flow simulations.



(a) far view



(b) close view

Figure 4.12: 2-D views of the computational grid of the backward-facing step flow problem. One quarter of nodes are shown. Red lines indicate the block edges.

The simulation parameters are selected to make comparisons with the experiment of

[120] and the IDDES study of [105]. The Reynolds number is $28,000$ based on the step height (H), and the Mach number is approximately 0.1. The channel has a depth of $4H$; hence, the area expansion ratio due to the step is $5/4$. The upstream viscous wall length before the step is set as $51H$ to achieve the measured boundary layer thickness of $1.07H$ at $x/H = -3.8$ in the experiment. There is also an inviscid part between the uniform inlet and the viscous wall, as in the flat plate problem described earlier. The span length is $2H$ with 30 cells distributed uniformly, which matches with the IDDES base study. The computational grid is composed of two blocks ($73 \times 169 \times 31$ and $481 \times 301 \times 31$ grid nodes, separately) communicated by one-to-one multiblock topology. Far and close views of the grid with the edges of the blocks are shown in Figure 4.12. The mesh is created following the guidelines given in Section 3.1 except that the stretching ratio inside the boundary layers along the reattachment wall is replaced by 1.14 as proposed in [105]. Besides, the grid nodes of the WMLES zones are clustered in the streamwise direction as shown in Figure 4.12.

The simulation is carried out by IDDES. Δt^* of the unsteady simulation is set to 6×10^{-2}. The mean flow field is obtained by averaging the field over time after the initial transient period passed. The friction coefficient distribution along the reattachment wall is compared in Figure 4.13 with the measurements [120] as well as RANS, DDES, and IDDES (based on the S-A equation) results of [105]. The trend of the current C_f distribution is similar with the experiment and the IDDES base results. The negative peak, indicating a recirculating zone, appears at around $x/H = 5$. The straight lines past the $x/H \approx 12$ station represent the recovery region. The current results show an overprediction in the recirculating zone and an underprediction in the recovery zone, slightly. This might be due to the mesh resolution and/or the solver accuracy. On the other hand, it is clear that RANS fails to capture the flow behavior, entirely. Furthermore, DDES could not predict the recirculating zone as accurately as IDDES. These prove the superiority of IDDES in the reattached flow region.

Figure 4.14 shows Q-criterion isosurfaces at an instance of unsteady computations which clearly reveal vortical structures related to the developing eddies. The flow appears perfectly 2-D up to the step corner. After separation, the flow turns into one containing 3-D structures following a quasi-2D short region. This points out to a switch from the RANS to the LES modes of IDDES. In the vicinity of the wall one

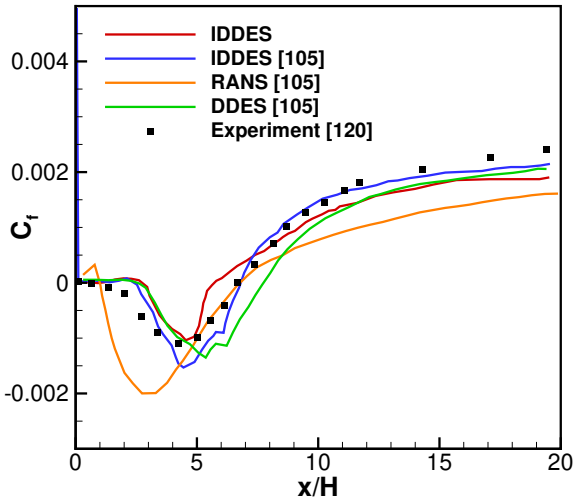


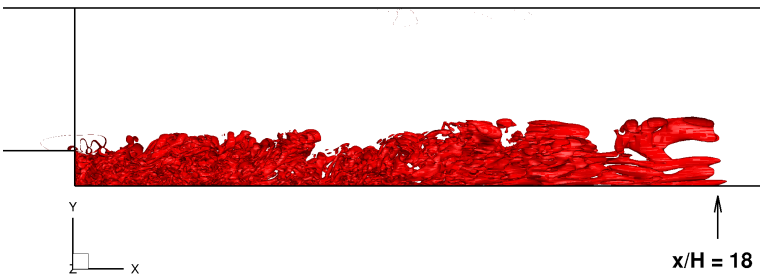
Figure 4.13: Comparison of the friction coefficient distributions along the reattachment wall

step below, smaller eddy structures are observed. The WMLES mode is expected to activate, there. The structures become bigger through the recovery region, and around $x/H = 18$ the flow becomes 2-D again (see Figure 4.14a).

Figure 4.15 presents some variables to help understand the switching mechanism of IDDES. Recall that the IDDES length scale is defined in Section 2.2.1.2 as

$$l_{\text{IDDES}} = \tilde{f}_d(1 + f_e)d_w + (1 - \tilde{f}_d)C_{\text{DES}}\Delta_{\text{IDDES}}$$

This equation tells that when $\tilde{f}_d$ becomes zero, the length scale is equal to $C_{\text{DES}}\Delta_{\text{IDDES}}$, and therefore, the domain is treated as pure LES. When $\tilde{f}_d = 1$, the wall distance, d_w, takes over such that the RANS mode is activated. Figure 4.15a shows the $\tilde{f}_d$ contours where the dark regions represent the RANS mode, and the white regions represent the LES mode. The RANS regions are thinner in the reattachment zone than over the pre-separation wall and the upper wall. The reason can be understood by analyzing the f_B contours shown in Figure 4.15b. Recall that $\tilde{f}_d = \max(1 - f_{dt}, f_B)$, and in WMLES zones, $\tilde{f}_d$ is equal to f_B. Comparing both figures shows that near the reattachment wall from the step corner ($x/H = 0$) to the recovery region ($x/H \approx 18$), $\tilde{f}_d$ takes its value from f_B. Hence, these regions (marked in Figure 4.15a) are where IDDES



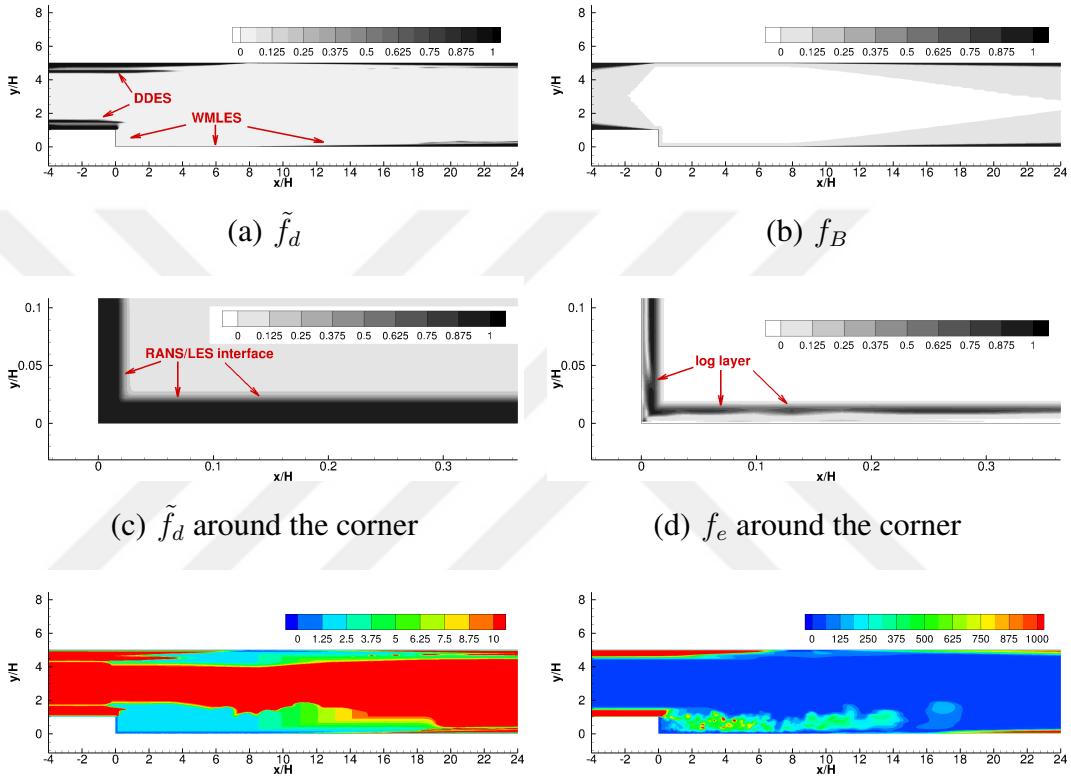
(a) 2-D view



(b) 3-D view

Figure 4.14: Isosurfaces of Q-criterion ($Q = 0$) of an instantaneous flow field around the backward-facing step geometry from different views

behaves as WMLES by limiting the RANS mode very close to wall. Likewise, $\tilde{f}_d$ differs from f_B in the rest of the domain, which is treated as DDES. In addition, the vicinity of the walls in the WMLES regions are investigated in Figures 4.15c-d. The color change in Figure 4.15c shows the RANS/LES interface, appearing at the end of the log layer. In order to prevent the Log Layer Mismatch problem (see Section 2.2.1.2), the elevating function, f_e, goes to 1 inside the log layer (see Figure 4.15d), and thereby compensating for the reduction in the modeled Reynolds stresses. As a result, the ultimate length scale and the eddy viscosity are obtained as in Figures 4.15e and 4.15f, respectively. It is inferred that the reduction of the length scale as well as the eddy viscosity starts around the same region of the appearance of 3-D structures in Figure 4.14. Then, they both begin to increase in the recovery region.



(a) $\tilde{f}_d$ (b) f_B

(c) $\tilde{f}_d$ around the corner (d) f_e around the corner

(e) l_{IDDES} (f) $\hat{\nu}_t/\nu$

Figure 4.15: Some variables from an instantaneous flow field around the backward-facing step geometry

CHAPTER 5

TRANSITIONAL AND CAVITY FLOW SIMULATIONS

This chapter presents the simulations regarding the boundary layer transition as well as the cavity noise predictions. Transition simulations are carried out over the NREL S826 wind turbine blade profile near the stall threshold as well as over a circular cylinder. For the latter, results of a drag crisis phenomena, in which as Reynolds number increases the drag coefficient decreases suddenly, are shown. Both studies correspond to severe situations for DDES, as the flow fields include not only large separated regions but also laminar separation bubbles, slight separations, and reattachment. By these particular studies it is aimed to improve aerodynamic coefficients by providing DDES with transitional behavior. Transonic and supersonic flow simulations over open cavities are conducted as well. Combining the modifications made to the DDES, it is aimed to estimate the acoustic field resulting from the complex flow phenomena over such cavities.

5.1 Flow over an NRELS826 Blade Section

3-D unsteady flow around the NRELS826 wind turbine blade profile, which was designed for turbines with a span of $10-15$ meters by the National Renewable Energy Laboratory (NREL), is simulated using DDES, DDES-SLA, and DDES-SLA-BCM3 approaches. The flow parameters of the problem are selected according to those of the available literature data: experimental measurements by Technical University of Denmark (DTU) wind tunnels [102], the numerical studies by Çakmakçıoğlu *et al.* [8] that performed URANS based on $k-\omega$ shear stress transport equations with Langtry-Menter transition prediction model (denoting as $k-\omega$ SST Transition, in the rest of

this study) as well as DDES based on S-A using CFD++ commercial software, and the numerical results of Sarlak *et al.* [101] using LES through DTU's CFD solver, EllipSys3D.

Table 5.1: Blade and flow parameters of the benchmark studies where U_∞ is the freestream velocity, Tu_∞ is the freestream turbulence intensity, and s/c is the span-to-chord ratio

	Re number	U_∞ (m/s)	Tu_∞	s/c
LES [101]	100,000	15	%0.2	0.12
Experiment [102]	100,000	15	%0.2	5
DDES [8]	145,000	20	N/A	5
$k-\omega$ SST Transition [8]	145,000	20	N/A	5

Some flow and geometric parameters of the benchmark studies are given in Table 5.1. The simulations are carried out for two Reynolds numbers of $100,000$ (Re_1) and $145,000$ (Re_2). Mach number is set to ~ 0.06, which corresponds to 20 m/s. The selected AoAs are $4°, 6°, 8°, 10°$, and $12°$ for Re_1, whereas $8°, 10°$, and $12°$ for Re_2.

5.1.1 Configurations and Setups

5.1.1.1 Geometry

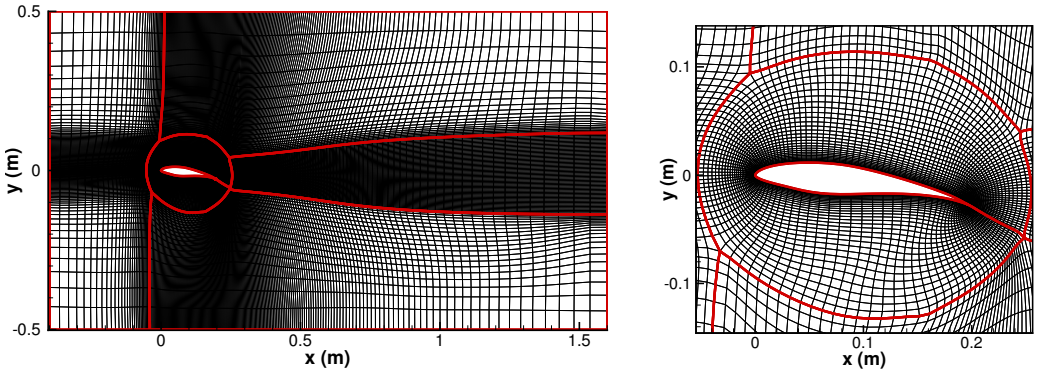
DTU wind tunnel test section dimensions are $1 \times 1 \times 2$ m. The chord length of the wing is 0.2 m. In this study, a computational domain is built with the same dimensions as the tunnel, except in the spanwise direction. In the experiment the blades has a wall-to-wall span with negligible gap or full contact between the blade tips and the side walls of the wind tunnels. Therefore, an infinite span with periodic conditions is preferred in the numerical simulations in order to reduce the computational expense. In classical DES simulations of massively detached flow, the spanwise length is mostly taken as 1 chord length [111]. In contrast, the LES study by [101] shows that a span-to-chord ratio (s/c) of 0.12 is sufficient for slightly separated flows, as in the current problem. In this regard, the mesh is formed with a blade span of 0.15

chord length. Nevertheless, for the highest AoA, a span-length-sensitivity analysis is performed by doubling the span (see Section 5.1.2.1), since the spanwise length becomes more critical when stall starts due to spanwise correlations of separation bubbles.

The location of the blade leading edge with respect to the inlet is similar to that of the experiment when viewed in the same scales. Since the wind tunnel has fixed inlet flow direction parallel to its wall surfaces, various angles of attack are configured by rotating the airfoil itself.

5.1.1.2 Grid Generation

A multiblock structured mesh is generated in 2-D, and then extruded along spanwise direction for 0.15 chord length (see Figure 5.1). The first block includes an O-mesh structure around the airfoil and the remaining 4 blocks extend the mesh domain to the tunnel walls, and inlet & outlet boundaries, as shown in Figure 5.1a. This is a tunnel grid with an O-H type multiblock topology. In order to be able to capture the wake region, one block with higher resolution is created in the expected wake region of the blade section. The mesh resolution is set in accordance with the criteria given in Section 3.1. All grids are built considering Re_2, and used for both Reynolds numbers. In the wall-normal direction, $y^+ \approx 1$. In the streamwise direction, $\Delta x^+_{max} \approx 100$ on the suction side, and $\Delta x^+_{max} \approx 180$ on the pressure side. In the spanwise direction, all blocks have 25 grid points uniformly distributed with $\Delta z^+ \approx 45$ which corresponds to 6.25×10^{-3} chord length. This dimensionless spacing is approximately 3.5 times that of the benchmark LES study. The O-mesh around the airfoil has $297 \times 71 \times 25$ cells whereas the whole domain contains $947,175$ cells in total. The airfoil geometry and block structure together with an enlarged view of the O-mesh can be seen in Figure 5.1b. Table 5.2 compares the grids and the numerical solvers used in the current and the benchmark studies. It is expected that the use of higher accuracy order gives the freedom of using coarser grid than the benchmark studies.



(a) O-H type mesh for the whole grid domain composed of 5 blocks

(b) O-mesh around the airfoil. Every other grid lines in both directions are shown.

Figure 5.1: 2-D views of the tunnel grid with multiblock topology around the blade section having AoA of 8°

Table 5.2: Simulation parameters of the current and benchmark studies

	# of cells	y^+	mesh type	solver accuracy
Current study	947,175	≈ 1	O-H (multiblock)	4th-order
$k-\omega$ SST Transition as well as DDES [8]	11,434,420	< 1	O-H (overset)	2nd-order
LES [101]	16,777,216	$\approx$ 1-2	O-H (multiblock)	2nd-order

5.1.1.3 Boundary Conditions

The boundary conditions for the computational domain are given in Figure 5.2. The application of each condition is described in Section 3.2. It should be noted that in the studies of $k-\omega$ SST Transition and DDES, the effects of the top, bottom and lateral tunnel walls were all included through no-slip wall conditions. On the other hand, the LES study used slip wall conditions at the top and bottom walls, and periodic boundary conditions at the spanwise ends of the domain to reduce the computational cost, exactly as in the present study. The inlet and outlet conditions are the same as those of the benchmark studies except a characteristic based inflow boundary type was used in the $k-\omega$ SST Transition and DDES studies.

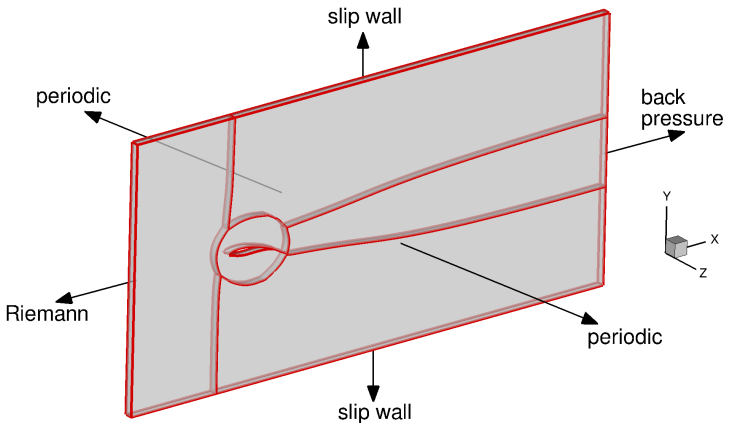


Figure 5.2: 3-D view of the computational domain with boundary conditions

5.1.2 Results and Discussion

Simulations are carried out using 120 processors until the flow statistics converge. Convergence of the flow statistics is determined by drawing the running average of the aerodynamic coefficients, typically as shown in Figure 5.3. Unsteady data are collected from $t_1^* = 150$ to $t_2^* = 250$. Hence, convergence requires approximately 6 chord convection times based on the freestream velocity. Note that $\Delta t^* = 2.5 \times 10^{-3}$.

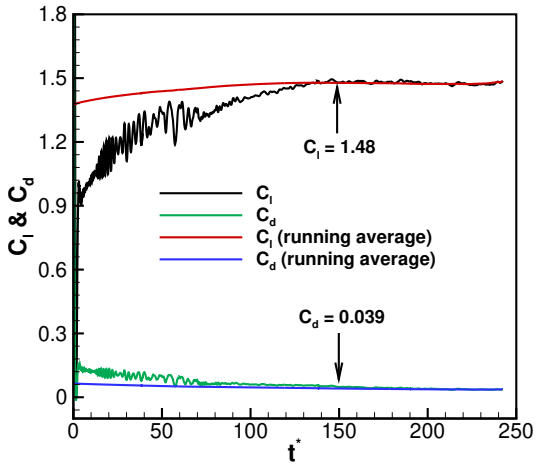


Figure 5.3: Lift and drag coefficients together with the running averages of the blade profile changing with dimensionless time at AoA of 10° and Re_1 via DDES-SLA-BCM3

5.1.2.1 Grid Dependency Analysis

In 2-D domain, no grid dependency analysis is done in this case, since this is only a comparative study with focus on showing the superiority of the SLA length scale over the standard DDES length scale for revealing the LES-like structures on the same mesh. Thus, only the spanwise length sensitivity is analyzed. It is conducted by doubling the span dimension. When the flow goes into stall, scope of 3-D effects on the aerodynamic results might increase, that is, larger structures in the spanwise direction could emerge. Hence, the high AoA case, i.e. AoA of $12°$, is selected for comparisons. Note that for both Reynolds numbers in consideration (Re_1 and Re_2), this AoA shows a near-stall or post-stall (see Section 5.1.2.2 and Section 5.1.2.3). The results of DDES-SLA in Figure 5.4 show that the pressure coefficient, C_p, distributions of the cases with s/c of 0.15 and s/c of 0.30 for Re_1 almost coincide. When the lift and drag coefficients (C_l and C_d) are compared, only slight differences are observed (0.35% for C_l and 1.8% for C_d). Consequently, s/c of 0.15 is considered sufficient to resolve the 3-D structures. The simulations shown hereafter are performed using the grids with s/c of 0.15.

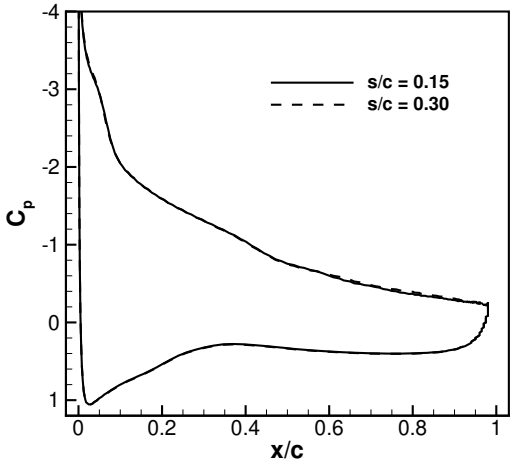


Figure 5.4: C_p distributions over the blade surface at AoA of $12°$ and Re_1 via DDES-SLA

5.1.2.2 Case 1: Reynolds number of 100,000

This section presents the aerodynamic results for the Re_1 case. In Figure 5.5, C_l and C_d values of the wind turbine blade profile are compared with those from the LES and experimental studies. As seen in the figure, the lift slopes in the linear region obtained from all current simulations are in good agreement with the measurement. Despite the much coarser meshes employed, the current simulation approaches both capture the C_l values more accurately than LES in both pre- and post-stall regions. This is mainly due to the numerical scheme discrepancies of the solvers[1]. In the current studies, stall occurs at AoA of $10°$, the same as the measurement. On the other hand, a similar trend in the C_d curves is observed in Figure 5.5. After stall, the discrepancies between the studies increase. Moreover, DDES and DDES-SLA appear to have yielded almost the same levels in both aerodynamic coefficients. Despite a slight difference in C_l around stall, use of the BCM transition model makes significant changes to C_d. In fact, C_d values of DDES-SLA-BCM3 are in very good agreement with those of the experiment.

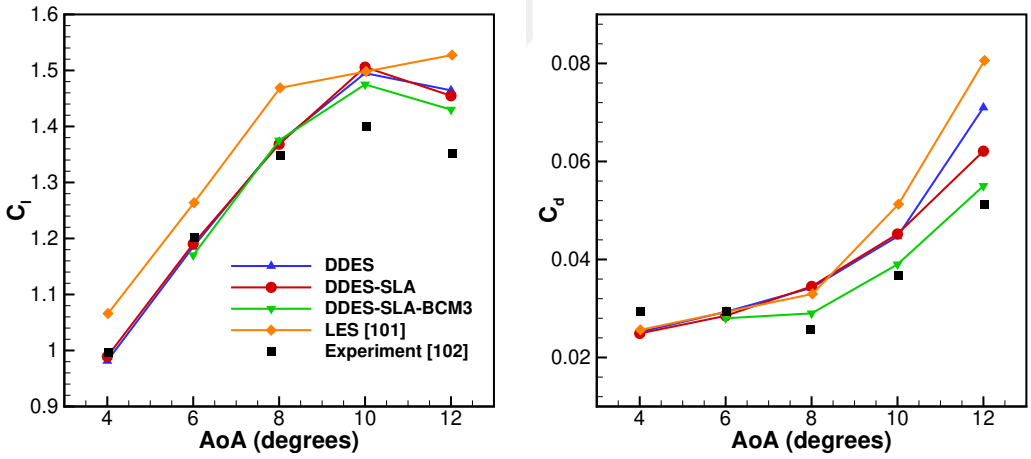
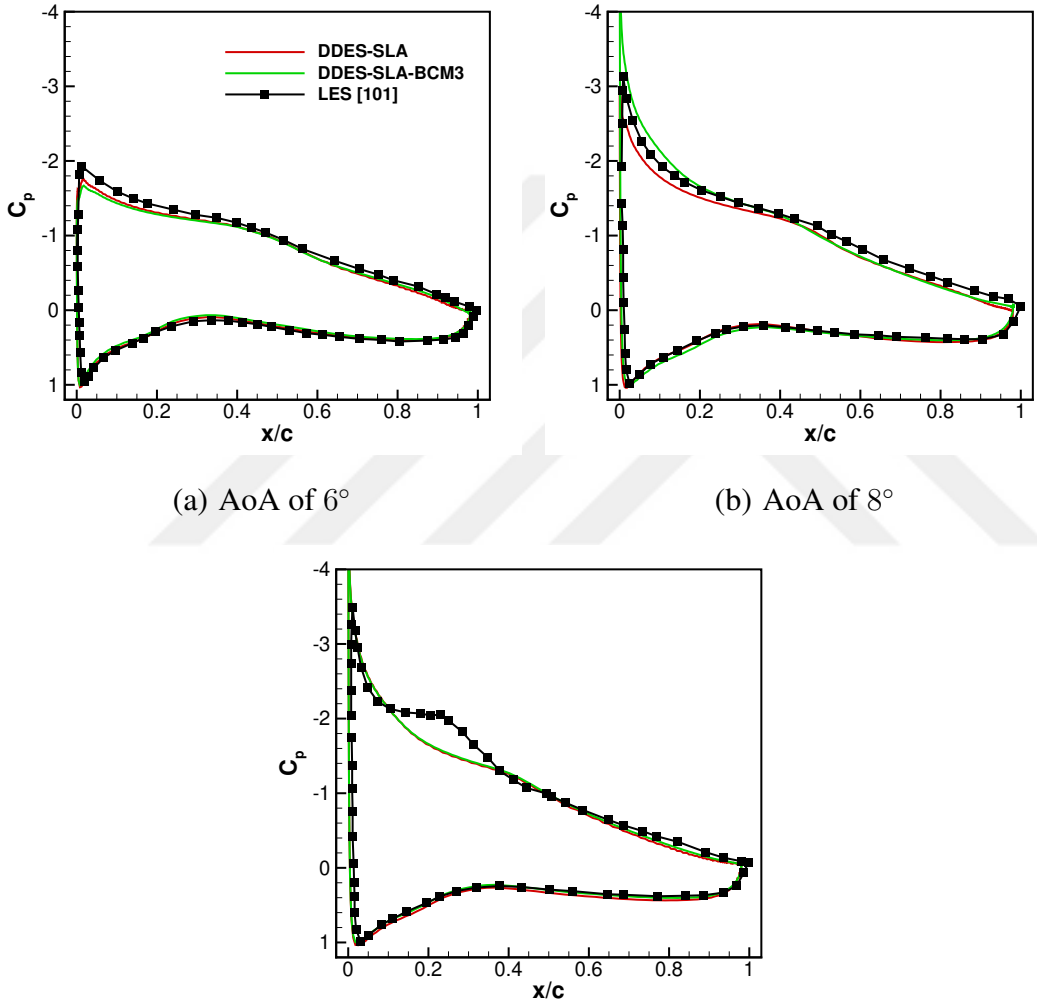


Figure 5.5: C_l and C_d values of the wind turbine blade profile for several AoAs around stall ($\mathrm{Re} = 100,000$)

Figure 5.6 shows the C_p comparisons with the available AoAs from the benchmark LES study. Since quite similar C_p profiles are given by DDES and DDES-SLA (as

[1] In the LES study [101], the deviations from the experiment is related to inability to estimate the transition point, the limitations of the subgrid scale model of LES, the numerical schemes, and the short span width. The main difference between the current study and the LES one is due to the numerical discretization schemes.

expected from lift coefficients), DDES ones are not included. The results are in good agreement to a great extent. However, at AoA of $10°$, the present simulations show neither a separation nor a reattachment as opposed to the LES study, which might be a clue explaining the difference in stall estimations as previously stated. Note that in the LES study (see [101]) they related this unexpected prediction of separation to incapabilities of the standard Smagorinsky subgrid scale model. In general, between DDES-SLA and the one with the transition model, there is no significant difference.



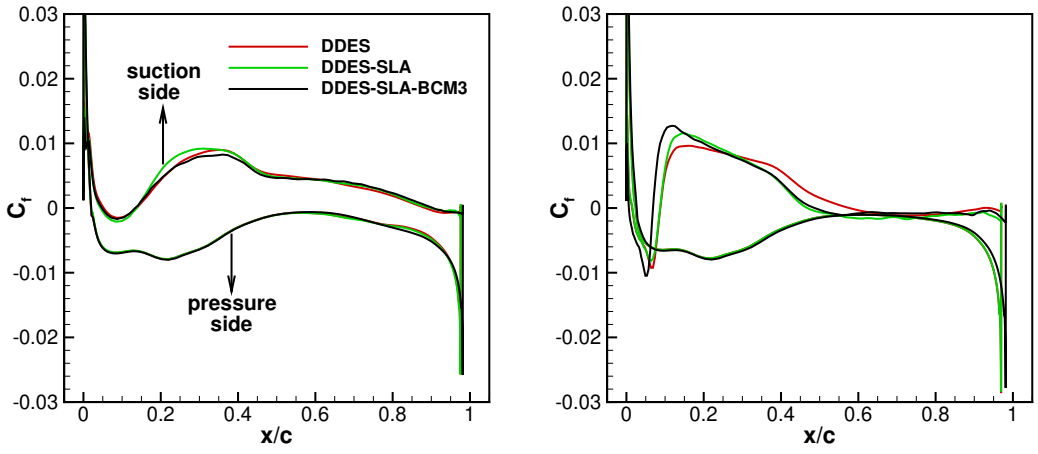
(a) AoA of $6°$ (b) AoA of $8°$

(c) AoA of $10°$

Figure 5.6: C_p distributions over the blade surface for various AoAs (Re $= 100,000$)

Presented in Figure 5.7 are the friction coefficient distributions (C_f) along the blade surface, which possibly explains the discrepancies observed in C_d predictions. At

AoA of $10°$, all DDES frameworks give almost the same results whereas at AoA of $12°$ some differences occur on the suction side. The peak in the profiles at AoA of $12°$ is an indication to flow separation, causing boundary layer transition. The transition model, at this point, changes the onset of this separation, which is also observed in Figure 5.8. The flow separation starts at $x/c \approx 0.06$ both in the DDES and DDES-SLA computations while at $x/c \approx 0.05$ in the DDES-SLA-BCM3 ones. The flow is laminar before separation, and turbulent after the reattachment point, as also indicated by the eddy viscosity levels in Figure 5.10. Hence, this is a separation bubble inducing the transition mechanism. Since it appears to be located very close to the leading edge, nearly a sharp stall occurs. Here, the transition model suppresses the eddy production completely for a very short distance before separation, and thereby providing a pure laminar separation. Figure 5.9, which shows the intermittency function contours, supports this conclusion. The function is zero between $x/c = 0$ and $x/c \approx 0.05$ over the suction side as well as all over the pressure side as expected. In the other frameworks, the separation onset is retarded slightly due to missing transition information, which makes a significant difference in estimating the drag coefficients (reconsider Figure 5.5). Nonetheless, the separations observed in the DDES and DDES-SLA computations are still laminar, which is enabled by setting the initial condition of eddy viscosity as almost zero by using the modified version of the S-A equation.



(a) AoA of $10°$ (b) AoA of $12°$

Figure 5.7: C_f distributions over the blade surface for various AoAs (Re $= 100,000$)

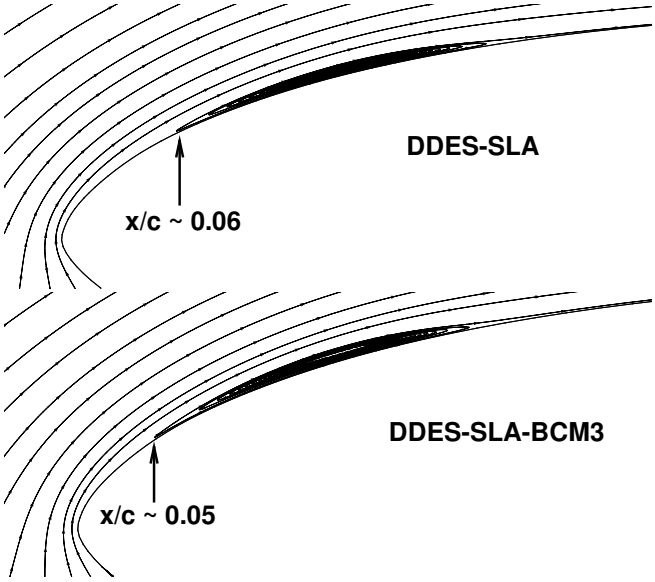


Figure 5.8: Laminar separation bubble observed around the leading edge at AoA of 12° via DDES-SLA and DDES-SLA-BCM3 (Re $= 100,000$)

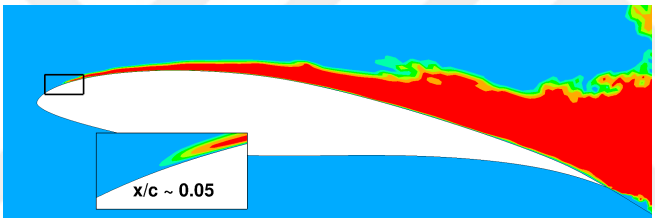
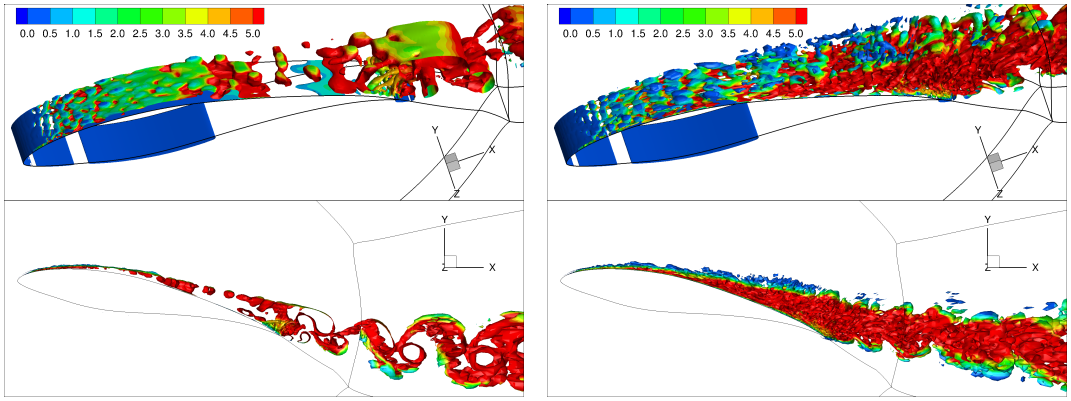


Figure 5.9: The intermittency function contours (red: $\gamma_{BCM3} = 1.0$) around the blade via DDES-SLA-BCM3 (Re $= 100,000$)

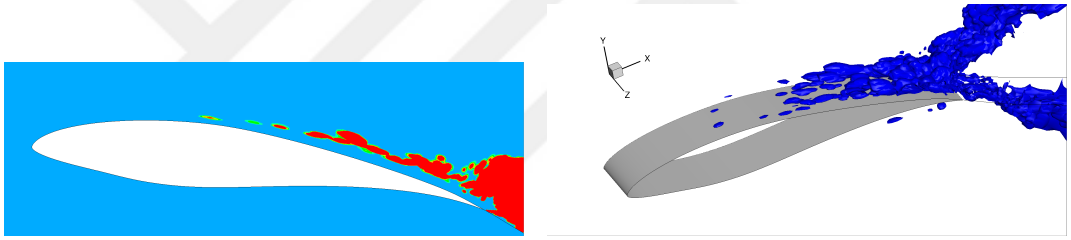
Comparing the friction coefficient profiles at AoA of 12° (see Figure 5.7b), DDES differs from DDES-SLA only for a fraction of the suction side after the transition. Hence, it would be beneficial to look at the vortical flow structures over the surface. Figure 5.10 shows the isosurfaces of Q-criterion colored by the eddy viscosity at an instant of time. In the DDES-SLA results, the vortical structures turn into 3-D fine turbulence immediately, whereas the DDES results mostly show somewhat 2-D behavior. These visuals support that the shear-layer-adapted length scale accelerates transition from the modeled (RANS) mode to the resolved (LES) mode of DDES, and acts more like LES. The contour levels signify that this acceleration is achieved by reducing the viscosity in the initial region of separation. As a result, DDES-SLA gives somewhat a closer C_d value to the measured value, although C_l values of both

DDES approaches look very similar.

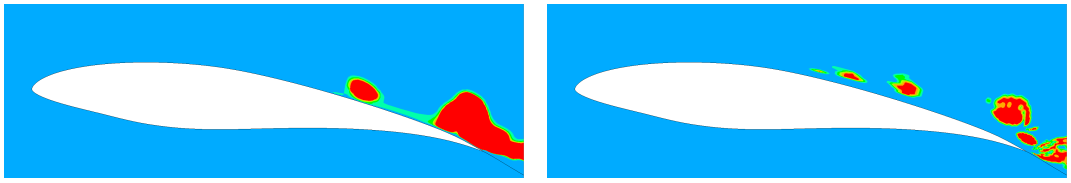


(a) DDES (b) DDES-SLA

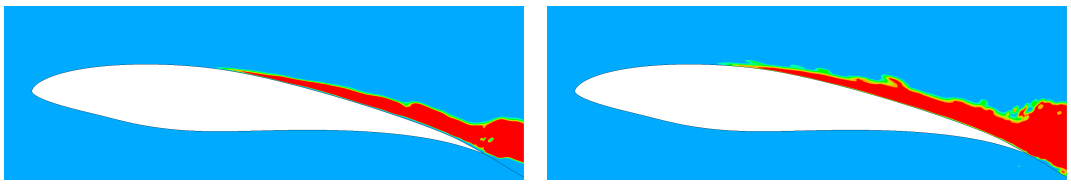
Figure 5.10: Isosurfaces of Q-criterion ($Q = 0$) colored by $\hat{\nu}_t/\nu$ around the blade at AoA of $12°$ via DDES and DDES-SLA (Re $= 100,000$)



(a) Term_1 contours (b) Term_1 isosurfaces



(c) Term_2 from the original model (d) γ_{BCM} from the original model



(e) Term_2 after modifications (f) γ_{BCM} after modifications

Figure 5.11: Transition model terms (red color: 30.0) and the intermittency function (red color: 1.0) around the blade surface at AoA of $10°$ (Re $= 100,000$)

Lastly in this section, the functions of the BCM model are presented at AoA of 10°. Figure 5.11 shows instantaneous contours of Term_1, Term_2, and γ_{BCM} variables. The same problem is solved by DDES-SLA-BCM using the original BCM model to compare with the current one involving modifications recently done to the model (see Section 2.2.1.1). As mentioned before, during solutions of unsteady problems Term_1 may not exist permanently along the downstream. This tackled case has strong unsteadiness such that nonzero Term_1 values disappear instantly at some points both in the spanwise and streamwise directions (see Figures 5.11a-b). This spoils the permanence of γ_{BCM} generation (and the eddy viscosity production) outside the boundary layer, as time advances. Consequently, Term_2 could not activate γ_{BCM} inside the downstream boundary layer, as shown in Figures 5.11c-d. Hereby, the proposed Term_3 as well as the modified version of Term_2 could trigger the intermittency function in the desired regions, as evident from Figures 5.11e-f.

5.1.2.3 Case 2: Reynolds number of 145,000

In this case, results for the Re_2 case are presented in the same manner as Section 5.1.2.2. Table 5.3 gives the aerodynamic coefficients for the three computed AoAs (8°, 10° and 12°) and compares with the benchmark studies including DDES and $k-\omega$ SST Transition of [8]. Apparently, the lift coefficient results of the AoA of 8° case are overpredicted by the current DDES approach when compared to the benchmark DDES study which has finer grid domain in the streamwise and normal directions. On the contrary, DDES-SLA with and without the transition model gives almost the same C_l value as the benchmark DDES. Therefore, this can be considered as an indication that DDES needs finer grids than DDES-SLA to capture the same C_l values. Similar statements can be made regarding the drag coefficient results. On the other hand, as AoA is increased, the current studies with DDES and DDES-SLA could not reveal a stall angle, unlike the other benchmark simulations. In addition, all current approaches overpredict the lift coefficients and underpredicted the drag coefficients when compared to the benchmark ones. This can be explained by the grid resolution as well as the span width differences. Nevertheless, DDES-SLA gives closer results than DDES.

Table 5.3: Comparison of lift and drag coefficients of the blade section

	AoA of 8°		AoA of 10°		AoA of 12°	
	C_l	C_d	C_l	C_d	C_l	C_d
DDES	1.446	0.0318	1.559	0.0404	1.6982	0.0524
DDES-SLA	1.378	0.0332	1.509	0.0415	1.604	0.0578
DDES-SLA-BCM3	1.380	0.0270	1.505	0.0340	1.530	0.0605
DDES [8]	1.355	0.0284	1.374	0.0456	1.315	0.0744
$k-\omega$ SST Transition [8]	1.202	0.0281	1.322	0.0472	1.343	0.0672

When the transition model is involved into DDES-SLA, closer C_l and C_d values to the benchmark values are observed at AoA of 12°, as shown in Table 5.3. The same results also indicate a stall behavior after AoA of 10°. However, stall starts at AoA of 8° in the benchmark simulations, unlike DDES-SLA-BCM3. This can be related to the grid resolution difference as stated earlier. It should be noted here that the $k-\omega$ SST Transition simulation had the same fine grid domain as the DDES of the same study, but yielded the closest results to the experimental ones. Hence, considering both DDES-SLA-BCM3 and $k-\omega$ SST Transition simulations, use of transition models could be necessary in such low Reynolds number wing flows.

In order to examine the reason of observed discrepancies, pressure coefficient distributions on the surface and the streamlines over the blade are plotted in Figure 5.12 and Figure 5.13, comparing the results at AoAs of 8° and 12°, respectively. At AoA of 8°, whereas $k-\omega$ SST Transition simulation predicts a sudden C_p change around the middle of the upper surface, both standard DDES studies fail to capture it. This is also emphasized in the study of [8]. At this point, DDES-SLA and DDES-SLA-BCM3 results reveal a ripple, similar to those of the $k-\omega$ SST Transition. This is also noticeable in the streamlines, which can be related to the C_p distribution. The reason of this relation is that such ripples indicate a sudden velocity change of flow. This is obviously caused by a separation bubble since the surface inclination of the airfoil does not change abruptly at this point, and there is no compressibility effect to change the velocity as well. When Figure 5.12 is analyzed, the mentioned separation bubble is only observed in DDES-SLA among the methods without transition mod-

els. The explanation of the failure of DDES studies is that the flow does not involve a massively separated region, a well-known requirement for classical DES/DDES. On the other hand, success in DDES-SLA comes from the SLA subgrid length scale originally proposed for shear layer separations. The findings show that DDES with the SLA length scale has a potential to simulate slightly separated flows. Note that the location of this bubble is not exactly the same as in the $k-\omega$ SST Transition simulation. This is expected due to the lack of a transition model. DDES-SLA-BCM3, on the other hand, not only captures the beginning of the ripple, but also computes the upstream region better than DDES and DDES-SLA, thanks to the BCM transition model. Considering the ripple onset together with the eddy viscosity levels to be shown below in Figures 5.14a-b infers that this ripple is a laminar separation bubble that induces the transition.

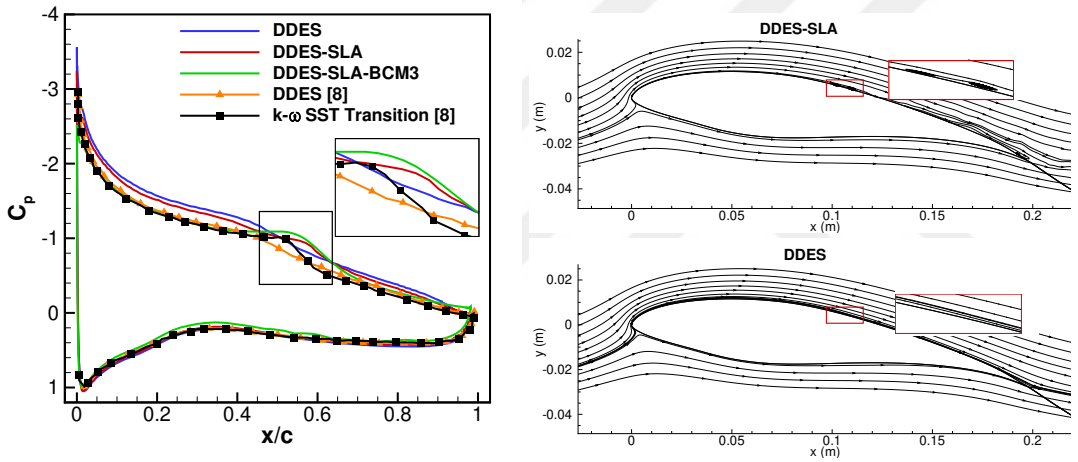


Figure 5.12: C_p distributions over the surface (left) and the streamlines around the blade (right) at AoA of 8° (Re $= 145,000$)

The results of the AoA of 12° case in Figure5.13 show that although C_p distributions do not reveal much difference among all numerical studies, a small ripple near the leading edge is only seen in the $k-\omega$ SST Transition one. This time, DDES-SLA-BCM3 fails to predict the ripple as well, which may indicate an insufficient grid resolution along the streamwise direction.

Figure 5.14 demonstrates isosurfaces of Q-criterion around the blade at AoAs of 8° and 12°. Likewise in the case of Re_1, at both AoAs DDES-SLA reveals more 3-D structures than DDES. In other words, the structures appearing in the DDES results

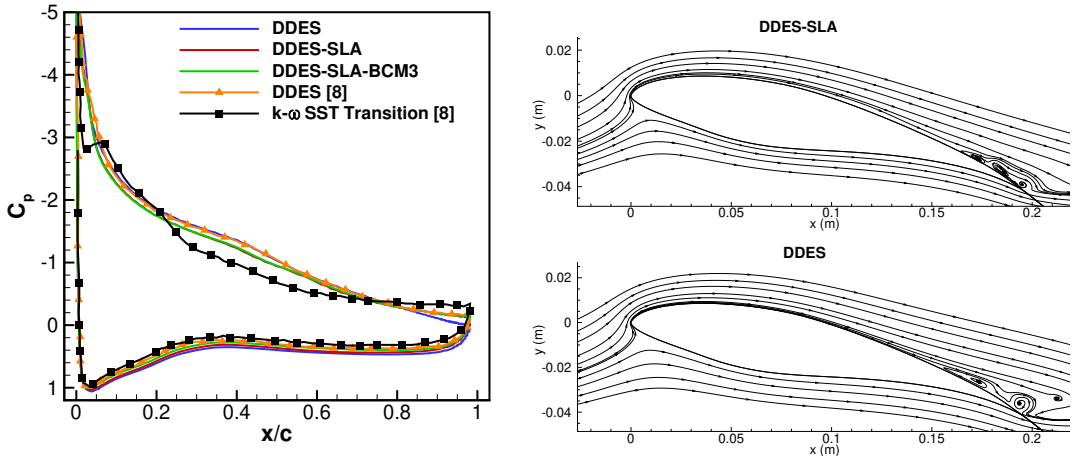
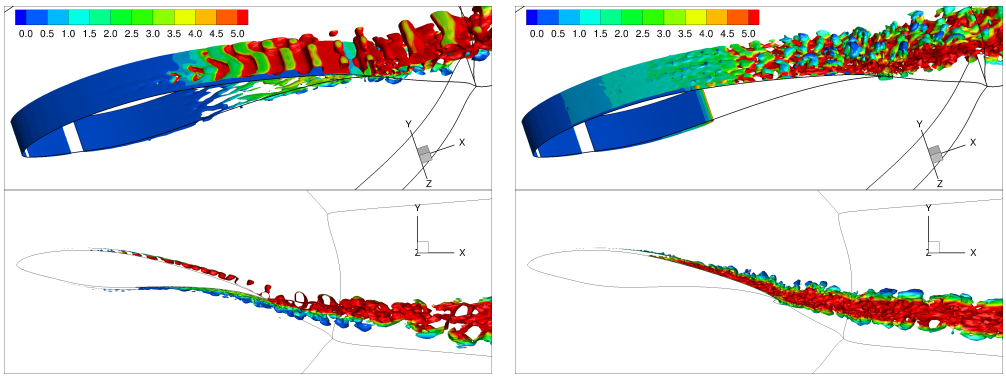


Figure 5.13: C_p distributions over the surface (left) and the streamlines around the blade (right) at AoA of $12°$ (Re $= 145,000$)

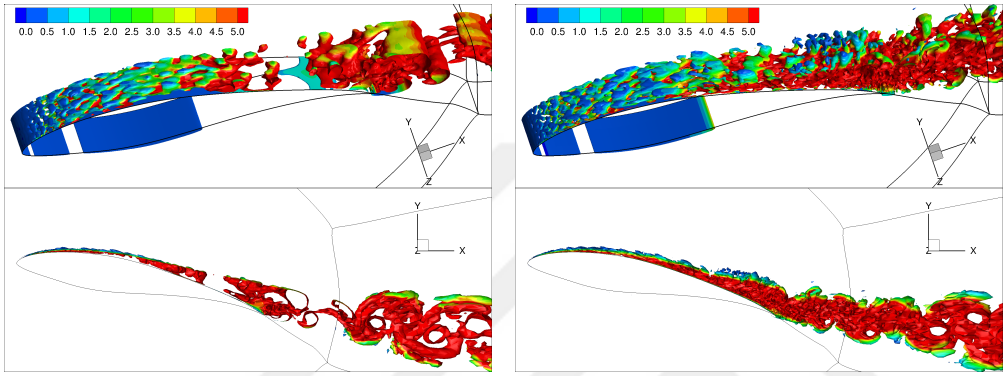
are formed of mostly 2-D big vortices whereas DDES-SLA obviously seems to provide the transition of the LES mode earlier. In addition, at AoA of $8°$, DDES reveals vortical structures on the pressure side, in contrast to DDES-SLA. In fact, those structures should not be generated on the pressure side. The reason of this behavior is not known although overcoming is simply taking a little higher initial $\hat{\nu}_t$ value. Another important observations from DDES-SLA isosurfaces at AoA of $8°$ is the structures firstly appear just outside the boundary layer edge, and then in a short distance they cover all over the near wall regions, as evident in Figure 5.14b. This may indicate the presence of the Kelvin-Helmholtz (K-H) instabilities, detected by the SLA sensors. These are the primary instabilities triggering separation-induced transition. Here, unlike DDES, DDES-SLA unlocks the instabilities, and makes the downstream region completely 3-D. This can explain the superiority of DDES-SLA over DDES in predicting aerodynamic coefficients.

Figure 5.15 demonstrates the ratio of the eddy related viscosity ($\hat{\nu}_t$) to the molecular viscosity (ν) around the blade given by the current simulations. It is evident that the SLA subgrid length scale reduces the eddy viscosity to increase the LES content, as is already stated in the previous case (Re_1). This is related directly to the emergence of 3-D structures shown in Figure 5.14. DDES-SLA-BCM3, on the other hand, maintains the leading edge (indicated by a rectangle in Figure 5.15) and the pressure side fully laminar whereas DDES-SLA generates some eddy viscosity there. The BCM



(a) AoA of $8°$ via DDES

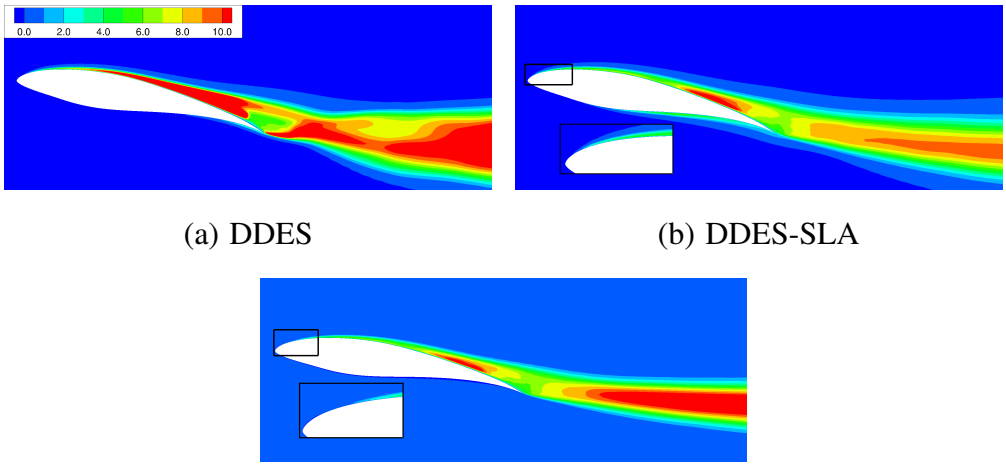
(b) AoA of $8°$ via DDES-SLA



(c) AoA of $12°$ via DDES

(d) AoA of $12°$ via DDES-SLA

Figure 5.14: Isosurfaces of Q-criterion ($Q = 0$) colored by $\hat{\nu}_t/\nu$ around the blade at AoAs of $8°$ and $12°$ via DDES and DDES-SLA ($\mathrm{Re} = 145,000$)



(a) DDES

(b) DDES-SLA

(c) DDES-SLA-BCM3

Figure 5.15: $\hat{\nu}_t/\nu$ contours of mean flow fields at AoA of $12°$ ($\mathrm{Re} = 145,000$)

model enhances the aerodynamic performance in this way.

One may notice that simulating both the pre- and post-transition regions accurately is vital for this type of flow problems. In this regard, DDES-SLA-BCM3 gives plausible results by blending the SLA length scale and the BCM model. It should be pointed out again that the BCM transition model captures the transition onset without solving any additional differential equations.

5.2 Flow over a Circular Cylinder

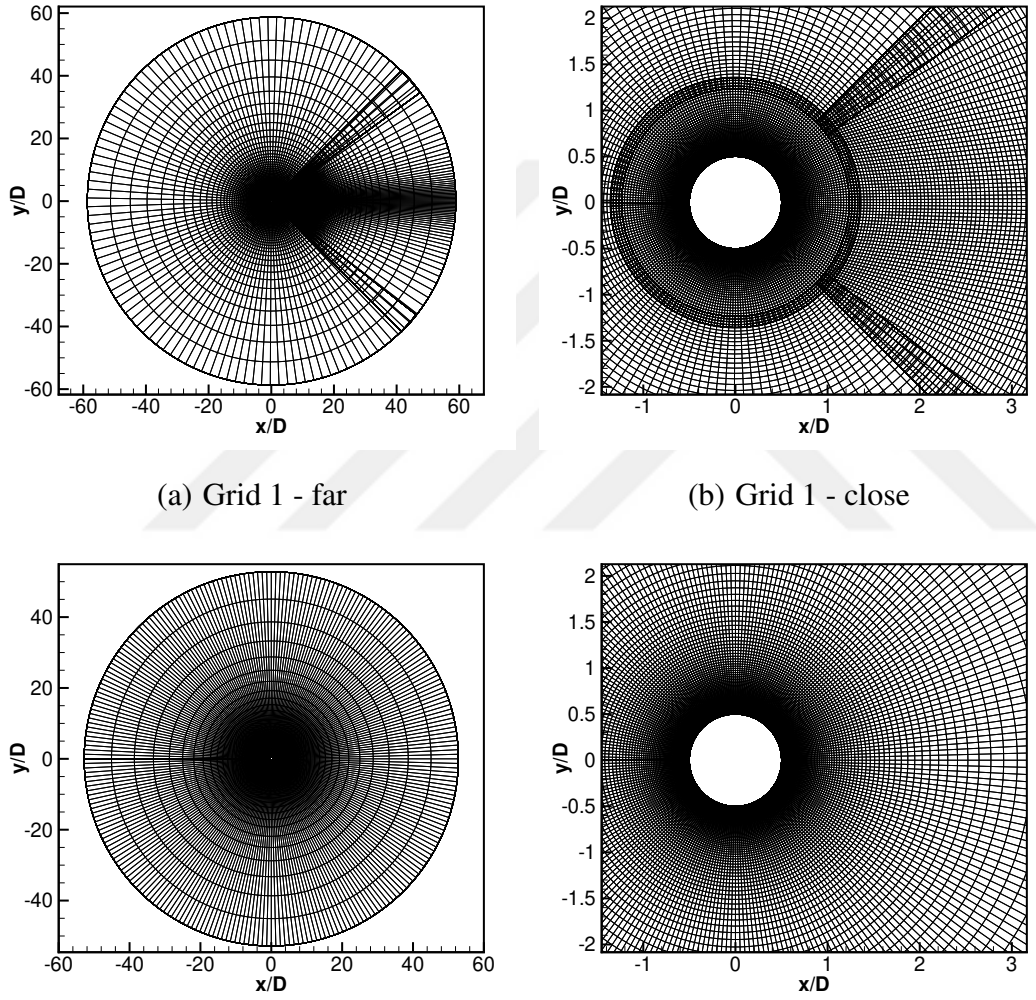
Flow over a circular cylinder is a difficult problem for DDES because different flow regimes are involved in a way that a Reynolds number (Re) increment yields a drag crisis, namely a sudden decrease in drag, after a certain point. The aim of this study is to compare the prediction capabilities of different frameworks based on URANS[2], DDES, DDES-SLA, DDES-BCM, and DDES-SLA-BCM3. In this regard, flow with a Mach number of 0.1 is simulated at various Reynolds numbers (Re of $10^4, 10^5, 5.0 \times 10^5$ and 10^6).

5.2.1 Grid Generation and Boundary Conditions

An O-grid is generated around the 2-D circle and then extruded with a uniform spacing, Δ_z, in the spanwise direction. The mesh generation parameter details are given in Section 3.1. Wake resolution is quite important in this problem as large vortices emanating from an unsteady separation from a blunt body are shed along the wake in a repeating pattern (Kármán vortex street). Thus, in the mesh generation procedure in the $x - y$ plane, the cylinder wake is divided into three regions as suggested by [111] (D: diameter of the cylinder): Viscous ($0.5D - 1.5D$), Focus ($1.5D - 15.0D$), and Euler Regions ($15.0D - 50.0D$). Viscous and Focus Regions are the zones where turbulent structures are resolved directly by the LES mode; therefore, Δ_{max} ($= \Delta_z$) is kept constant there. Δ_z equals to $0.03125D$ considering [111]. For grid dependency analysis, an additional grid is examined having different $\Delta_{max} = 2\Delta_z$ (see Table 5.4 for Grid 1 and Grid 2). Changing the span length is also studied, using the same grid

[2] URANS results are included to show a superiority of DDES.

resolution as in Grid 2. $0.5D$, $1.0D$, and $1.5D$ values are selected for this purpose, referring to as Grid 2, Grid 3, and Grid 4, respectively. Close and far views of the two grids having different resolutions in the wake region are shown in Figure 5.16. Grid 2 is a single block domain whereas Grid 1 is composed of three blocks (see Figure 5.16b) that are communicated by 3rd-order overset technique in the overlapping regions. Once again, boundary conditions can be found in Table 3.1.



(a) Grid 1 - far

(b) Grid 1 - close

(c) Grid 2 - far

(d) Grid 2 - close

Figure 5.16: Close and far views of two grids having different wake resolutions over a cylinder

5.2.2 Results and Discussion

Parallel simulations are performed using multiprocessors, the number of which varies from 32 to 64. Δt^* is equal to 5×10^{-1}, which is rather big comparing to the previous problems since the field is dominated by large eddies. Mean flow values are obtained by averaging the unsteady flow data gathered for 300 nondimensional time after 100 nondimensional time has passed.

5.2.2.1 Grid Dependency Analysis

Grid dependency study is performed at the largest Reynolds number, which is 10^6. Table 5.4 shows some grid parameters with separation angles and drag coefficients obtained by DDES. The values of the benchmark study that employed DDES with $\gamma - Re_\theta$ transition model [107] based on $k-\omega$ SST eddy viscosity equations are also included to make comparison. It is shown that the wake resolution of Grid 2 is sufficient to predict aerodynamic values. On the other hand, when the wake resolution is kept constant, it is observed that at least $1.0D$ span length is necessary. Hence, the rest of the simulations are performed on Grid 3. Note that Δ_z that is twice the benchmark one is not examined in the grid dependency study. This is to demonstrate the superiority of DDES-SLA over DDES as the SLA length scale is less dependent on the spanwise grid spacing (recall Section 2.1.3.4). Lastly, the total cell number is much lower than the benchmark one. It should be emphasized that the benchmark simulations are performed employing the EllipSys3D code which is 2nd-order in space and time, whereas the current computations are carried out by a high-order code.

5.2.2.2 Simulations

In this section the attained mean flow fields are compared with those given by DDES with and without $\gamma - Re_\theta$ transition model presented in [107], as well as experimental data of [123, 27]. In the present computations the turbulent intensity is taken as 0.13 just as in the benchmark studies. This parameter is used only for the Term_1 calculations in DDES-BCM and DDES-SLA-BCM3. It should be noted that unlike the previous problems, the original BCM model used for DDES-BCM provides a

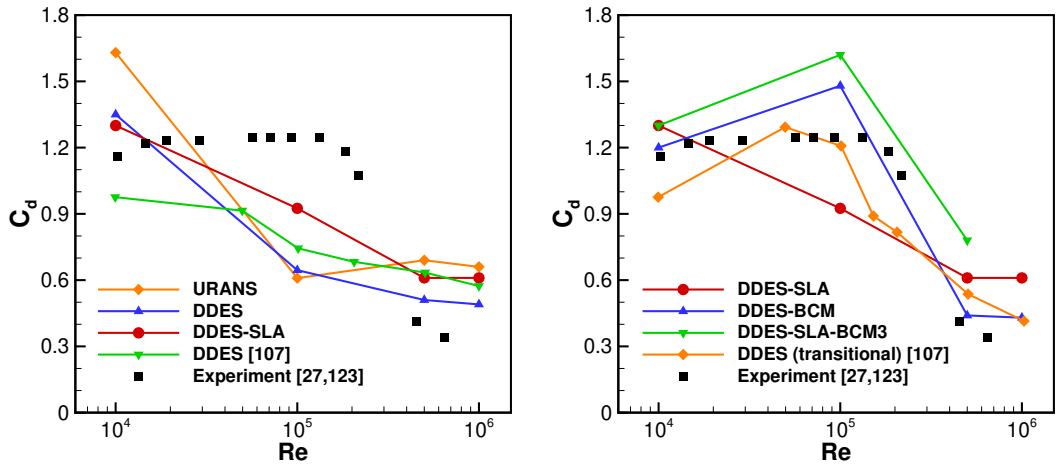
Table 5.4: Grid dependency study for cylinder flow

	Grid 1	Grid 2	Grid 3	Grid 4	DDES [107]
Δ_z	0.03125D	0.03125D	0.03125D	0.03125D	0.0156D
Δ_{max}	0.03125D	0.06250D	0.06250D	0.06250D	-
span length	0.5D	0.5D	1.0D	1.5D	2.0D
total # of cells	0.82×10^6	0.69×10^6	1.37×10^6	2.1×10^6	8.4×10^6
C_d	0.60	0.59	0.49	0.47	0.42
θ_{sep}	112.5	110.7	106.9	106.3	109.6

permanent intermittency function over the surface in this problem since the time and length scales are big enough. Therefore, the results of DDES-BCM are included as well.

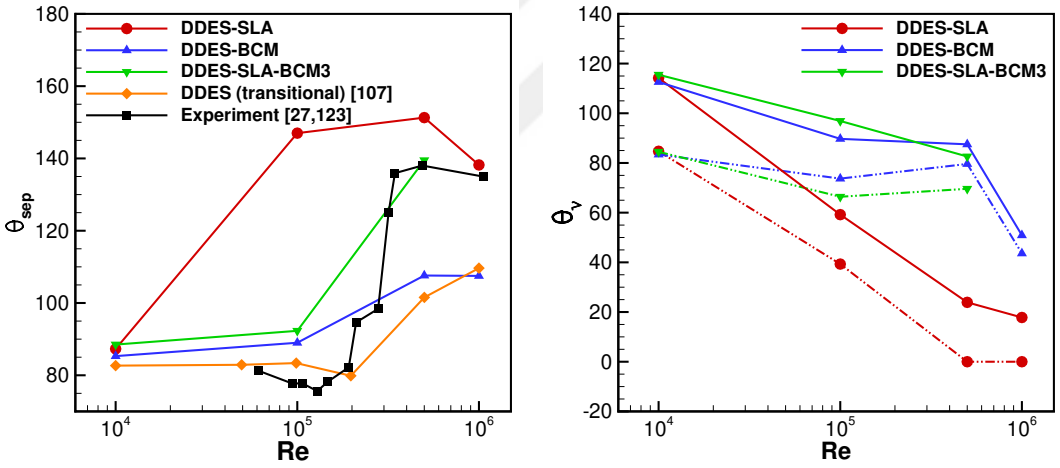
First, the drag coefficient values, computed from the averaged flow field, are given in Figure 5.17. All referenced data are included for comparison. For clear visualization, the results are divided into two groups. The drag crisis can clearly be seen in the measured data after Re of 2×10^5. Before this, the drag values appear to be almost constant except at Re of 10^4. It is evident from Figure 5.17a that the trend of the measurements is not predicted by the simulations without a transition model. In addition, the DDES and DDES-SLA simulations show a constant decrease whereas URANS computations are of a total failure. This indicates that all the DDES approaches appear to have performed much better than URANS at each Reynolds number, as expected. The present DDES results are in fair agreement with the benchmark DDES ones, yielding that the grid resolution can be considered sufficient. Moreover, among the methods without transition models, DDES-SLA gives the closest results to the benchmark ones. On the other side, in Figure 5.17b, the drag crisis can be observed by the simulations using a transition model. Interestingly, the DDES-SLA-BCM results are in more agreement with the benchmark transitional DDES and the experiment results than the DDES-SLA-BCM3 ones.

The onset angles of wake separation (θ_{sep}, starting from the stagnation point) are shown in Figure 5.18a. Here, wake separation means flow separation that results in a wake. Figure 5.18b, on the other side, presents the angles at which the eddy viscosity



(a) Group 1 (b) Group 2

Figure 5.17: Comparison of drag coefficients of the cylinder flow for different Reynolds numbers. For clear visualization, the results are divided into two groups.



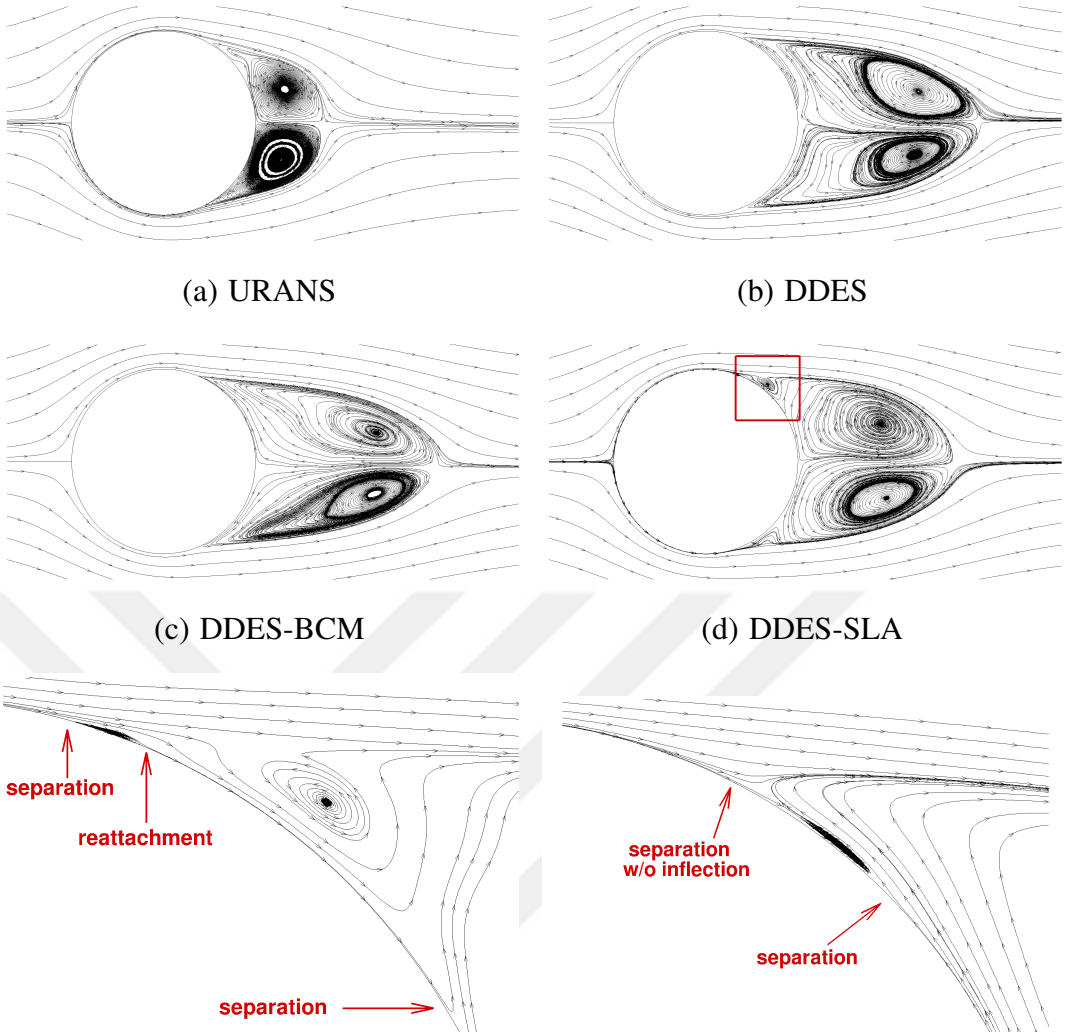
(a) Wake separation (b) $\hat{\nu}_t/\nu$

Figure 5.18: The onset angles of the flow separation forming wake as well as certain eddy viscosity values (dashed dot: $\hat{\nu}_t/\nu = 0.001$, solid: $\hat{\nu}_t/\nu = 5.0$) for different Reynolds numbers

reaches some certain values. Each solid line in this figure represents the first appearance of fully turbulent flow. Note that both figures include only the DDES-SLA, DDES-BCM, and DDES-SLA-BCM3 results from the current studies since they pre-

dict more accurate C_d values than the others. At Re of 10^4, laminar flow separates just before the angle of $90°$, and then forms wake without reattachment on the surface, supported by Figure 5.20a. The flow becomes turbulent around the angle of $120°$ as shown in Figure 5.18b. This behavior can be observed in all numerical studies. As Re increases up to the critical point ($\text{Re}_{\text{critical}} \approx 2 \times 10^5$), laminar-to-turbulent transition is not expected before the wake separation. Besides, according to the experiment and the transitional DDES study from literature, flow keeps separating around the same region up to $\text{Re}_{\text{critical}}$. Re of 10^5 results from the current simulations except DDES-SLA also follow this trend. When looking at both Figure 5.18a and Figure 5.18b, DDES-BCM and DDES-SLA-BCM3 exhibit a transition to turbulent flow downstream from the separation point, as desired. This is achieved by suppressing the turbulence production until transition criteria are met, thanks to the BCM model. DDES-SLA, on the other hand, shows a late separation considerably at the corresponding Reynolds number. In fact, a reattachment is observed in DDES-SLA, retarding the wake separation. Figure 5.20b can support this observation. This results in an early drag crisis, which is compatible with the C_d results of DDES-SLA (see Figure 5.17).

The reason for the sudden increase of θ_{sep} after the critical Reynolds number, as observed in the measurements, can be attributed to that the separated laminar flow turns into turbulent rapidly such that it reattaches to the surface, followed by a wake separation downstream. This behavior is exhibited only when using the SLA subgrid length scale (at Re of 5.0×10^5), resulting in a good agreement with the experiment in estimating θ_{sep}. The delay of wake separation revealed by the SLA length scale can be seen in Figure 5.19, which shows streamlines over the cylinder. Figure 5.19e, a close view of the red spot in Figure 5.19d, shows the initial separation, reattachment, and the second separation obtained by DDES-SLA. The reattachment part reduces the pressure drag caused by the wake. Although the skin friction increases due to turbulent boundary layer, the drag coefficient is reduced in total. Hence, the drag crisis phenomena occurs. The same spot is plotted for DDES-SLA-BCM3 as well (see Figure 5.19f). It should be noted that in the DDES-SLA-BCM3 results the first separation point is not an inflection point on the wall. Instead, that point is the starting point of a reverse flow inside the boundary layer. Unlike the others, the separated flow is revealed without an inflection point, which is not physical. This indicates an in-



(a) URANS (b) DDES

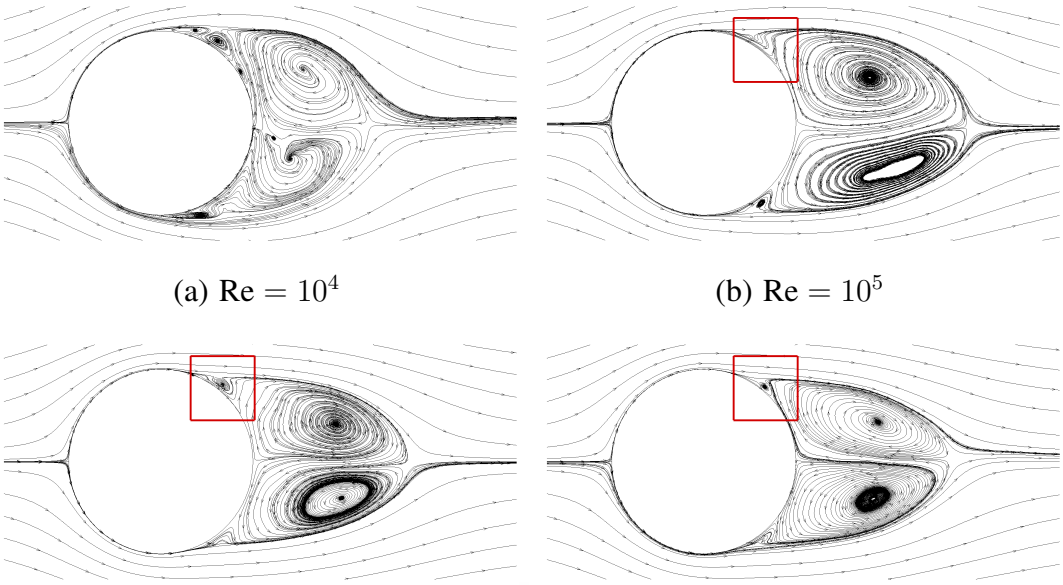
(c) DDES-BCM (d) DDES-SLA

(e) DDES-SLA (close view) (f) DDES-SLA-BCM3 (close view)

Figure 5.19: Averaged streamlines over the cylinder obtained by different methods (Re $= 5.0 \times 10^5$)

compatibility between SLA and BCM3 for this problem. This might be the reason for the differences observed in the C_d values. On the contrary, methods without SLA do not show any reattachment at all, as evident from Figures 5.19a-c at Re of 5.0×10^5. Lastly, at Re of 10^6, θ_{sep} is predicted more accurately by SLA again. It seems that an increment of the eddy resolution by rapid switching to the LES mode helps capturing flow reattachment.

In addition to the results from Figure 5.18, in DDES-SLA, the eddy viscosity reaches a fully turbulent value significantly earlier than the wake separation onset for the



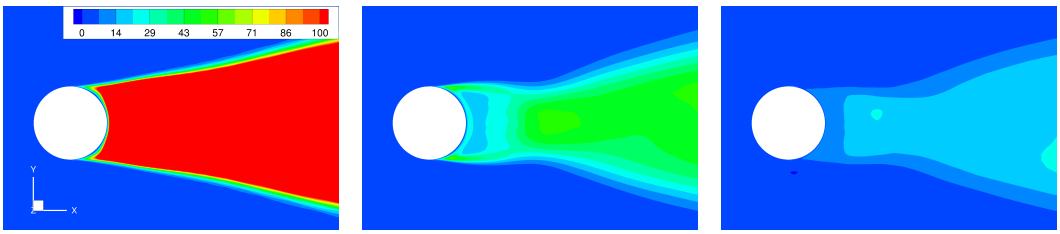
(a) Re $= 10^4$ (b) Re $= 10^5$

(c) Re $= 5.0 \times 10^5$ (d) Re $= 10^6$

Figure 5.20: Averaged streamlines over the cylinder obtained by DDES-SLA for different Reynolds numbers

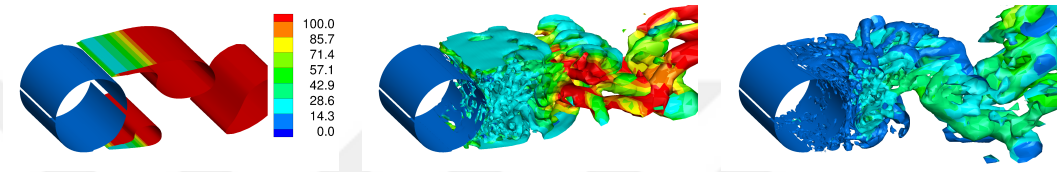
last two Reynolds numbers. However, DDES-SLA can exhibit a separation bubble although the incoming flow is turbulent (compare Figures 5.18b and 5.19e). The reason is when SLA detects the K-H instabilities, it reduces the eddy viscosity, and thereby causing the separation. Nevertheless, the success of the simulation methods with the BCM transition model in estimating drag force is achieved by suppressing the eddy viscosity production until separation. It should be emphasized that the BCM model is much cheaper than the other transition model used in the benchmark study. The $k - \omega - \gamma - Re_\theta$ approach involves solving 9 equations in total. Therefore, it is estimated up to 33% increased efficiency of the solution algorithm when BCM based on the S-A one equation is used instead (6 PDEs against 9).

Time-averaged streamlines over the cylinder are shown in Figure 5.19 and Figure 5.20. In the first figure, it is seen that URANS creates narrower wake as compared to the others at the same Re. DDES and DDES-BCM exhibit similar wake shapes whereas DDES-SLA reveals two separation zones as spotted in red rectangle, which is already discussed. On the other hand, Figure 5.20 shows the change of the wake shape as Re increases via DDES-SLA. It is observed that the turbulent flow separations yield



(a) URANS (b) DDES (c) DDES-SLA

Figure 5.21: Mean eddy viscosity ($\hat{\nu}_t/\nu$) contours obtained by different methods (Re $= 10^5$)



(a) URANS (b) DDES (c) DDES-SLA

Figure 5.22: Instantaneous isosurfaces of Q-criterion colored by eddy viscosity levels ($\hat{\nu}_t/\nu$) obtained by different methods ($Q = 10^3$, Re $= 10^5$)



(a) URANS (b) DDES (c) DDES-SLA

Figure 5.23: Instantaneous vorticity contours at wake region obtained by different methods (Re $= 10^6$)

wider wake regions than the laminar one as in the Re of 10^4 case.

The effect of eddy viscosity levels on the flow resolution can be seen in Figures 5.21, 5.22, and 5.23 showing mean eddy viscosity contours, instantaneous Q-criterion levels, and instantaneous vorticity contours over the cylinder, respectively. It appears that URANS yields larger eddy viscosity values in the wake region because the ed-

dies are modeled everywhere. This causes the turbulent structures to appear as completely 2-D. On the contrary, DDES can reveal 3-D contents by resolving the eddies in the wake region. Use of SLA, on the other hand, accelerates the activation of the eddy-resolving mode so that 3-D structures suddenly appear after flow separation, unlike DDES. The reduction of eddy viscosity at flow separation onset provides this, as already discussed. Vorticity snapshots support these conclusions.

5.3 Transonic Flow over an Open Cavity

This section presents the computations of a transonic open cavity flow and the noise produced. Mach number and Reynolds number are set to 0.85 and 6.75×10^6, respectively. Simulations are performed through DDES, DDES-SLA, and IDDES-SLA. In this problem, flow is fully turbulent before it goes over the cavity geometry; hence, no transition model is used.

5.3.1 Configurations and Setups

5.3.1.1 Geometry and Boundary Conditions

The investigated flow configuration is an open cavity with a length-to-depth ratio (L/D) of 5. This configuration matches that of the widely studied M219 case, and hence the computed results could be compared to the available M219 data.

The computational domain is formed of two structured mesh blocks, one covering the inside of the cavity, and the other outside of it. Two different configurations are handled, called as Configurations 1 and 2. Configuration 1 represents the classical M219 case that has 5 solid walls inside the cavity. On the other side, Configuration 2 has no physical lateral solid walls, and thereby having only 3 solid walls inside the cavity. Besides, Configuration 1 has wider span in the outer block than Configuration 2. The rest of the domain dimensions are the same in both configurations. A schematic of the computational domain with relevant dimensions and outer boundary conditions is shown in Figure 5.24 whereas the outer span differences between the configurations

can be seen in Figure 5.25. The dimensions are given as follows,

$$x_a/D = 45, \quad x_b/D = 5, \quad L/D = 5, \quad x_c/D = 177, \quad y/D = 35, \quad W_2/W = 8 \tag{5.1}$$

In Configuration 1, width-to-depth ratio (W/D) is 1 in the inner block while being 8 in the outer one. Riemann invariant based far field conditions are applied on the outer span faces. The inner walls are treated as no-slip walls. In Configuration 2, both mesh blocks, inside and outside the cavity, are set to have the same width. Periodic BC is applied on the lateral boundaries of the outer block. However, inside the cavity either periodic or slip wall conditions are enforced to avoid boundary layer resolutions such that the computational resource requirements are lowered, as compared to Configuration 1. The effects of this approach are evaluated using the lateral dimensions of $0.5D$, $1.0D$, and $1.5D$, while keeping the mesh resolution in that direction fixed. The rest of BCs, available in Section 3.2, are the same in both configurations.

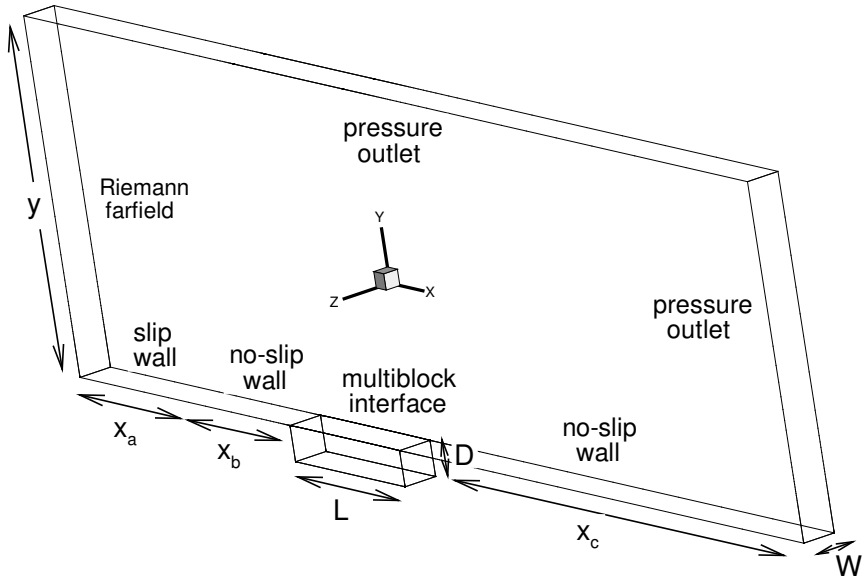


Figure 5.24: Schematic of Configuration 2 with boundary conditions

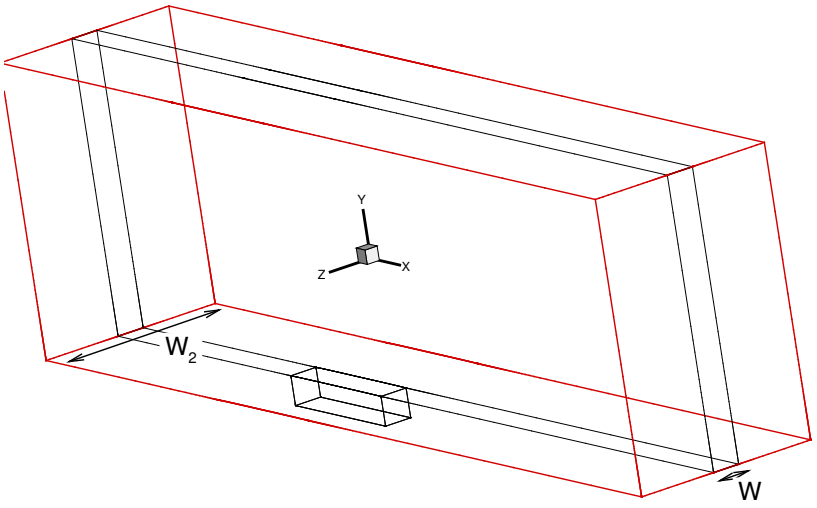


Figure 5.25: Comparison of outer span widths between two configurations. Red lines belong to Configuration 1.

5.3.1.2 Grid Generation

DES gridding strategies given in Section 3.1 are followed for both configurations. Near the walls, y^+ is taken as 1, leading the first cell distance away from all the walls to equal to a physical dimension of $2\times10^{-5}D$. The grid is stretched in the wall-normal direction with a ratio of 1.2 up to the boundary layer edges. In case of IDDES, in order to capture the WMLES region, which is the impingement zone occurring around the aft corner of the cavity, a stretching ratio of 1.14 would be a better choice as pointed out in Section 2.2.1.2. Nevertheless, it is commented out in [105] that 1.2 is also an acceptable growth rate. In a sense, over all the walls RANS boundary layer mesh is created. On the other hand, in the LES region inside the cavity, Δ_{max} is set to resolve the high frequency feedback mechanisms. In this context, two grids with different Δ_{max} values are generated for Configuration 2: $\Delta_{max,1} = 3 \times 10^{-2}D$ and $\Delta_{max,2} = 4.5 \times 10^{-2}D$. In the outer block, cells with Δ_{max} are maintained up to $1D$ length in the upward, y-direction from the cavity mouth, as well as up to $1D$ length downstream from the aft corner to ensure that the vortical structures originated along the shear layer and their impingement on the aft wall are resolved properly. The rest of the mesh in the $x-y$ plane is stretched rather rapidly, yielding some mesh damp-

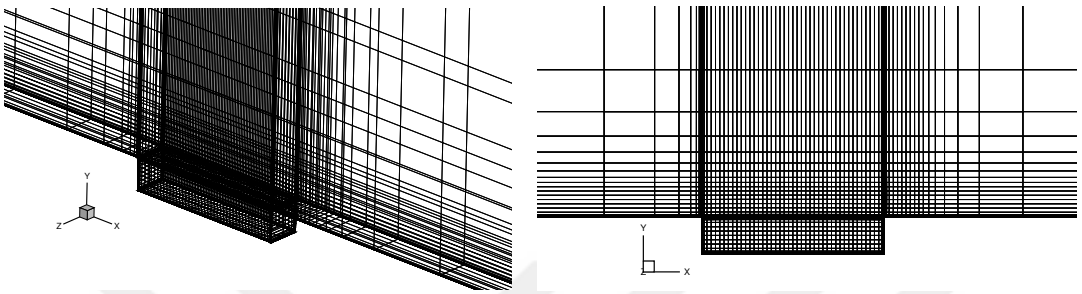
Table 5.5: The details of the cavity grids

Grids	y^+	W/D	Δ_{max}/D	total # of cells	spatial scheme
Grid A	~ 1	0.5	4.5 $\times 10^{-2}$	$\sim$ 0.5 million	4th-order DRP
Grid B	~ 1	1.0	4.5 $\times 10^{-2}$	$\sim$ 1.0 million	4th-order DRP
Grid C	~ 1	1.5	4.5 $\times 10^{-2}$	$\sim$ 1.5 million	4th-order DRP
Grid D	~ 1	1.0	3.0 $\times 10^{-2}$	$\sim$ 2.4 million	4th-order DRP
Grid E	~ 1	1.0	3.0 $\times 10^{-2}$	$\sim$ 13.3 million	4th-order DRP
LES [63]	wall model	1.0	3.0 $\times 10^{-3}$	$\sim$ 6.0 million	2nd-order
IDDES [69]	~ 1	1.0	1.5 $\times 10^{-2}$	$\sim$ 28.7 million	3rd-order Roe

ing eventually for non-reflective property along with the outer boundary conditions. In the spanwise direction, the grids that belong to Configuration 2 are extruded uniformly with a dimension of $\Delta_z = \Delta_{max}$ to have cubic cells. In Configuration 2, 4 different computational grids, denoted A, B, C, and D, having 2 different Δ_{max} values and 3 different lateral dimensions are used for studying their effects. Only one grid is created for Configuration 1, denoted E, which has the same 2-D grid topology in the $x - y$ plane as Grid D. In the spanwise direction in Grid E, the inner block is clustered through the lateral faces whereas it is extruded with a stretching ratio of 1.2 in the outer block from the cavity width edges to the far field boundaries. The details of the grids together with those of the benchmark studies from literature are tabulated in Table 5.5.

The results are compared with those of an LES study [63], an IDDES study [69], and measurements [45] from literature. As indicated in Table 5.5 all the employed grids of Configuration 2 in the present study are coarser than those of the benchmark cases. One reason is the present use of a higher order solver enabling of setting a larger maximum cell dimension in the LES region. Besides, there are lateral viscous walls inside the cavity in both the LES and IDDES studies in literature, and corresponding outer domains have wider spans. The present study aims to capture similar turbulent and acoustic environment without placing physical lateral walls, which gives the benefit of using less demanding grids. This approach, however, necessitates to investigate the effects of spanwise dimensions, and this is done in the present study. A close view

of Grid D is provided in Figure 5.26. On the other hand, Grid E which has the same configuration as those of the literature studies are inherently much finer than the other current grids. However, it is still coarser than the grid of benchmark IDDES study. In addition, the reason why the LES grid from literature has a lower cell number than Grid E can probably be explained by the use of the wall model near solid walls in the related study. Figure 5.27 demonstrates a close view of Grid E.



(a) 3-D view (b) 2-D view

Figure 5.26: Close views of Grid D showing one every four cells

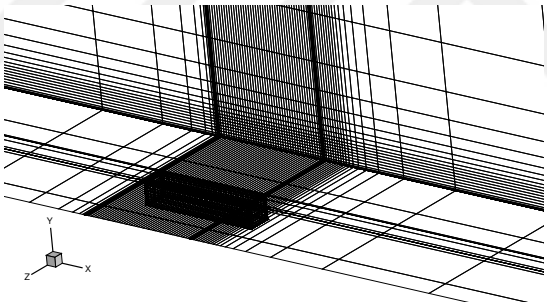


Figure 5.27: 3-D close view of Grid E showing one every four cells at IJK plane surfaces

5.3.2 Results and Discussion

The simulations that use Grids A-D are carried out using 112 cores, and for the one with Grid E, 280 cores are used. Since the effects of different grids and lateral BC options are evaluated in the study, for clarity all these subcases are summarized in Table 5.6, including some additional parameters. Δt^* is set to 1.25×10^{-3} for all the computations. This corresponds to a physical time step of 2×10^{-6} s. Data

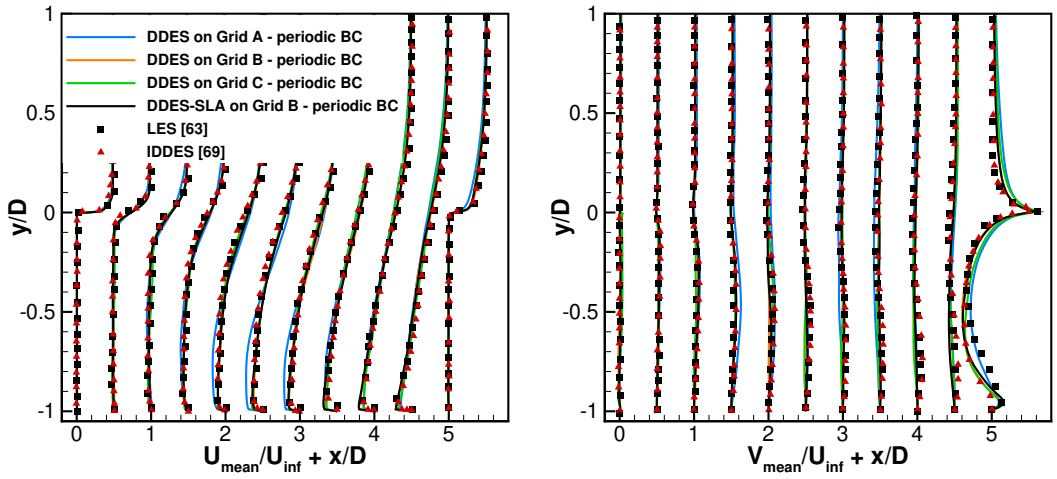
Table 5.6: The details of the transonic open cavity flow simulations

Methods	grid	inner lateral BC	$\Delta t_{\text{sampling}}$ (s)	T_{sampling} (s)
DDES	A, B, C	periodic	0.8 $\times 10^{-5}$	0.24
DDES-SLA	B, D	periodic, slip wall	0.8 $\times 10^{-5}$	0.2 - 0.32
IDDES-SLA	D	slip wall	0.8 $\times 10^{-5}$	0.32
IDDES-SLA	E	no-slip wall	-	-
LES [63]	-	viscous wall	1.0 $\times 10^{-5}$	0.5
IDDES [69]	-	viscous wall	1.8 $\times 10^{-5}$	0.295

sampling time step, $\Delta t_{\text{sampling}}$, is taken as 0.8×10^{-5} s, which is quite similar to those of the reference studies. Computed data is collected over physical durations, T_{sampling}, ranging from 0.2 s to 0.32 s. Note that Grid E could only be simulated until mean flow results are obtained. The computational resources of this dissertation is not enough to maintain the corresponding simulation to gather acoustic data. Therefore, the results of Grid E are presented only for mean flow fields.

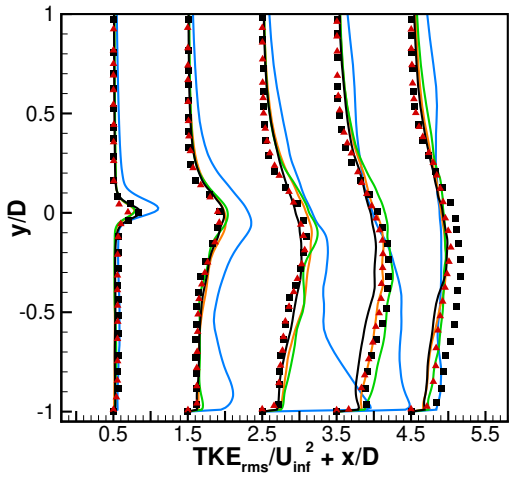
5.3.2.1 Mean Flow Fields

Mean flow quantities are obtained by temporal averaging of the whole field, which requires a physical time period of about 0.1 s. Turbulent kinetic energy (TKE) levels are extracted from the mean velocity field. About 500 instantaneous flow fields are sufficient to obtain statistically converged mean velocity and TKE profiles. The computed profiles along the cavity at the midspan plane from all the cases described in Table 5.6 are demonstrated in three separate figures for clear visualization. The reference LES and IDDES data are included in plots of all these figures for comparison. Figure 5.28 shows results computed by DDES on Grids A, B, and C as well as by DDES-SLA on Grid B. All the corresponding grids have lateral periodic BC. The results show that all the DDES approaches employed are capable of capturing the time-mean quantities around the cavity without lateral physical walls. Except for $W/D = 0.5$, the DDES results are not away from those of the reference studies, indicating the domain width should at least be equal to $1.0D$, in order to capture the mean flow characteristics



(a) Streamwise velocity

(b) Normalwise velocity



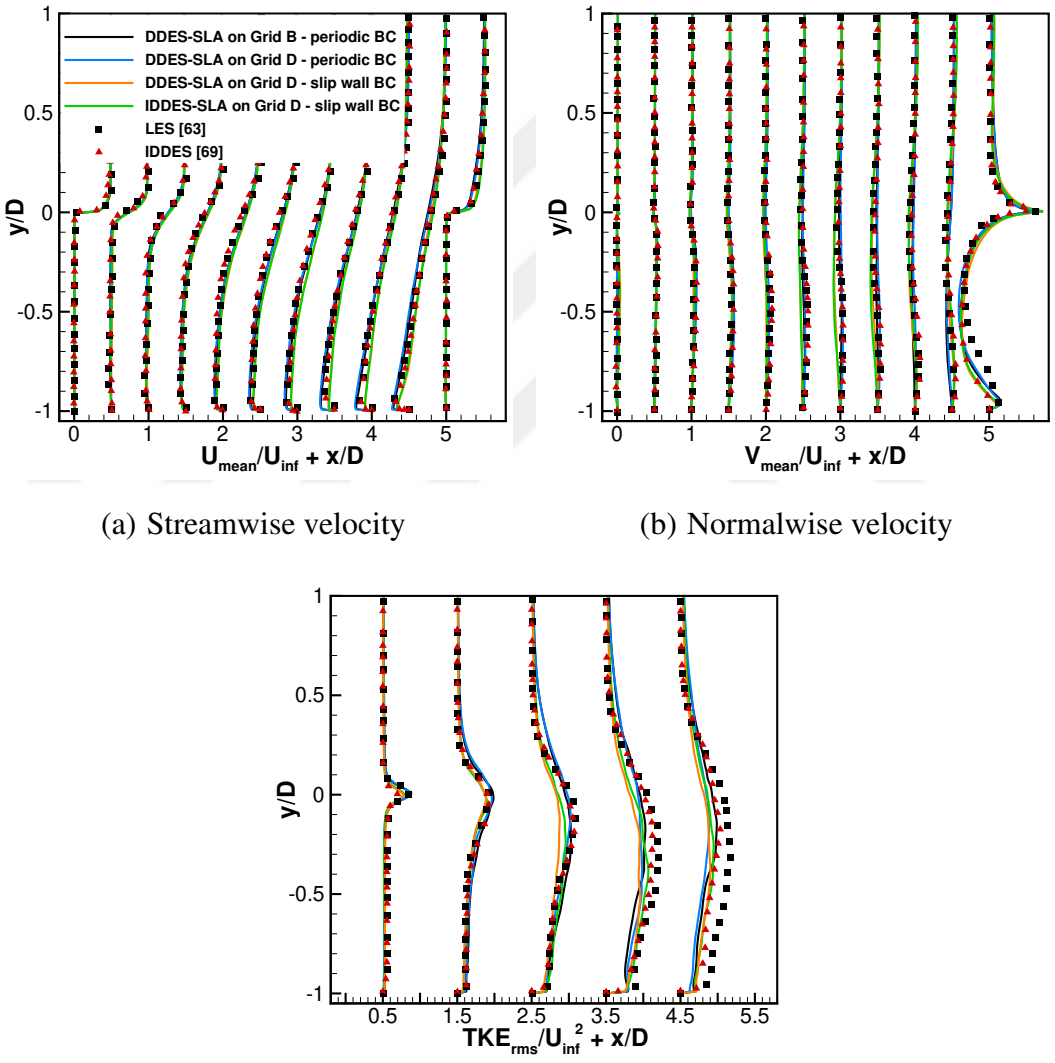
(c) TKE

Figure 5.28: Comparisons of mean flow velocity and TKE profiles along the cavity at middle of the span

observed in the M219 cavity problem. In addition, the present computations reveal in general quite similar flow profiles to the benchmark IDDES data, which deviate from the LES ones in the vicinity of the aft wall, especially for the normalwise velocity and TKE results (see Figures 5.28b-c). The current profiles appear to have larger deviations from the reference IDDES data, in comparison to LES. The only exception is the TKE profile at $x/D = 0.5$ where the DDES-SLA prediction is better than the benchmark IDDES, as indicated in Figure 5.28c. This improvement is achieved by accelerating transition to the LES mode using the SLA length scale. The corre-

sponding region is dominated by the K-H instability which is investigated in details later.

Figure 5.29 presents the profiles pertain to DDES-SLA and IDDES-SLA calculations on Grids B and D. This figure also compares the results from periodic and slip wall BC applications on the lateral boundaries inside the cavity. It is observed that there is no evidence that the fine grid (Grid D) improves the averaged quantities. Nevertheless, DDES-SLA and IDDES-SLA simulations with slip wall conditions on the lateral



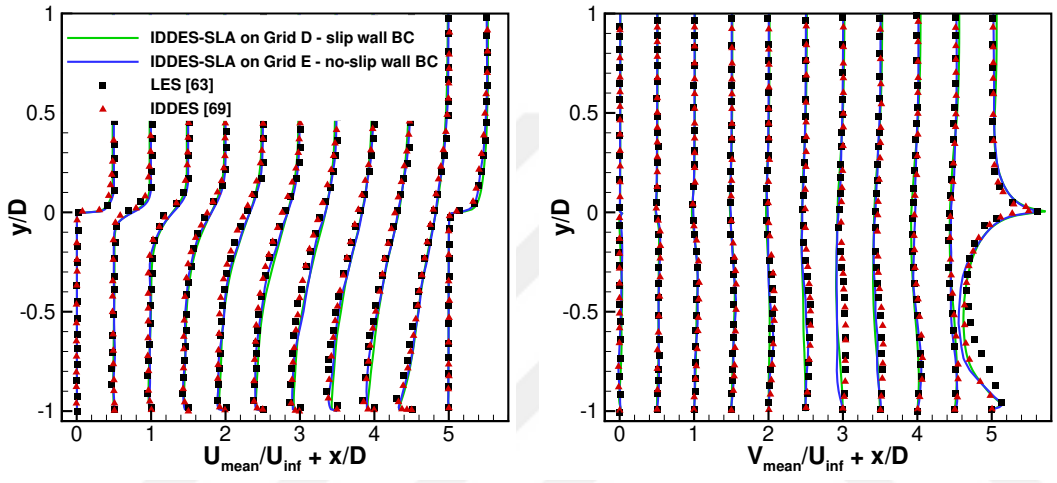
(a) Streamwise velocity

(b) Normalwise velocity

(c) TKE

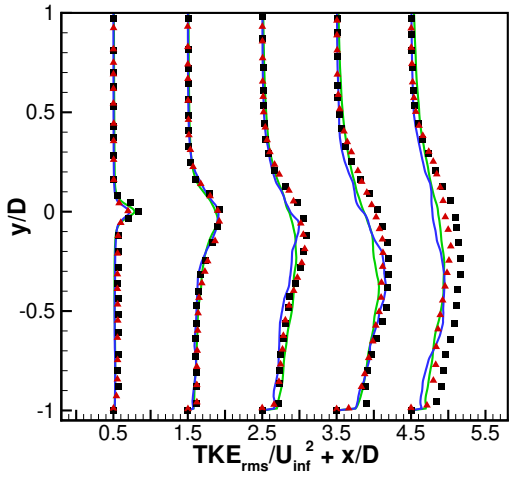
Figure 5.29: Comparisons of mean flow velocity and TKE profiles along the cavity at middle of the span

cavity boundaries are conducted on Grid D in order to resolve high frequency acoustic feedback. Applying slip wall condition there makes an improvement in capturing the gradients towards the aft wall even though the deviations in TKE profiles on the cavity mouth horizontal center plane are somewhat increased. The intersection of two different lateral BCs may be responsible for this effect. In addition, IDDES-SLA enhances the profile predictions around the aft wall in comparison to DDES-SLA. The former almost captures the benchmark IDDES velocity profiles in the corresponding region.



(a) Streamwise velocity

(b) Normalwise velocity

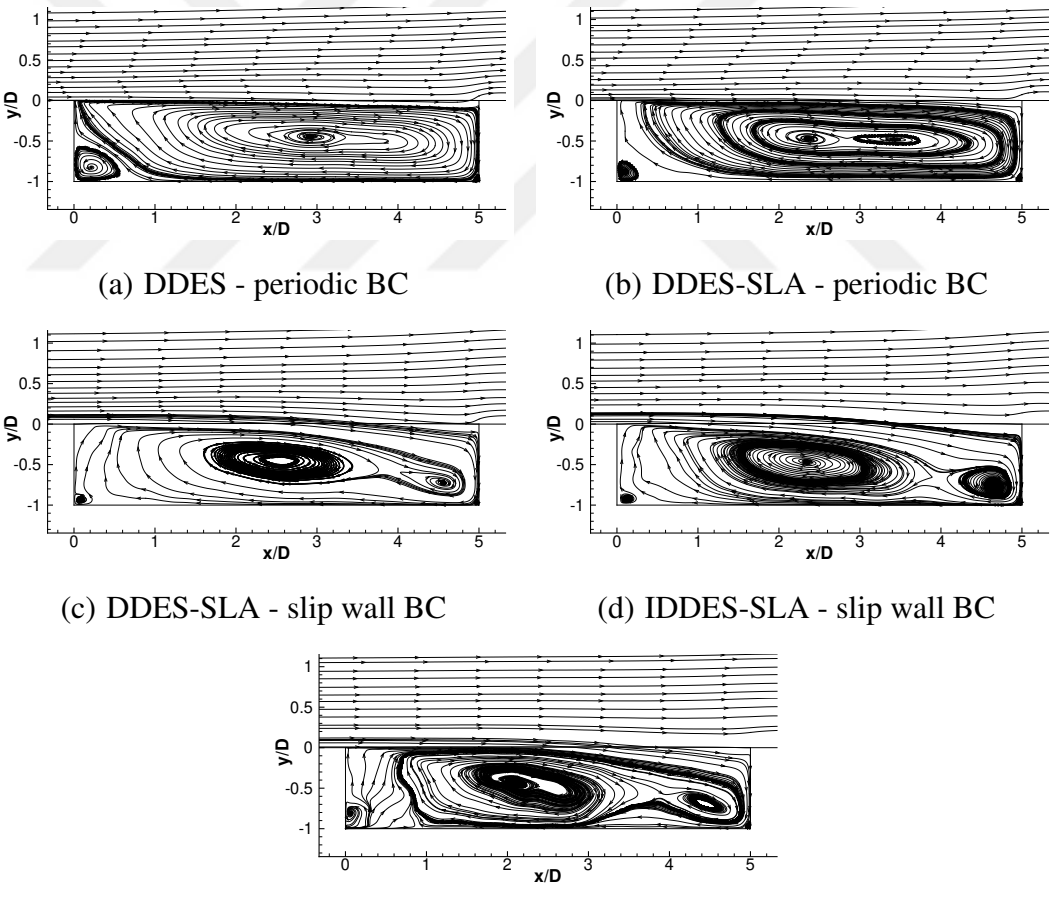


(c) TKE

Figure 5.30: Comparisons of mean flow velocity and TKE profiles along the cavity at middle of the span

On the other hand, Figure 5.30 includes IDDES-SLA results with slip wall (Grid D) and no-slip wall (Grid E) BCs, separately. Recall that Grid E is the only one that belong to Configuration 1, which has the same configuration as in the benchmark studies. Comparison of IDDES-SLA approaches on Grid D and Grid E shows that while use of actual M219 configuration improves the streamwise velocity profiles towards the aft wall, a slight enhancement is observed in capturing other profiles.

Figure 5.31 shows the streamlines associated with the mean flow fields obtained using the aforementioned DDES frameworks. In all the computed results, the separated flow seems to impinge on to the aft corner. This is the typical behavior of an open cavity flow. DDES appears to yield a large vortex with its center located at around $x/D = 3$, and two small vortices in the form of secondary flows near the corners.



(a) DDES - periodic BC

(b) DDES-SLA - periodic BC

(c) DDES-SLA - slip wall BC

(d) IDDES-SLA - slip wall BC

(e) IDDES-SLA - no-slip wall BC

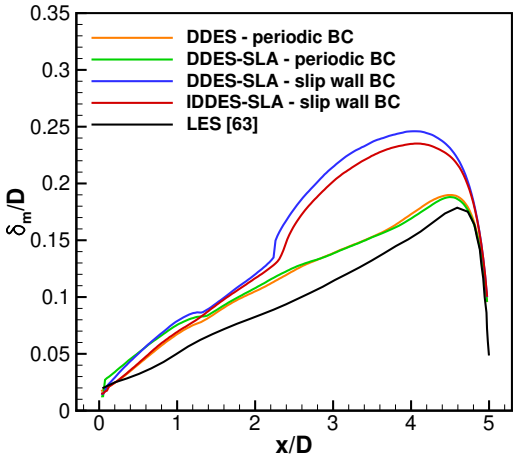
Figure 5.31: Streamlines of the mean flow fields at middle of the span

When SLA is activated, the vortex at the front corner becomes smaller in size and the large one gets focused around two centers, approximately at $x/D = 2.5$ and $x/D = 3.5$. Also, the lateral domain termination with the slip wall condition changes the vortex shapes considerably. The second center of the large zone shifts towards the small vortex at the back, which results in bending of the shear layer downward. This behavior is consistent with the previous graphs in which the velocity gradients have some differences through the aft wall when the lateral walls are treated as of the slip type. DDES-SLA and IDDES-SLA results with the slip wall BC exhibit similar vortex shapes. The locations of the vortex centers are the only observable discrepancies in these figures. Streamlines shown in Figure 5.31e are the only ones computed from Configuration 1, which has lateral solid walls inside the cavity. These streamlines, which are also compatible with the findings in the study of [86], are very similar to those with slip wall BC, particularly in the vicinity of the aft wall. Limiting the spanwise flow velocity by an inviscid wall seems to help the frameworks capture midspan flow fields of the actual M219 configuration. However, near the front corner IDDES-SLA with no-slip wall BC exhibits larger corner vortex than the one with slip wall BC.

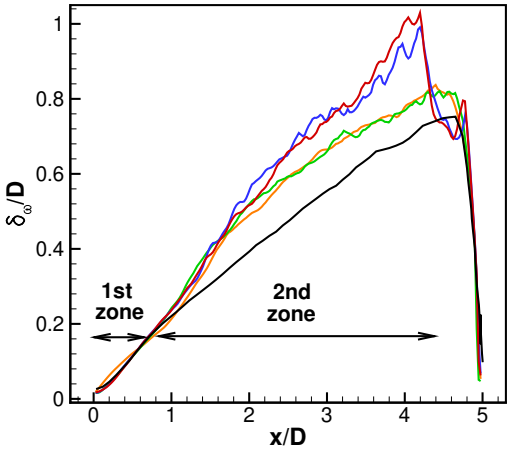
Before analyzing the acoustic results, the characteristics of the computed time-mean shear layers are discussed since they have an impact on the cavity acoustic field. In this regard, momentum and vorticity thicknesses (δ_m and δ_ω) are calculated as follows,

$$\begin{aligned} \delta_m(x,z) &= \int_{y_0(x,z)}^{+\infty} \frac{\bar{u}_1(x,y,z)}{U_\infty}\left(1-\frac{\bar{u}_1(x,y,z)}{U_\infty}\right)dy, \\ \delta_\omega(x,z) &= \frac{U_\infty}{\max\left(\dfrac{\partial \bar{u}_1(x,y,z)}{\partial y}\right)} \end{aligned} \tag{5.2}$$

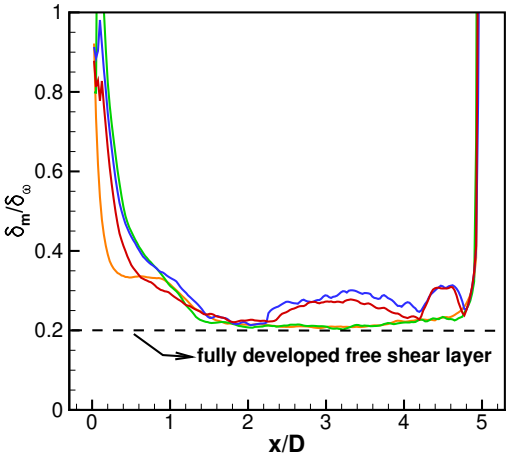
where $\bar{u}_1(x,z)$ represents the mean streamwise velocity component in the $x-z$ plane, and $y_0(x,z)$ is the maximum of y coordinate points in that plane where $\bar{u}_1(x,z) = 0$. Figure 5.32 presents how the dimensionless momentum and vorticity thicknesses, as well as their ratio, obtained by each employed DDES approach vary along the shear layer (at $z/D = 0.5$) emanating from the cavity leading edge. The results are



(a) momentum thickness



(b) vorticity thickness



(c) spreading ratio

Figure 5.32: Variations of the momentum thickness, the vorticity thickness, and the ratio of them along the shear layer

compared with the reference LES data. It is evident that the slopes of the predicted momentum thickness curves of all the cases are within 0.03 to 0.04. This range is common to free shear layers [46]. It may then be interpreted from these results that the momentum thickness spreading rates for the cavity in hand and those of free shear flows are similar, as also reported by some other studies [63]. As in the LES data given by [63], almost a linear variation can also be captured by the simulations with periodic BC. However, in the second half of the mixing layer the results with the slip wall BC show higher spreading rate unlike that predicted by LES. The reason may be again

the transition between the lateral BC conditions of the two mesh blocks: the outer block applies periodic conditions while the inner one applies slip wall BC. When the mentioned transition takes place between the same inner block and the wider outer block in the case of no-slip wall BC, the momentum thickness does not increase as such in the middle of the cavity mouth. In the vicinity of the aft corner, on the other hand, the thicknesses suddenly decrease, as expected because of the impingement.

The vorticity thickness variation of the reference LES study indicates existence of two linear zones, as shown in Figure 5.32b. The first zone has higher spreading rate, ending at $x/D \approx 0.7$. This zone is dominated by the K-H instability, revealing initial quasi-2D vortical structures with high amplification rates, followed by appearance of 3-D structures. This is like the transition state of the free mixing layers. The second zone starts with a lower spreading rate, representing a fully developed free shear layer region. The current simulations reveal two linear zones as well; however, the DDES one yields the first zone with a lower slope. This indicates that DDES fails to sufficiently resolve the K-H instability region due to the RANS mode. On the other hand, the SLA length scale detects the K-H instability waves and activates the LES mode, and thereby capturing the first zone slope. However, the end of the zone is estimated farther than that given by LES. Figure 5.32c points to this conclusion as well. The fully developed free shear layer zone starts at around $x/D = 1.5 - 2.0$ in all the present computations. The spanwise resolution may not be sufficient at this point.

Figure 5.33 demonstrates spanwise two-point auto-correlation of mean streamwise velocity profiles at different x/D locations along the shear layer. The locations are selected inside the K-H instability domain such that initial 2-D behavior of the separated shear layer can be investigated. The correlation function is computed as

$$C(x,r) = \frac{\int_r^{0.5D} \left[\bar{u}_1(x,D,z) - \bar{u}_{1z}(x,D)\right]\left[\bar{u}_1(x,D,z-r) - \bar{u}_{1z}(x,D)\right] dz}{\int_0^{0.5D} \left[\bar{u}_1(x,D,z) - \bar{u}_{1z}(x,D)\right]^2 dz} \tag{5.3}$$

$\bar{u}_{1z}$ is the span-averaged $\bar{u}_1$ value, and r is a distance between two points. The results, obtained by IDDES-SLA, show that as r increases, the correlation reduces as expected. The reason of obtaining negative values at some points is that the correlation

is computed from the perturbation values. In addition, it is observed from the variations the streamwise velocities at $x/D = 0.1$ are highly correlated up to $r/D = 0.2$, indicating 2-D structures. As the flow goes downstream, the spanwise correlation reduces. After $x/D = 0.7$, there is no correlation between points at $r/D = 0.1$ and further away such that flow field is dominated mostly by 3-D structures. This is consistent with the findings of the benchmark LES study.

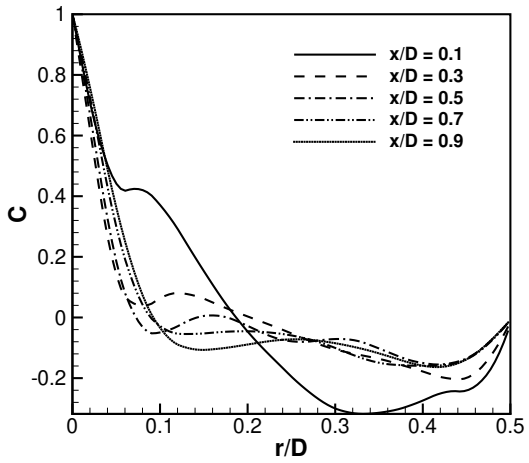
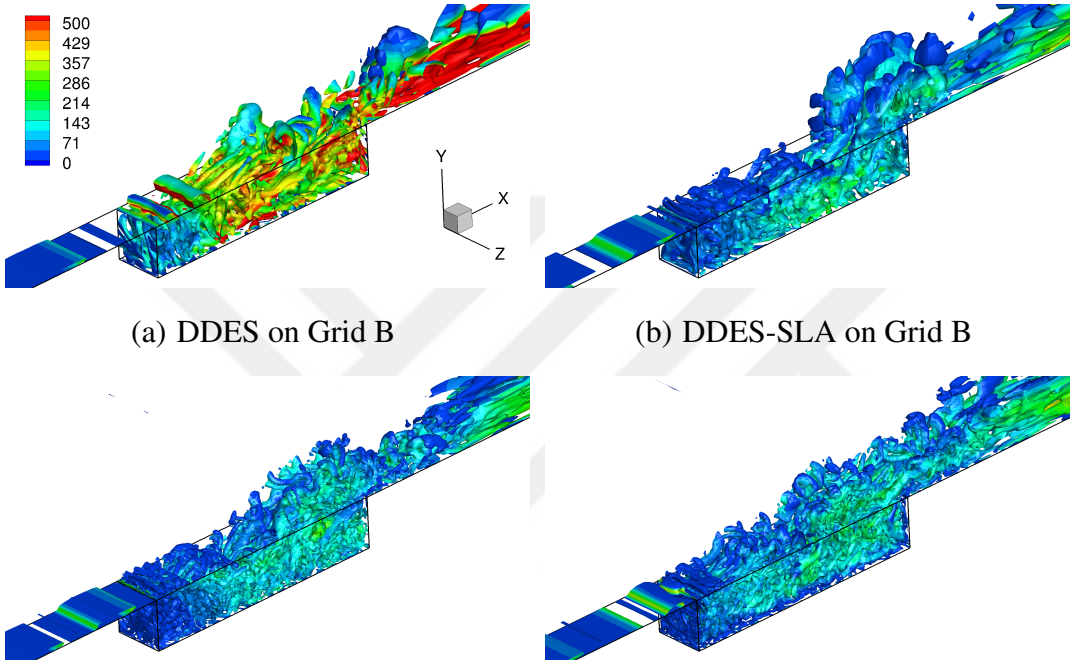


Figure 5.33: Spanwise two-point auto-correlation of mean streamwise velocity profiles at different locations along the shear layer

5.3.2.2 Instantaneous Flow Fields

This section presents instantaneous flow fields related to turbulence and acoustic properties. Recall that the current results of this section include only the ones available for the configuration without lateral solid walls. Q-criterion isosurfaces colored by the computed eddy viscosity values are presented first in Figure 5.34, in order to compare the turbulence resolution levels of the employed DDES, DDES-SLA, and IDDES-SLA methods. It is evident from the figure that some 2-D tubes near the leading edge exist as a sign of developing K-H instability waves. At this point it is useful to note that the SLA methods detect these waves immediately and accelerate the transition to the LES contents by reducing the subgrid length scale as well as the eddy viscosity. Consequently, the 2-D waves quickly roll in the spanwise direction, yielding a breakdown to 3-D fine structures in the simulations with the SLA length scale, but DDES delays this three-dimensionality. The effects of mesh resolution can

also be observed in Figures 5.34b-c. The resolution levels of the eddies from DDES-SLA and IDDES-SLA seem similar on the same mesh. However, the eddy viscosity contour levels differ locally. In the area around the cavity ceiling and the aft wall, IDDES-SLA reveals lower viscosity levels than DDES-SLA, indicating the WMLES mode is, indeed, activated by IDDES. On the contrary, higher levels appear around the front wall. Perhaps, the IDDES subgrid length scale in Equation (2.39) is not able to accomplish the rapid switching to the resolution mode of DDES as intended.



(a) DDES on Grid B

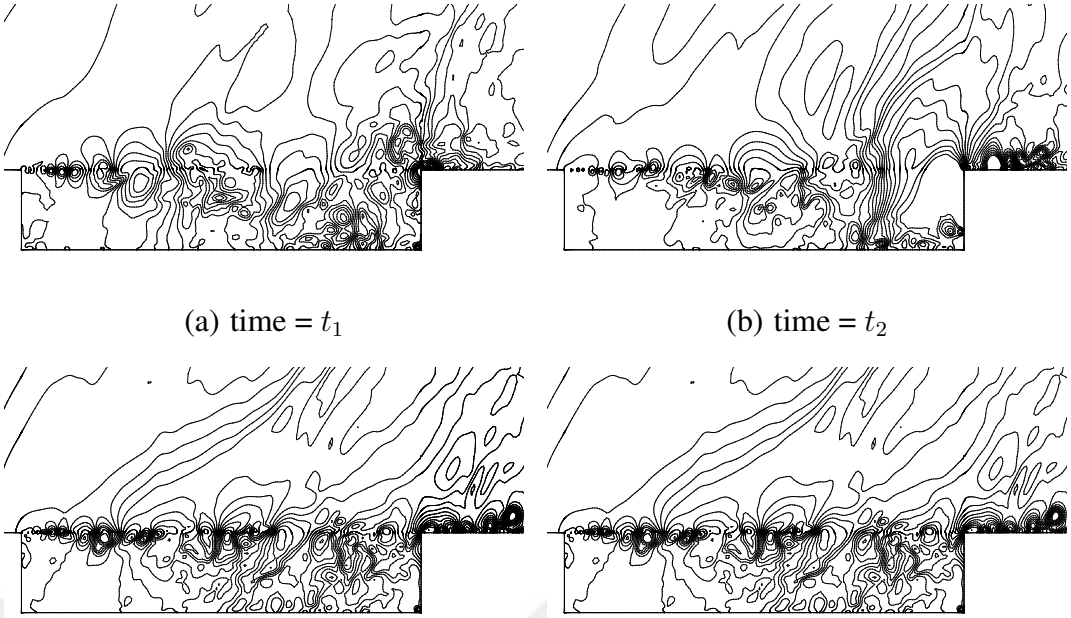
(b) DDES-SLA on Grid B

(c) DDES-SLA on Grid D

(d) IDDES-SLA on Grid D

Figure 5.34: Isosurfaces of Q-criterion ($Q = 0$) colored by $\hat{\nu}_t/\nu$ values

Pressure fluctuations predicted by IDDES-SLA at four sequential instants with equally spaced time intervals of one quarter of one eddy convection period along the cavity are presented in Figure 5.35. At the time of t_1 the development of the separated flow near the front wall can be seen while the downstream structures impinge on the aft wall. Then, at t_2, a large region of sparse contour lines appears near the aft wall, indicating a pressure build up due to the impingement. At t_3 and t_4 it is observed that upstream pressure fluctuations caused by the impingement merge with the downstream separated flow, increasing the complexity of the shear layer. This is typical of the feedback mechanism of open cavity flows.



(a) time = t_1 (b) time = t_2

(c) time = t_3 (d) time = t_4

Figure 5.35: Pressure fluctuations by IDDES-SLA at equally spaced instants over a convection period of shear layer

Acoustic results are obtained from the collected pressure data along the cavity ceiling at midspan. OASPL variations computed from this data are plotted in Figure 5.36. Experimental and IDDES data from literature are also included. OASPL is one of the important indicators for the simulation accuracy, as OASPL represents the total pressure energy at the data collection point. Besides, computation of total energy includes the contributions from all frequency levels; thus, it reduces the uncertain energy changes between dominant modes in the spectrum (recall the mode-switching phenomena in Section 1.1.3), and presents a more reliable sound levels [50, 63]. In general, all the current studies seem to have captured the OASPL trend along the ceiling except the front region. As aforementioned, the present simulations have no viscous lateral walls in the cavity, as opposed to the base studies. This may be the reason of large deviations around the front wall. As expected the sound levels increase towards the aft wall as a consequence of the widening shear layer structures and aft wall impingement. DDES-SLA simulations show closer levels to the benchmark data than DDES as expected. IDDES-SLA seems to have given the best results among

all the present computations. Apart from the front region, IDDES-SLA computes levels about 3 dB higher than those of the reference data whereas DDES-SLA shows nearly 5 dB and DDES shows 8 dB higher levels, respectively. This concludes that an increment in the eddy resolution directly enhances the noise level predictions. In addition, when looking at the DDES-SLA results, it is observed that changing the mesh resolution has an impact on the OASPL trend around the middle of the ceiling, particularly. Applying slip wall BC seems to correct the trend further as well as decrease the level discrepancies about 2 dB. Note that the improvement in sound levels using the slip wall BC compared to the periodic one is consistent with the findings in the study of [62].

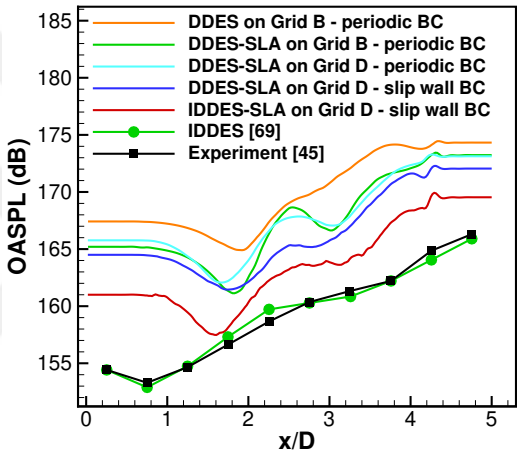


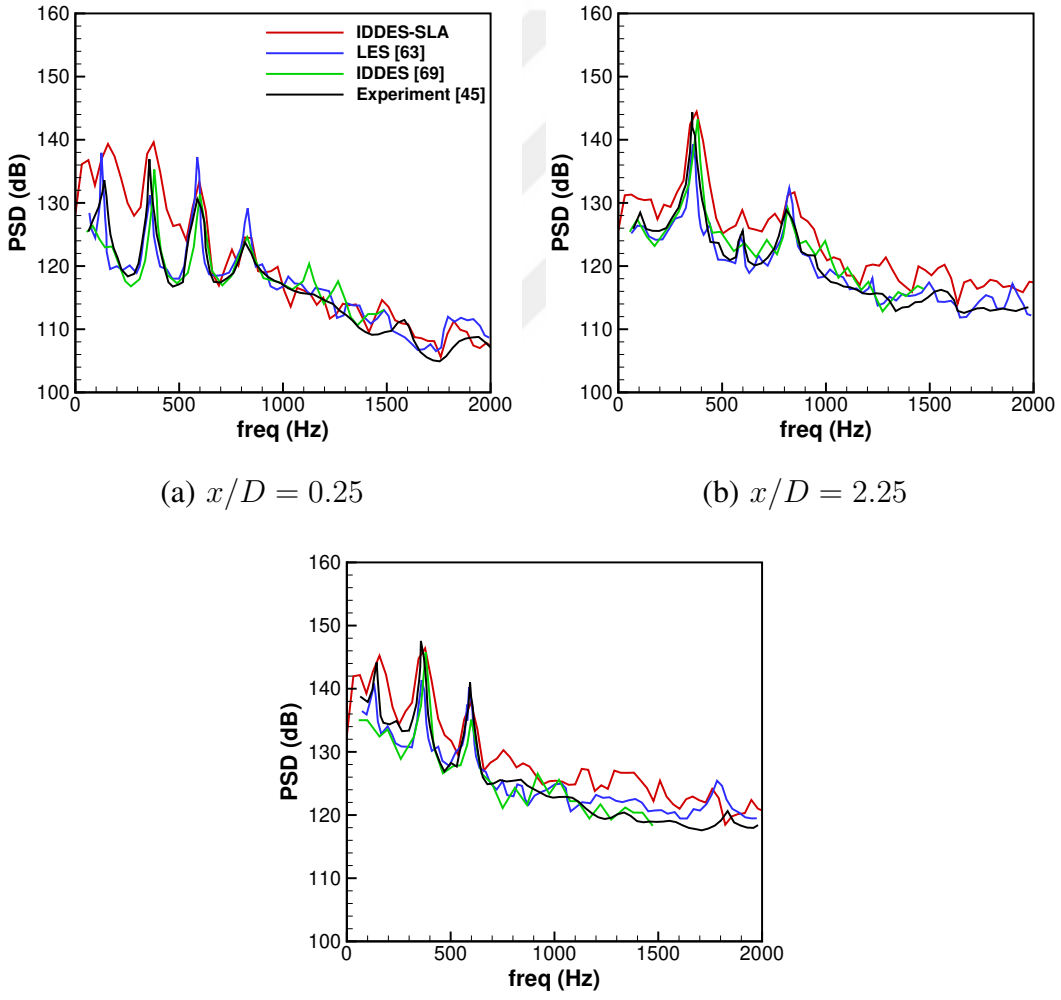
Figure 5.36: Comparison of overall sound pressure levels emitted from the cavity ceiling at midspan

In addition to the OASPL calculations, further analysis concerning particularly the spectral variations of the computed results is performed for the positions of $x/D = 0.25$, 2.25, and 4.25 along the ceiling at midspan. The time histories of the gathered pressure data are divided into multiple windows with 50% overlapping. Each window has 8192 data. Hanning windowing to minimize the spectral leakage, and then FFT are applied to each window. Then, the Power Spectral Density (PSD) levels are computed. The frequencies of Rossiter modes, corresponding to discrete peaks with narrow band, are given in Table 5.7 where all reference data as well as the ones obtained by the semi-empirical Rossiter's formula (see Appendix A) are also included. The agreement in these frequencies between the reference data and the present simu-

Table 5.7: Comparison of frequencies and PSD levels of Rossiter modes

	Frequencies (Hz)				PSD Levels (dB) at $x/D = 0.25$			
Methods	1st mode	2nd mode	3rd mode	4th mode	1st mode	2nd mode	3rd mode	4th mode
DDES on Grid B - periodic BC	145	365	590	830	152	142	135	128
DDES-SLA on Grid B - periodic BC	160	375	600	860	147	146	133	128
DDES-SLA on Grid D - periodic BC	155	375	610	870	147	145	131	122
DDES-SLA on Grid D - slip wall BC	155	375	600	850	146	142	131	123
IDDES-SLA on Grid D - slip wall BC	145	375	600	830	139	140	133	125
LES [63]	125	360	585	825	138	131	137	129
IDDES [69]	103	379	601	824	125	135	131	125
Experiment [45]	135	350	590	820	134	137	131	124
Rossiter's formula (see Appendix A)	148	357	566	775	-	-	-	-

lations is reasonably good. In addition, the PSD levels of these modes at $x/D = 0.25$ are included in the same table. It is found that the current simulations somewhat overestimates the sound levels at the first two modes. The other modes' levels can accurately be predicted, though. In general, DDES shows large discrepancies in PSD, compatible with the higher OASPL results. Using the SLA length scale reduces the discrepancies clearly. When compared to the measurements, performing simulations on the finer grid domain enhances the 4th mode sound level, particularly. Besides, conducting slip wall BC makes slight improvements on the first two mode levels. Apparently, the best agreement is provided by IDDES-SLA, as also observed in the OASPL levels. In particular, it is far better in estimating the first mode.



(a) $x/D = 0.25$ (b) $x/D = 2.25$

(c) $x/D = 4.25$

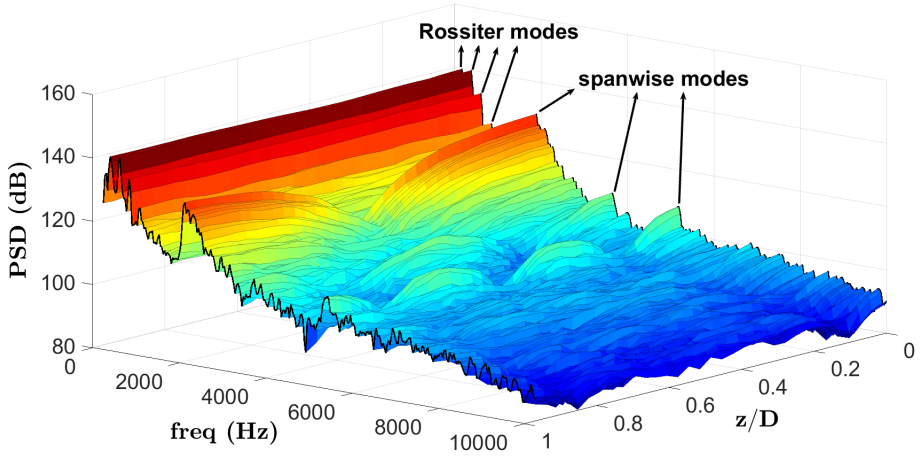
Figure 5.37: Comparison of PSD spectra at three cavity ceiling locations at midspan

Figure 5.37 compares the PSD spectrum of the IDDES-SLA results to the benchmark ones at the positions of $x/D = 0.25$, 2.25, and 4.25. In the graphs of all the data positions, Rossiter modes can clearly be observed. The mode frequencies appear independent from the data collection location. Analyzing Figure 5.37 shows that the current study overpredicts the low-frequency sound levels at $x/D = 0.25$, which causes a large discrepancy in OASPL in the corresponding region. It is observed for the rest that IDDES-SLA with slip wall BC is capable of capturing the cavity noise. Larger data collection periods may improve the predictions of the first mode. Moreover, differences at high frequencies up to 5 dB could be reduced by a finer grid than Grid D. Nevertheless, it is remarkable that this result of IDDES-SLA is obtained using much coarser grid than the reference studies, thanks to the turbulent length scale improvements as well as the high-fidelity numerical discretizations.

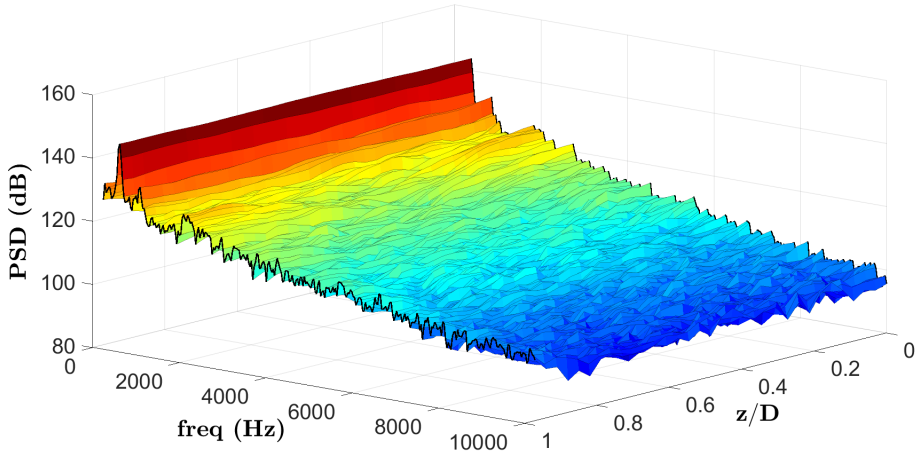
Presented in Figure 5.38 are sound level spectral surfaces along the span for the same three streamwise locations on the cavity ceiling. The results belong to the IDDES-SLA with slip wall BC study. It is shown that the Rossiter modes at all positions do not vary in the z-direction. As opposed to that, higher frequency sound levels exhibit spanwise variations. At $x/D = 0.25$, dominant modes apart from the Rossiter ones are clearly observed. These are the spanwise modes. Their sound levels vary throughout the span in a way of harmonic wave such that the modes can be ordered as 1st spanwise mode ($1s$), 2nd spanwise mode ($2s$), and so on as the frequency increases. Frequencies of these modes are shown in Figure 5.39 in which the PSD spectra at $z/D = 0$ for the first streamwise location are plotted. The frequencies are $f_{1s} = 1850$ Hz, $f_{2s} = 3650$ Hz, and $f_{3s} = 5200$ Hz, which are in fair agreement with the frequencies computed from the theoretical formula (Equation 5.4): 1840 Hz, 3680 Hz, and 5520 Hz, respectively.

$$f_{ms} = \frac{c_\infty m/(2W)}{\sqrt{1-(\kappa M_\infty)^2}}. \tag{5.4}$$

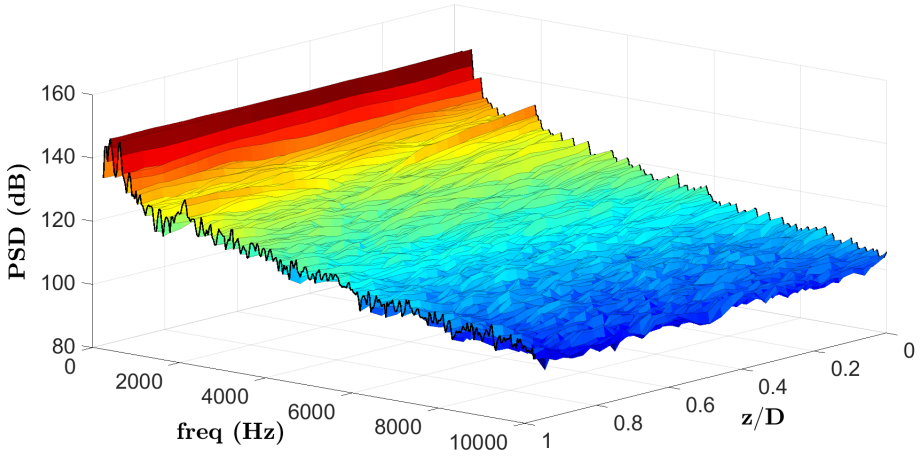
Here, ms is the mth spanwise mode number, and κ is the same function given in Appendix A. On the other hand, Figures 5.38b-c show that the 1st spanwise mode appears at $x/D = 2.25$, and $x/D = 4.25$ locations as well; however, the other ones are not clearly seen. It is also evident that the spanwise variations in higher frequencies increase at $x/D = 4.25$, probably due to the presence of the aft wall.



(a) $x/D = 0.25$



(b) $x/D = 2.25$



(c) $x/D = 4.25$

Figure 5.38: Sound level spectral surfaces along the span at three cavity ceiling locations

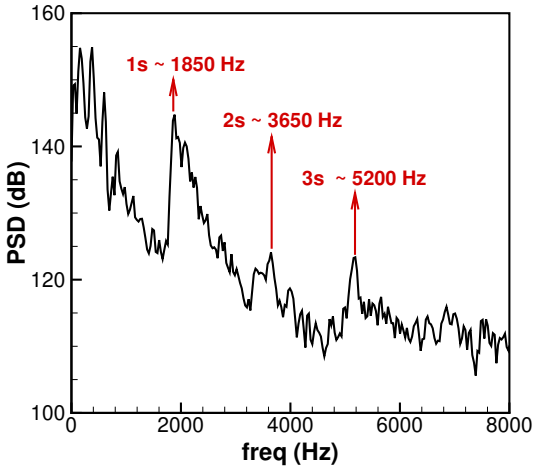


Figure 5.39: PSD spectra at $x/D = 0.25$, and $z/D = 0$ on the cavity ceiling with a spanwise acoustic mode representation

5.4 Supersonic Flow over an Open Cavity

In this section, a supersonic flow over an open cavity geometry is simulated by the IDDES-SLA framework. L/D and W/D are 5, and 0.5, respectively. The flow Mach number is 1.19 and the Reynolds number is 2×10^5. These values are selected so that the results with a reference LES study [93] can directly be compared. In addition, L/D is the same as in the previous problem of this thesis. Because the main flow characteristics are much more dependent on this ratio rather than W/D, the supersonic results could also be compared with the transonic ones.

5.4.1 Configurations and Setups

The simulation configuration is very similar to the transonic one which is given in Figure 5.24. Both the inner and the outer blocks have the same width. The rest of the dimensions of the outer block are set as

$$x_a/D = 13, \quad x_b/D = 9.2, \quad L/D = 5, \quad x_c/D = 15.5, \quad y/D = 20 \qquad (5.5)$$

The same BCs are applied on the computational boundaries as in the transonic prob-

Table 5.8: The details of the cavity grids

Grids	y^+	Δ_z/D	Δ_{max}/D	total # of cells	spatial scheme
IDDES-SLA	~ 2	2.0×10^{-2}	2.0×10^{-2}	$\sim$ 1.75 million	4th-order DRP
LES [93]	1.6	0.5×10^{-2}	2.2×10^{-2}	$\sim$ 20.0 million	6th-order

lem, except that since the flow leaving the domain is supersonic, all quantities at the outflow boundaries are extrapolated from the inner cells instead of using a pressure outlet condition. Moreover, unlike the transonic case, only one type of BCs is imposed at the spanwise boundaries. They are treated using periodic boundary conditions.

The mesh is generated in the same manner as in the transonic problem. Because the reference LES results were obtained by employing a solver with similar accuracy to METUDES, cell dimensions in the LES region are set as in the reference study. In this regard, $\Delta_{max} = \Delta_z = 2 \times 10^{-2} D$. Note that Δ_z of the LES study is 4 times shorter than the current one because the LES and DES grid requirements differ in the lateral direction. The grid details are compared in Table 5.8. The current grid density is much lower than the LES one, thanks to the RANS meshing near the solid walls.

5.4.2 Results and Discussion

Simulations are conducted using 112 cores. Δ_t^* is taken as 4×10^{-4}, corresponding to a physical time of 1.2×10^{-6} s.

Time-averaged flow fields are presented first. The boundary layer profile of the incoming flow is compared with the LES data at $x/L = -0.83$ in Figure 5.40. The velocity profile is in good agreement to the reference one, ensuring that the flow fields inside the cavity of both studies are subject to similar upstream conditions. Next, the stremwise velocity component and the TKE profiles over the cavity at midspan are demonstrated in Figure 5.41. Although the velocity profiles are in good agreement, the TKE results reveal some discrepancies, particularly in the vicinity of the aft wall. An insufficient resolution inside the WMLES region might be the reason for this.

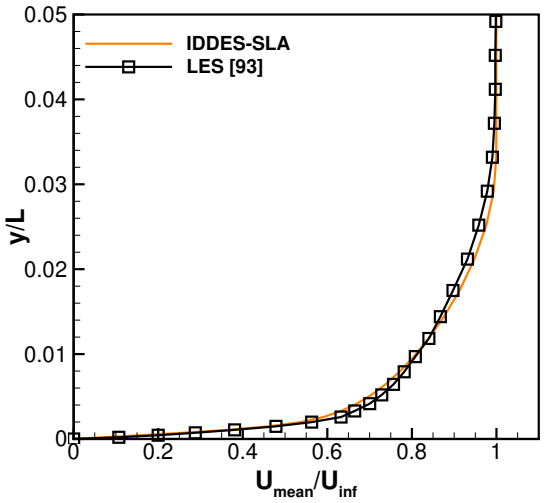
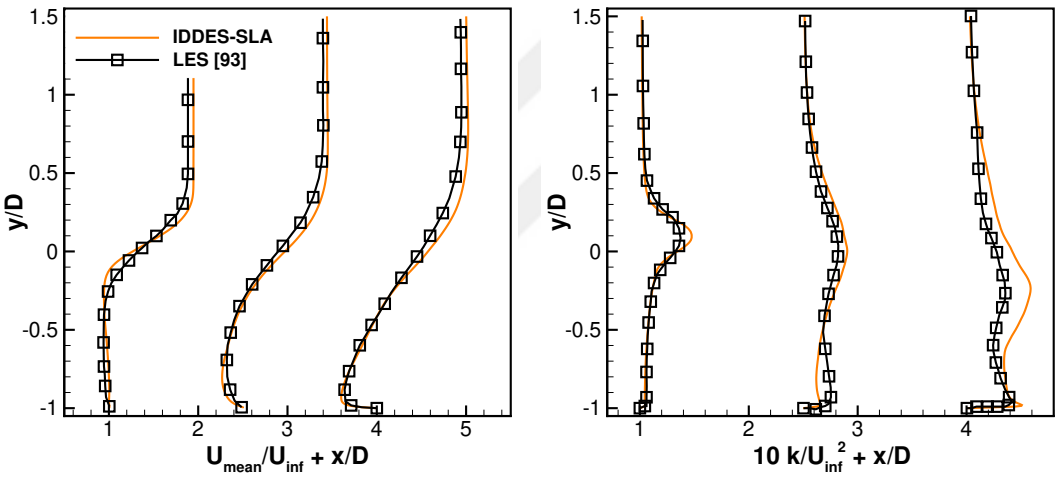


Figure 5.40: Comparison of boundary layer velocity profiles at $x/L = -0.83$



(a) Streamwise velocity (b) TKE

Figure 5.41: Comparisons of mean flow velocity and TKE profiles along the cavity at middle of the span

Figure 5.42 shows the streamlines at the midspan plane. It is observed that the separated flow directly impinges on the aft wall, which is the main characteristic of open cavity flows. Comparing the streamlines with the transonic flow one (recall Figure 5.31) indicates that supersonic flow results exhibit a large vortex near the front wall. In addition, the largest vortex has only one center in the supersonic flow while having two centers in the transonic one.

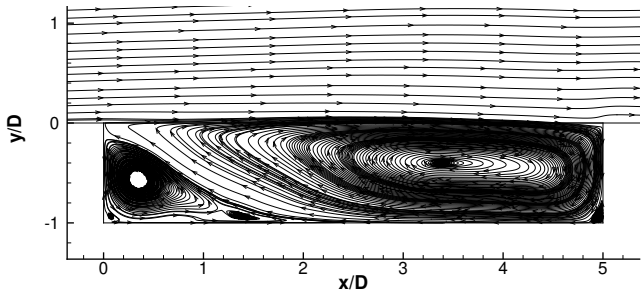
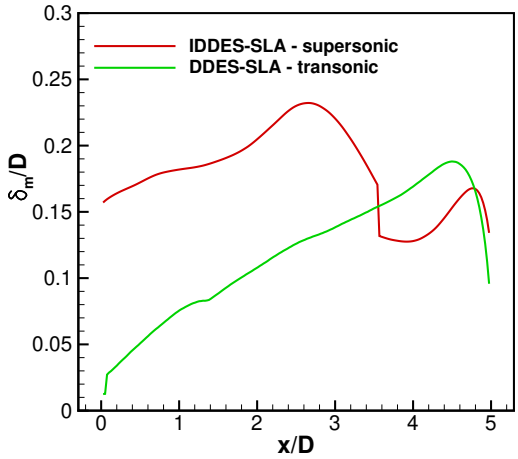


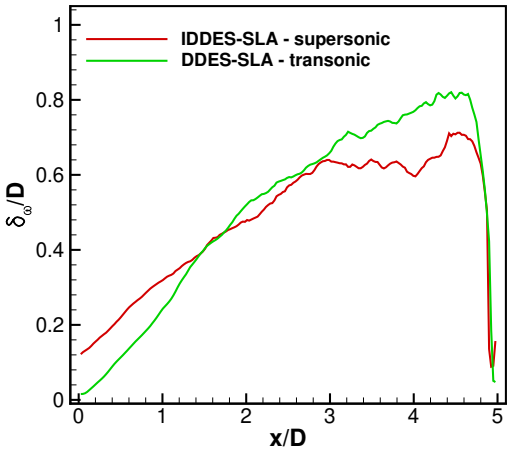
Figure 5.42: Streamlines of the mean flow fields at middle of the span obtained by IDDES-SLA

Momentum and vorticity thicknesses are shown in Figure 5.43. The corresponding transonic results obtained by DDES-SLA which has periodic spanwise boundary conditions are included for comparison. The results indicate that the initial supersonic momentum thickness is much larger than the transonic one, as a result of lower Reynolds number. The slopes of both momentum thickness variations match each other though, which is related to the mixing layer characteristic as discussed in Section 5.3. However, after $x/D \approx 2.8$, the thickness starts to decrease in the supersonic case. Such decrease is also seen in the vorticity thickness variation at a similar location. Moreover, at a downstream location ($x/D \approx 3.5$), a sudden drop in the momentum thickness is evident. This is probably related to a shock wave, which is observed at a similar location in another study [121] that conducted a dynamic mode decomposition analysis. The same study also reported that this shock wave possibly occurs as a consequence of feedback compression wave. After $x/D \approx 3.5$, the ratio of thicknesses reaches a plateau matching the fully developed free shear layer line.

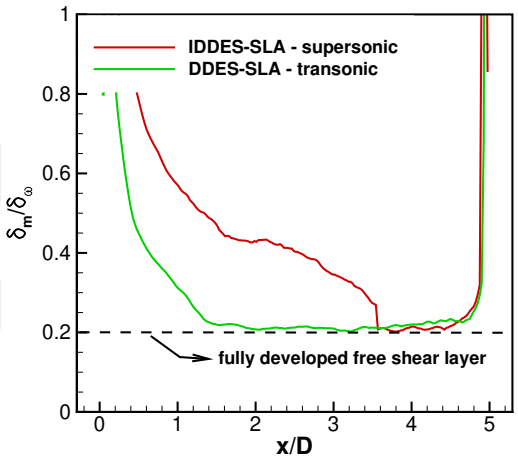
Figure 5.44 presents the isosurfaces of Q-criterion colored by the eddy viscosity levels. For comparison, IDDES-SLA results from the transonic problem are added in the same figure by resetting the viscosity levels to be the same as in the supersonic one. The first observation is that the supersonic flow field reveals eddy structures with lower viscosity levels than the transonic one. This is expected since the freestream Reynolds number of the supersonic flow is one order lower. Another observation is that IDDES-SLA with supersonic flow exhibits longer K-H instability region than the one with transonic flow, yielding mostly 2-D behavior around the front corner on the ceiling. Conversely, the same area is filled with 3-D structures in the transonic case.



(a) momentum thickness



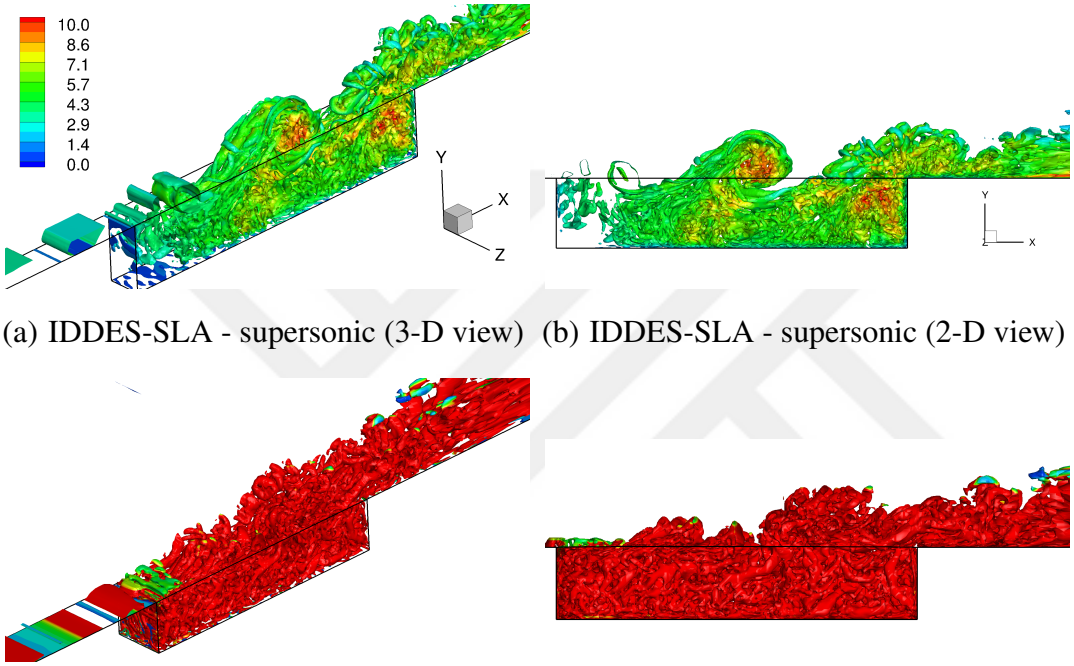
(b) vorticity thickness



(c) spreading ratio

Figure 5.43: Variations of the momentum thickness, the vorticity thickness, and the ratio of them along the shear layer

Lastly, at the streamwise location where the momentum thickness suddenly drops, as shown in Figure 5.43a, 3-D structures disappear for a short distance. Again, this may signify the shock wave occurrence.



(a) IDDES-SLA - supersonic (3-D view) (b) IDDES-SLA - supersonic (2-D view)

(c) IDDES-SLA - transonic (3-D view) (d) IDDES-SLA - transonic (2-D view)

Figure 5.44: Isosurfaces of Q-criterion ($Q = 0$) colored by $\hat{\nu}_t/\nu$ values of instantaneous flow fields

CHAPTER 6

CONCLUSIONS

In this thesis, various DDES frameworks are implemented in a high-order solver called METUDES, and its turbulent and acoustic flow field prediction capabilities are investigated by solving boundary layer transition as well as cavity noise problems. This chapter presents some concluding remarks and findings from the thesis study, and the further suggestions.

6.1 Improvements to METUDES

For transitional flow problems, the BCM transition model is incorporated into the DDES and DDES-SLA approaches of METUDES. The BCM implemented versions of the DES frameworks are called DDES-BCM and DDES-SLA-BCM3. In particular, three improvements are proposed and implemented in DDES-SLA-BCM3, aiming to overcome the deficiencies encountered during unsteady flow solutions. The implementations are validated through flatplate and Eppler E387 test cases.

On the other hand, the IDDES method is implemented and validated for cavity flow and acoustics problems. In addition, the SLA subgrid length scale is introduced into IDDES, called IDDES-SLA.

In order to provide application flexibility for complex geometries, a multiblock feature with overset capability is also added to the solver. This feature enables generation of tunnel grids around airfoils as well as cavity grids composed of two separate regions more easily. The overset grid approach is based on the Chimera technique with high-order interpolation methods. This allows the mesh blocks to have different

grid topologies. The multiblock and overset approaches are validated by solving an isentropic vortex convection problem.

Lastly, numerical difficulties encountered while performing the cavity flow simulations are eliminated by the following improvements:

- The residual smoothing algorithm used for the N-S equations is modified, and residual smoothing for the turbulence model equation is added.
- Dissipation for shock capturing regarding the turbulence equation is enhanced by the TVD switch.
- A biased artificial dissipation is implemented to be activated in grid cells near the solid walls.
- A scaling factor is added to the artificial dissipation of the turbulence equation for high aspect-ratio cells locating along the shear layer at the cavity mouth.

6.2 Boundary Layer Transition

In the transitional flow problems, DDES, DDES-SLA, and DDES-SLA-BCM3 approaches are considered. Flow conditions of the problems are selected to include mostly the separation-induced transition caused by slight separations of attached flows. These are difficult cases for DDES. There are two common findings from the studies of all these problems:

- The approaches using the SLA subgrid length scale reduces the eddy viscosity in the regions dominated by the Kelvin-Helmholtz instabilities, unlike DDES. This accelerates the transition from the RANS mode to the LES mode of DDES, thereby letting the instabilities inside boundary layers grow and increasing the turbulent content downstream. This allows DDES-SLA to achieve more accurate results than DDES at most of the flow conditions.
- The proposed modifications to the BCM model prevents the intermittency function from losing its persistence in cases involving strong unsteadiness.

The other significant results obtained in each problem are listed individually as follows:

6.2.1 Flow over an NRELS826 Blade Section

At Re of $100,000$

- When compared to a literature study, using a higher-order solver in the present computations enables capturing the stall angle better.
- Despite some small differences in the lift coefficients around the stall, the drag coefficients results of DDES-SLA-BCM3 are in better agreement with the measured data in literature than those of the DDES and DDES-SLA.
- At the post-stall angle, the onset of the separation bubble that triggers transition is predicted differently when the BCM model is used. This results in a more accurate C_d value.
- The flow can be kept laminar up to the transition point even without the BCM model. This is provided by solving the modified version of the S-A equation.

At Re of $145,000$

- All present approaches overpredict C_l and underpredict C_d at all angles of attack around the stall, when compared to the benchmark studies. It is inferred that a finer grid is needed.
- The expected stall occurs only in the DDES-SLA-BCM3 solution, but at a farther AoA.
- At the pre-stall angle, DDES-SLA reveals a separation bubble, unlike DDES. This is provided by the K-H instability sensor of the SLA approach. However, the exact location of the bubble can be predicted when the transition model is added.

6.2.2 Flow over a Circular Cylinder

- The results of DDES-BCM are also included in this case as the unsteadiness is weak (i.e. time and length scales are big enough).

- The drag coefficients given by DDES-BCM and DDES-SLA-BCM3 are in better agreement with the measured data from literature than those by DDES and DDES-SLA. The success of the frameworks with the transition model is provided by suppressing the eddy production unless a transition criterion is met, as indicated by the eddy viscosity onset angles.

- Higher Reynolds number causes the separated flow to reattach to the surface, and then separate again in the DDES-SLA simulations, whereas this is not observed in DDES. This late separation is also evident in the measurements.

- At Re of 5.0×10^5, despite showing an accurate flow separation angle, DDES-SLA-BCM3 reveals a reverse flow inside the boundary layer without an inflection point, which is not expected. This is possibly an indication of an incompatibility between the transition model and the SLA approach in this case, which requires further investigation.

All the investigated transitional flow problems demonstrate that predictions of both the pre- and post-transition regions are important in accurately calculating the desired aerodynamic coefficients. In this context, the collaboration of the SLA length scale and the BCM transition model has important roles in providing DDES with transitional behavior. It should be also emphasized that the BCM model is very attractive as it does not require any extra differential equations.

6.3 Cavity Flow

Transonic and supersonic flows over the M219 cavity without lateral solid walls are simulated by DDES, DDES-SLA, and IDDES-SLA. In the transonic case, the results are compared with some studies in literature in which the cavity geometry has lateral walls. On the other hand, the supersonic results are compared with another refer-

ence study which has the same lateral configuration. The main findings are given as follows:

6.3.1 Transonic Flow over an Open Cavity

- All the present approaches are able to capture the mean flow characteristics and turbulent kinetic energy profiles as long as the cavity width is taken equal to at least one depth.
- The simulations with SLA show the most accurate results in the early shear layer region, which are dominated by the K-H instabilities. This is attributed to a rapid transition to the LES mode.
- Using slip wall BC along the lateral cavity faces, instead of periodic one, improves the velocity and TKE gradients towards the aft wall, but worsens the gradients along the shear layer.
- The onsets of fully developed free shear layer obtained by all simulations occur at further downstream from the expected location. This requires a further investigation by increasing the mesh resolution in the LES region.
- IDDES-SLA yields less eddy viscosity in the vicinity of cavity ceiling and aft wall than DDES-SLA. This is considered as an indicator of the WMLES regions as intended, providing an increment of the eddy resolution.
- All present simulations capture the OASPL trend along the cavity ceiling except near the front wall. A possible reason is the absence of lateral walls in the present computations.
- All present simulations capture the frequencies of the Rossiter modes that are highly-intense and narrow-band tones.
- In general, the sound levels emanating from the ceiling predicted by IDDES-SLA are in better agreement with the benchmark results than those by the other approaches, whereas the levels obtained by DDES deviate from the benchmark results the most.

- Sound level spectral surfaces along the span show that the Rossiter modes exhibit mainly 2-D behavior. Apart from the Rossiter modes, there appear spanwise acoustic modes, the frequencies of which fairly match with those from the theoretical formula.

6.3.2 Supersonic Flow over an Open Cavity

- The simulation of this case is performed only by IDDES-SLA.
- Even though the velocity profiles over the cavity are in good agreement with the LES ones from literature, there appear slight deviations in the TKE profiles towards the aft wall.
- When compared to the transonic case, a longer K-H instability region is observed near the front wall.
- The supersonic flow reveals similar momentum and vorticity thickness variations along the shear layer to the transonic one. This is compatible with the free shear layer characteristics.
- At a certain point between the middle of the shear layer and the aft wall, the momentum thickness drops suddenly, unlike in the transonic case, which may indicate a shock wave occurrence.

The cavity studies show that a combination of IDDES and the SLA subgrid length scale has a great potential to simulate this type of complex flow fields. In addition, the results without lateral walls indicate that the proposed simulation configuration to reduce the computational cost substantially could be a good alternative in cavity flow problems, particularly in case of high Reynolds numbers.

6.4 Suggestions and Future Work

This study contains many efforts on improving the METUDES flow solver to be able to predict the transitional flow aerodynamics as well as the cavity flow noise through DDES frameworks. However, there are still numerical issues to overcome. The solver

needs further developments to accelerate the running performance. In this regard, multigrid method, implicit time integration, and nonblocking communications are some of the recommended features to include in the solver. On the other hand, the main problems encountered during the simulations are mainly related to the artificial dissipation of the S-A turbulence equation. In this context, the information in literature is limited. Although some improvements have been made during this thesis, a detailed numerical investigation regarding the weight of the TVD switch, the scaling of the artificial dissipation, etc. requires to validate these improvements.

For transitional DDES, the proposed incorporation of the BCM model into the DDES-SLA framework requires further development considering the incompatibility observed in the cylinder problem. Besides, DDES-SLA-BCM3 is mainly tested on the separation-induced transitional flow problems. However, it should be also tested on the other types of transition mechanisms such as natural, bypass, and wake-induced. In addition, a new approach, IDDES-SLA-BCM3, might be useful to predict the reattachment point in the separation-induced transitions.

For the cavity flow noise part, a decomposition of the Rossiter as well as the spanwise modes would indicate the flow physics better, and therefore, the effect of absence of lateral walls can be understood clearly.

REFERENCES

[1] B. Abu-Ghannam and R. Shaw. Natural transition of boundary layers—the effects of turbulence, pressure gradient, and flow history. *Journal of Mechanical Engineering Science*, 22(5):213–228, 1980.

[2] R. Allen, F. Mendonça, and D. Kirkham. Rans and des turbulence model predictions of noise on the m219 cavity at m= 0.85. *International Journal of Aeroacoustics*, 4(1):135–151, 2005.

[3] S. R. Allmaras and F. T. Johnson. Modifications and clarifications for the implementation of the spalart-allmaras turbulence model. In *ICCFD7-1902, Seventh International Conference on Computational Fluid Dynamics, Big Island, Hawaii*, 2012.

[4] J. Benek, J. Steger, and F. C. Dougherty. A flexible grid embedding technique with application to the euler equations. In *6th Computational Fluid Dynamics Conference Danvers*, page 1944, 1983.

[5] D. B. Bliss and R. E. Hayden. Landing gear and cavity noise prediction. *Landing gear and cavity noise prediction NASA*, 1976.

[6] C. Bogey and C. Bailly. Les of a high reynolds, high subsonic jet: effects of the subgrid modellings on flow and noise. In *16th AIAA Computational Fluid Dynamics Conference*, page 3557, 2003.

[7] M. Breuer, N. Jovičić, and K. Mazaev. Comparison of des, rans and les for the separated flow around a flat plate at high incidence. *International journal for numerical methods in fluids*, 41(4):357–388, 2003.

[8] S. Cakmakcioglu, I. Sert, O. Tugluk, and N. Sezer-Uzol. 2-d and 3-d cfd investigation of nrel s826 airfoil at low reynolds numbers. In *Journal of Physics: Conference Series*, volume 524, page 012028. IOP Publishing, 2014.

[9] S. C. Cakmakcioglu, O. Bas, and U. Kaynak. A correlation-based algebraic transition model. *Proceedings of the Institution of Mechanical Engineers, Part C: Journal of Mechanical Engineering Science*, 232(21):3915–3929, 2018.

[10] S. C. Cakmakcioglu, O. Bas, R. Mura, and U. Kaynak. A revised one-equation transitional model for external aerodynamics. In *AIAA AVIATION 2020 FORUM*, page 2706, 2020.

[11] J. Carter. Viscous-inviscid interaction analysis of transonic turbulent separated flow. In *14th Fluid and Plasma Dynamics Conference*, page 1241, 1981.

[12] K. Cengiz. *Use of detached eddy simulation for aerodynamics and aeroacoustics of blade sections*. PhD thesis, Middle East Technical University, 2018.

[13] K. Cengiz and Y. Özyörük. Experiences with two detached eddy simulation approaches through use of a high-order finite volume solver. *International Journal for Numerical Methods in Fluids*, 92(8):899–921, 2020.

[14] K. Cengiz, Ö. Yalçın, and Y. Özyörük. Akış kaynaklı rüzgar türbini gürültüsü hesaplamaları için yüksek çözünürlüklü 2 ve 3 boyutlu navier-stokes çözücülerinin geliştirilmesi ve uygulanması. *TUBİTAK 1001 Project Report*, 2016.

[15] A. Charwat. An investigation of separated flows-part i: The pressure field. *Journal of the Aerospace Sciences*, 28(6):457–470, 1961.

[16] N. Chauvet, S. Deck, and L. Jacquin. Zonal detached eddy simulation of a controlled propulsive jet. *AIAA journal*, 45(10):2458–2473, 2007.

[17] G. Chesshire and W. D. Henshaw. Composite overlapping meshes for the solution of partial differential equations. *Journal of Computational Physics*, 90(1):1–64, 1990.

[18] C. Çıray. *Akışkanlar Mekaniğine Giriş: Mühendislik Yaklaşımı*. ODTÜ Yayıncılık, 2007.

[19] J. G. Coder and H. D. Ortiz-Melendez. Transitional delayed detached-eddy simulation of multielement high-lift airfoils. *Journal of Aircraft*, 56(4):1303–1312, 2019.

[20] T. Colonius and S. K. Lele. Computational aeroacoustics: progress on nonlinear problems of sound generation. *Progress in Aerospace sciences*, 40(6):345–416, 2004.

[21] A. Crivellini and V. D'Alessandro. Spalart–Allmaras model apparent transition and RANS simulations of laminar separation bubbles on airfoils. *International Journal of Heat and Fluid Flow*, 47:70–83, June 2014.

[22] A. Crivellini, V. D'Alessandro, and F. Bassi. A Spalart–Allmaras turbulence model implementation in a discontinuous Galerkin solver for incompressible flows. *Journal of Computational Physics*, 241:388–415, May 2013.

[23] B. Crouse, S. Senthooran, D. Freed, G. Balasubramanian, M. Gleason, M. Puskarz, P.-T. Lew, and L. Mongeau. Experimental and numerical investigation of a flow-induced cavity resonance with application to automobile buffeting. In *12th AIAA/CEAS Aeroacoustics Conference (27th AIAA Aeroacoustics Conference)*, page 2494, 2006.

[24] W. Cui, Z. Xiao, and X. Yuan. Simulations of transition and separation past a wind-turbine airfoil near stall. *Energy*, 205:118003, 2020.

[25] S. Deck. Numerical simulation of transonic buffet over a supercritical airfoil. *AIAA journal*, 43(7):1556–1566, 2005.

[26] S. Deck. Recent improvements in the Zonal Detached Eddy Simulation (ZDES) formulation. *Theoretical and Computational Fluid Dynamics*, 26:523–550, 2012.

[27] N. K. Delany and N. E. Sorensen. Low-speed drag of cylinders of various shapes. *NACA Technical Note*, 3038, 1953.

[28] D. Di Pasquale, A. Rona, and S. Garrett. A selective review of transition modelling for cfd. In *39th AIAA fluid dynamics conference*, page 3812, 2009.

[29] T. D. Economon, F. Palacios, S. R. Copeland, T. W. Lukaczyk, and J. J. Alonso. Su2: An open-source suite for multiphysics simulation and design. *Aiaa Journal*, 54(3):828–846, 2016.

[30] ESDU. Aerodynamics and aero-acoustics of rectangular planform cavities. *Part I: Time Averaged Flow, ESDU data sheet*, 2008.

[31] ESDU. Aerodynamics and aeroacoustics of rectangular planform cavities. *Part II: Unsteady flow and aero-acoustics,, ESDU data sheet*, 2008.

[32] A. Favre. Equations des gaz turbulents compressibles. *J. de Mecanique*, 4(3), 1965.

[33] Flickr. A lockheed martin f-22a fighter shows off its internal weapons bays. `https://www.flickr.com/photos/50115004@N00/2501038976/`. Taken by Rob Shenk. Accessed November-2021.

[34] E. Gabriel, G. E. Fagg, G. Bosilca, T. Angskun, J. J. Dongarra, J. M. Squyres, V. Sahay, P. Kambadur, B. Barrett, A. Lumsdaine, R. H. Castain, D. J. Daniel, R. L. Graham, and T. S. Woodall. Open MPI: Goals, concept, and design of a next generation MPI implementation. In *Proceedings, 11th European PVM/MPI Users' Group Meeting*, pages 97–104, Budapest, Hungary, September 2004.

[35] A. R. George. Automobile aerodynamic noise. Technical report, SAE Technical Paper, 1990.

[36] N. J. Georgiadis, D. P. Rizzetta, and C. Fureby. Large-eddy simulation: current capabilities, recommended practices, and future research. *AIAA journal*, 48(8):1772–1784, 2010.

[37] X. Gloerfelt, C. Bailly, and D. Juvé. Direct computation of the noise radiated by a subsonic cavity flow and application of integral methods. *Journal of Sound and Vibration*, 266(1):119–146, 2003.

[38] S. Grace. An overview of computational aeroacoustic techniques applied to cavity noise prediction. In *39th Aerospace Sciences Meeting and Exhibit*, page 510, 2001.

[39] Y. Guo, K. J. Yamamoto, and R. W. Stoker. Experimental study on aircraft landing gear noise. *Journal of Aircraft*, 43(2):306–317, 2006.

[40] E. K. Guseva, A. V. Garbaruk, and M. K. Strelets. Assessment of delayed des and improved delayed des combined with a shear-layer-adapted subgrid length-scale in separated flows. *Flow, Turbulence and Combustion*, 98(2):481–502, 2017.

[41] C. Haigermoser. Application of an acoustic analogy to piv data from rectangular cavity flows. *Experiments in fluids*, 47(1):145–157, 2009.

[42] C. Haigermoser, F. Scarano, M. Onorato, P. Torino, and T. Delft. Investigation of the flow in a rectangular cavity using tomographic and time resolved piv. In *Proceedings of ICAS 26th International Congress of the Aeronautical Sciences, Anchorage, AK*, 2008.

[43] A. Hamed, D. Basu, and K. Das. Detached eddy simulations of supersonic flow over cavity. *AIAA paper*, 549:2003, 2003.

[44] H. H. Heller, D. Holmes, and E. E. Covert. Flow-induced pressure oscillations in shallow cavities. *Journal of sound and Vibration*, 18(4):545–553, 1971.

[45] M. Henshaw and J. de Charentenay. Verification and validation data for computational unsteady aerodynamics. Technical report, RTO Technical Report 26, 2000.

[46] L.-S. Huang and C.-M. Ho. Small-scale transition in a plane mixing layer. *Journal of Fluid Mechanics*, 210:475–500, 1990.

[47] R. Jacobs and P. Durbin. Simulations of bypass transition. *Journal of Fluid Mechanics*, 428:185, 2001.

[48] A. Jameson. The evolution of computational methods in aerodynamics. *Journal of Applied Mechanics*, 50(4b):1052–1070, 1983.

[49] A. Jameson. Time dependent calculations using multigrid, with applications to unsteady flows past airfoils and wings. In *10th Computational Fluid Dynamics Conference*, page 1596, 1991.

[50] M. A. Kegerise, E. F. Spina, S. Garg, and L. N. Cattafesta III. Mode-switching and nonlinear effects in compressible flow over a cavity. *Physics of Fluids*, 16(3):678–687, 2004.

[51] D. H. Kim, J. H. Choi, and O. J. Kwon. Detached eddy simulation of weapons bay flows and store separation. *Computers & Fluids*, 121:1–10, 2015.

[52] P. S. Klebanoff, K. Tidstrom, and L. Sargent. The three-dimensional nature of boundary-layer instability. *Journal of Fluid Mechanics*, 12(1):1–34, 1962.

[53] L. Kleiser and T. A. Zang. Numerical simulation of transition in wall-bounded shear flows. *Annual review of fluid mechanics*, 23(1):495–537, 1991.

[54] J. Kok. A high-order low-dispersion symmetry-preserving finite-volume method for compressible flow on curvilinear grids. *Journal of Computational Physics*, 228(18):6811–6832, 2009.

[55] J. C. Kok and S. P. Spekreijse. Efficient and accurate implementation of the k-omega turbulence model in the nlr multi-block navier-stokes system. 2000.

[56] D. Kožulović and B. L. Lapworth. An approach for inclusion of a nonlocal transition model in a parallel unstructured computational fluid dynamics code. *Journal of turbomachinery*, 131(3), 2009.

[57] K. Krishnamurty. Acoustic radiation from two-dimensional rectangular cutouts in aerodynamic surfaces. *NACA Technical Note*, 3487, 1955.

[58] S. L. Krist, R. T. Biedron, and C. L. Rumsey. Cfl3d user's manual (version 5.0). 1998.

[59] H. Lai and K. H. Luo. A three-dimensional hybrid les-acoustic analogy method for predicting open-cavity noise. *Flow, turbulence and Combustion*, 79(1):55–82, 2007.

[60] R. Langtry and S. Sjolander. Prediction of transition for attached and separated shear layers in turbomachinery. In *38th AIAA/ASME/SAE/ASEE Joint Propulsion Conference & Exhibit*, page 3641, 2002.

[61] R. Langtry and P. Spalart. Detached eddy simulation of a nose landing-gear cavity. In *IUTAM Symposium on Unsteady Separated Flows and Their Control*, pages 357–366. Springer, 2009.

[62] L. Larchevêque, P. Sagaut, and O. Labbé. Large-eddy simulation of a subsonic cavity flow including asymmetric three-dimensional effects. *Journal of Fluid Mechanics*, 577:105–126, 2007.

[63] L. Larchevêque, P. Sagaut, T.-H. Le, and P. Comte. Large-eddy simulation of a compressible flow in a three-dimensional open cavity at high reynolds number. *Journal of Fluid Mechanics*, 516:265–301, 2004.

[64] S. Lardeau, M. Leschziner, and T. Zaki. Large eddy simulation of transitional separated flow over a flat plate and a compressor blade. *Flow, turbulence and combustion*, 88(1-2):19–44, 2012.

[65] S. Lawson and G. Barakos. Review of numerical simulations for high-speed, turbulent cavity flows. *Progress in Aerospace Sciences*, 47(3):186–216, 2011.

[66] E. Lazar, G. Elliott, and N. . Glumac. Control of the shear layer above a supersonic cavity using energy deposition. *AIAA journal*, 46(12):2987–2997, 2008.

[67] K. R. Lee, J. H. Park, and K. H. Kim. High-order interpolation method for overset grid based on finite volume method. *AIAA journal*, 49(7):1387–1398, 2011.

[68] Z. Liu, G. Xiong, and C. Liu. Direct numerical simulation for the whole process of transition on 3-d airfoils. In *Fluid Dynamics Conference*, page 2081, 1996.

[69] K. Luo and Z. Xiao. Improved delayed detached-eddy simulation of transonic and supersonic cavity flows. In *Progress in Hybrid RANS-LES Modelling*, pages 163–174. Springer, 2015.

[70] K. Luo, W. Zhe, Z. Xiao, and S. Fu. Improved delayed detached-eddy simulations of sawtooth spoiler control before supersonic cavity. *International Journal of Heat and Fluid Flow*, 63:172–189, 2017.

[71] L. M. Mack. Boundary-layer linear stability theory. Technical report, California Inst of Tech Pasadena Jet Propulsion Lab, 1984.

[72] M. R. Malik and C. C. Kiris. Revolutionary computational aerosciences (rca) research portfolio and cfd 2030. In *High-Fidelity LES/DNS Data for Innovative Turbulence Models Kick-off Meeting*, 2019.

[73] R. J. McGhee. *Experimental results for the Eppler 387 airfoil at low Reynolds numbers in the Langley low-turbulence pressure tunnel*, volume 4062. National Aeronautics and Space Administration, Scientific and Technical ..., 1988.

[74] O. W. McGregor and R. White. Drag of rectangular cavities in supersonic and transonic flow including the effects of cavity resonance. *AIAA Journal*, 8(11):1959–1964, 1970.

[75] S. Medida and J. Baeder. Application of the correlation-based gamma-re theta t transition model to the spalart-allmaras turbulence model. In *20th AIAA computational fluid dynamics conference*, page 3979, 2011.

[76] F. R. Menter, R. B. Langtry, S. Likki, Y. Suzen, P. Huang, and S. Völker. A correlation-based transition model using local variables—part i: model formulation. *Journal of turbomachinery*, 128(3):413–422, 2006.

[77] F. R. Menter, P. E. Smirnov, T. Liu, and R. Avancha. A one-equation local correlation-based transition model. *Flow, Turbulence and Combustion*, 95(4):583–619, 2015.

[78] M. V. Morkovin. Bypass transition to turbulence and research desiderata. *Transition in Turbines*, 2386:161–204, 1985.

[79] R. Mura and S. C. Çakmakçıoğlu. A revised one-equation transitional model for external aerodynamics-part i: Theory, validation and base cases. In *AIAA Aviation 2020 Forum*, page 2714, 2020.

[80] NASA. Turbulence modeling resource. `http://turbmodels.larc.nasa.gov/flatplate_grids.html`. Accessed November-2021.

[81] P. Nayyar, G. Barakos, and K. Badcock. Analysis and control of weapon bay flows. In *NATO RTO AVT-123 Symposium on" Flow Induced Unsteady Loads and the Impact on Military Applications", Budapest*, pages 24–28, 2005.

[82] P. Nayyar, G. Barakos, and K. Badcock. Numerical study of transonic cavity flows using large-eddy and detached-eddy simulation. *Aeronautical Journal*, 111(1117):153–164, 2007.

[83] N. Nikitin, F. Nicoud, B. Wasistho, K. Squires, and P. R. Spalart. An approach to wall modeling in large-eddy simulations. *Physics of fluids*, 12(7):1629–1632, 2000.

[84] B. J. Olson and S. K. Lele. Directional artificial fluid properties for compressible large-eddy simulation. *Journal of Computational Physics*, 246:207–220, 2013.

[85] S. Peng, W. Haase, M. Braza, and A. Revell. M219 cavity flow. *DESider—A European Effort on Hybrid RANS-LES Modelling, Notes on Numerical Fluid Mechanics and Multidisciplinary Design*, 103:270–285, 2009.

[86] S.-H. Peng and S. Leicher. Des and hybrid rans-les modelling of unsteady pressure oscillations and flow features in a rectangular cavity. In *Advances in Hybrid RANS-LES Modelling*, pages 132–141. Springer, 2008.

[87] U. Piomelli. Wall-layer models for large-eddy simulations. *Progress in aerospace sciences*, 44(6):437–446, 2008.

[88] U. Piomelli and E. Balaras. Wall-layer models for large-eddy simulations. *Annual review of fluid mechanics*, 34(1):349–374, 2002.

[89] U. Piomelli, T. A. Zang, C. G. Speziale, and M. Y. Hussaini. On the large-eddy simulation of transitional wall-bounded flows. *Physics of Fluids A: Fluid Dynamics*, 2(2):257–265, 1990.

[90] E. B. Plentovich, R. L. Stallings Jr, and M. B. Tracy. Experimental cavity pressure measurements at subsonic and transonic speeds. static-pressure results. *NASA Technical Note*, 3358, 1993.

[91] M. A. Potsdam, V. Sankaran, and S. A. Pandya. Unsteady low mach preconditioning with application to rotorcraft flows. In *Proceedings of the 18th AIAA CFD Conference, Miami, FL*, 2007.

[92] D. P. Rizzetta. Numerical simulation of supersonic flow over a three-dimensional cavity. *AIAA journal*, 26(7):799–807, 1988.

[93] D. P. Rizzetta and M. R. Visbal. Large-eddy simulation of supersonic cavity flowfields including flow control. *AIAA journal*, 41(8):1452–1462, 2003.

[94] D. P. Rizzetta and M. R. Visbal. Direct numerical simulations of flow past an array of distributed roughness elements. *AIAA journal*, 45(8):1967–1976, 2007.

[95] D. Rockwell and E. Naudascher. Review—self-sustaining oscillations of flow past cavities. *Journal of Fluids Engineering*, 100(2):152–165, 1978.

[96] J. Rossiter. A preliminary investigation into armament bay buffet at subsonic and transonic speeds. *Royal Aircraft Establishment, TM AERO*, 679, 1960.

[97] J. Rossiter. Wind tunnel experiments on the flow over rectangular cavities at subsonic and transonic speeds. Technical report, Ministry of Aviation; Royal Aircraft Establishment; RAE Farnborough, 1964.

[98] J. Rossiter and A. Kurn. Wind tunnel measurements of the unsteady pressures in and behind a bomb bay (tsr 2). Technical report, Technical Report AERO. 2677, Royal Aircraft Establishment, 1963.

[99] C. W. Rowley, T. Colonius, and A. J. Basu. On self-sustained oscillations in two-dimensional compressible flow over rectangular cavities. *Journal of Fluid Mechanics*, 455:315–346, 2002.

[100] SAE. Landing gear housings during landing. `https://www.sae.org/dlymagazineimages/web/516/9148_10447.jpg`. Accessed November-2021.

[101] H. Sarlak, R. Mikkelsen, S. Sarmast, and J. N. Sørensen. Aerodynamic behaviour of nrel s826 airfoil at re= 100,000. In *Journal of Physics: Conference Series*, volume 524, page 012027. IOP Publishing, 2014.

[102] S. Sarmast. *Numerical study on instability and interaction of wind turbine wakes*. PhD thesis, KTH Royal Institute of Technology, 2014.

[103] A. Savill. Some recent progress in the turbulence modelling of by-pass transition. *Near-wall turbulent flows*, pages 829–848, 1993.

[104] P. Shankar and M. Deshpande. Fluid mechanics in the driven cavity. *Annual Review of Fluid Mechanics*, 32(1):93–136, 2000.

[105] M. L. Shur, P. R. Spalart, M. K. Strelets, and A. K. Travin. A hybrid rans-les approach with delayed-des and wall-modelled les capabilities. *International Journal of Heat and Fluid Flow*, 29(6):1638–1649, 2008.

[106] M. L. Shur, P. R. Spalart, M. K. Strelets, and A. K. Travin. An enhanced version of des with rapid transition from rans to les in separated flows. *Flow, Turbulence and Combustion*, 95(4):709–737, 2015.

[107] N. N. Sørensen, A. Bechmann, and F. Zahle. 3d cfd computations of transitional flows using des and a correlation based transition model. *Wind Energy*, 14(1):77–90, 2011.

[108] P. Spalart, W. Jou, M. Strelets, and S. Allmaras. Comments on the feasibility of les for wings, and on a hybrid rans/les approach. *Advances in DNS/LES*, 1:4–8, 1997.

[109] P. R. Spalart. Detached-eddy simulation. *Annual Review of Fluid Mechanics*, 41:181–202, 2009.

[110] P. R. Spalart, S. Deck, M. L. Shur, K. D. Squires, M. K. Strelets, and A. Travin. A new version of detached-eddy simulation, resistant to ambiguous grid densities. *Theoretical and Computational Fluid Dynamics*, 20:181–195, 2006.

[111] P. R. Spalart and C. Streett. Young-person's guide to detached-eddy simulation grids. *NASA/CR-2001-211032*, 2001.

[112] R. L. Stallings Jr, E. B. Plentovich, M. B. Tracy, and M. J. Hemsch. Measurements of store forces and moments and cavity pressures for a generic store in and near a box cavity at subsonic and transonic speeds. 1995.

[113] M. J. Stanek, M. R. Visbal, D. P. Rizzetta, S. G. Rubin, and P. K. Khosla. On a mechanism of stabilizing turbulent free shear layers in cavity flows. *Computers & Fluids*, 36(10):1621–1637, 2007.

[114] H. W. Stock and W. Haase. Navier-stokes airfoil computations with e transition prediction including transitional flow regions. *AIAA journal*, 38(11):2059–2066, 2000.

[115] Y. Suzen and P. Huang. Modeling of flow transition using an intermittency transport equation. *J. Fluids Eng.*, 122(2):273–284, 2000.

[116] R. C. Swanson, R. Radespiel, and E. Turkel. On some numerical dissipation schemes. *Journal of computational Physics*, 147(2):518–544, 1998.

[117] R. C. Swanson and E. Turkel. On central-difference and upwind schemes. In *Upwind and High-Resolution Schemes*, pages 167–181. Springer, 1992.

[118] C. K. Tam and J. C. Webb. Dispersion-relation-preserving finite difference schemes for computational acoustics. *Journal of computational physics*, 107(2):262–281, 1993.

[119] E. Turkel. Preconditioning-squared methods for multidimensional aerodynamics. In *13th Computational Fluid Dynamics Conference*, Snowmass Village, CO, U.S.A., jun 1997. American Institute of Aeronautics and Astronautics.

[120] J. Vogel and J. Eaton. Combined heat transfer and fluid dynamic measurements downstream of a backward-facing step. *ASME*, 107, 1985.

[121] J. Wang, X. Ming, H. Wang, Y. Ma, and J. Wu. Flow characteristics of a supersonic open cavity. *Fluid Dynamics*, 54(5):724–738, 2019.

[122] S. Wang, M. Ge, X. Deng, Q. Yu, and G. Wang. Blending of algebraic transition model and subgrid model for separated transitional flows. *AIAA Journal*, 57(11):4684–4697, 2019.

[123] C. Weiselberger. New data on the laws of fluid resistance, naca tech. *Note TN84*, 1922.

[124] F. M. White and J. Majdalani. *Viscous fluid flow*, volume 3. McGraw-Hill New York, 2006.

[125] D. C. Wilcox. Simulation of transition with a two-equation turbulence model. *AIAA journal*, 32(2):247–255, 1994.

[126] Ö. Yalçın. Development of a high-order navier-stokes solver for aeroacoustic predictions of wind turbine blade sections. Master's thesis, Middle East Technical University, 2015.

[127] Ö. Yalçın, K. Cengiz, Y. Wein, Lars Özyörük, and J. R. Seume. Transitional ddes study over a circular cylinder and an airfoil profile. In *13th International ERCOFTAC symposium on engineering, turbulence, modelling and measurements (ETMM13)*, 2021.

[128] Z. Yang. On bypass transition in separation bubbles: a review. *Propulsion and Power Research*, 8(1):23–34, 2019.

[129] Z. Yang, P. R. Voke, and A. M. Savill. Mechanisms and models of boundary layer receptivity deduced from large-eddy simulation of by-pass transition. In *Direct and large-eddy simulation I*, pages 225–236. Springer, 1994.

APPENDIX A

THE ROSSITER FORMULA

The original Rossiter formula was given in [97] as

$$f_m = \frac{U_\infty}{L} \frac{m - \alpha}{M_\infty + 1/\kappa} \tag{A.1}$$

where m is the mode number and f is the frequency. U_∞ and M_∞ are the freestream velocity and Mach numbers, respectively. κ and α are functions of L/D where L represents the cavity length and D represents the cavity depth. The cavity geometries studied in this work have L/D of 5. The corresponding κ and α functions equal to 0.57 and 0.29, respectively.